TECHNIQUES FOR LASER INTERFEROMETER GRAVITATIONAL WAVE DETECTORS

by

PETER KURT FRITSCHEL

B.A. Swarthmore College
(1984)

SUBMITTED IN PARTIAL FULFILLMENT
OF THE REQUIREMENTS FOR THE
DEGREE OF

DOCTOR OF PHILOSOPHY

at the

MASSACHUSETTS INSTITUTE OF TECHNOLOGY

February, 1992

Signature of Author _____
Department of Physics
October, 1991

Certified by _____
Rainer Weiss
Thesis Supervisor

Accepted by _____
George Koster
Chairman, Department Committee

TECHNIQUES FOR LASER INTERFEROMETER GRAVITATIONAL WAVE DETECTORS

by

PETER KURT FRITSCHEL

Submitted to the Department of Physics in October, 1991
in partial fulfillment of the requirements for
the degree of Doctor of Philosophy in Physics

Abstract

Laser interferometry is being developed as a method for the detection of gravitational radiation. A Michelson interferometer is intrinsically sensitive to the differential optical path length changes produced in its two orthogonal arms by a passing gravitational wave. The path length changes due to expected astronomical sources of gravitational radiation are, however, extremely small. Their detection requires that new forms of interferometers, and new methods of fringe detection, be developed and tested.

A small prototype interferometer built to study some of these techniques is described. This Michelson interferometer employs Fabry-Perot cavities in the arms as a means of increasing the conversion of arm length variations to optical phase variations. One of the experiments uses internal phase modulation as a method for generating the error signals necessary to hold the cavities on resonance and to maintain the dark fringe condition. Internal modulation also provides a potentially shot-noise limited signal proportional to the interferometer path length difference. The advantages and limitations of this technique are discussed.

Another experiment investigates the technique of light recycling. This is a method for increasing the effective light power in the interferometer by a resonant build-up of the input light. This is the first experimental demonstration of light recycling with a Fabry-Perot arm interferometer. An increase in the circulating power by a factor of 18 is observed, in good agreement with the expected gain given the losses of the system. The experiment also addresses several phenomena associated with the configuration of coupled optical cavities found in a recycled Fabry-Perot interferometer.

The recycling experiment uses a different phase modulation geometry for detecting the output signal. This is the external modulation technique, where a fraction of the circulating light is split off to form a reference beam. This beam is phase modulated and interfered with the interferometer output field. By removing the modulators from the arms of the interferometer, external modulation avoids limitations due to losses and distortions in the modulators.

Throughout the thesis, the application of these techniques to a full-scale gravity wave detector is discussed.

Acknowledgments

For the initial idea of doing these types of experiments, for regularly providing motivation and inspiration to do them, for instilling in me a love of basic research and a style of doing it, for supplying everything from six-shooters to the mother-of-all-programs, I thank my thesis advisor, Rainer Weiss.

For contributing his lab skills and intuition not only to the experiments but also to my development as a researcher, for his invaluable and just plain fun partnership in the lab, and for showing me how things are done in other parts of the world, I thank David Shoemaker.

For help with these experiments along the way, I thank: Jeff Livas, originator of the life-size schedule which planned on this work being finished 3 years ago; Nelson Christensen, whose uncharacteristic patience with fibers meant I didn't have to test mine; and Joe Giaime, developer of a photodetector too quiet for its own good, and a possible future partner in a PVC plumbing business.

I give my greatest thanks to my wife and companion, Pam.

"At the MIT they are currently working on the Laser Interferometer Gravitational-Wave Observatory, known by the mellifluous acronym 'LIGO'. It is, put simply, a pair of 2.5 mile underground tunnels for trapping and observing lasers. Why you ask, would you make such tunnels, why not see the laser show at the planetarium and study the phenomenon there!"

Otto Sternenkrausen

Table of contents

1 Introduction

1.1 Introduction and history

The modern physicist often does not have a thorough understanding of what appears to be the correct classical theory of gravity – general relativity –. Yet it is not surprising to such a physicist that the theory predicts the existence of gravitational radiation – for a gravitational field cannot change instantaneously without violating causality – nor that gravity waves should travel at the speed of light – for that is the only Lorentz invariant velocity. The existence of gravitational radiation is generally accepted without the supporting evidence of a direct detection of gravity waves, for there is convincing indirect evidence (see the last paragraph in this section). The detection of gravity waves would at the very least prove their existence and measure their propagation properties. The possible rewards are much higher. Since any detected radiation would originate from astrophysical sources (see section 1.2), a measurement of gravity waves would provide new information about the physics of these sources. It would provide much-needed data on the physics in the poorly understood regime of relativistically strong gravity. A gravity wave detector would be a new kind of observatory on the universe, providing information that would further – and maybe change – our understanding of the universe.

The prediction of gravitational radiation by Einstein (Einstein 1916) did not exactly open the floodgates of experimental research in this field. The effort to detect gravitational radiation did not start until the early 1960's with J. Weber's experiments with resonant acoustic bar antennas (Weber 1960). These detectors are solid elastic bodies, whose fundamental mode is excited by a passing gravity wave of appropriate frequency. The field expanded considerably after 1969 in response to Weber's claimed detection of gravity waves (Weber 1969), as over a dozen groups tried to construct similar bar detectors to see if Weber's results could be reproduced. Unfortunately, no one was able to confirm the alleged detection.

The sensitivity of bar detectors has increased greatly since the initial experiments due to improvements in transducers and seismic isolation, and operation of the bars at cryogenic temperatures. Today these detectors have attained strain sensitivities of $h_{\rm rms} \sim 10^{-18}$, generally operating at about 1 kHz with a bandwidth of a few hertz. For a review of bar technology see Michelson, Price and Taber (1987) and Thorne (1987).

The idea of detecting gravity waves using a laser interferometer was first suggested by Gertsenshtein and Pustovoit (1962). This idea of interferometrically monitoring the relative positions of test masses – masses free to move under the influence of a passing gravity wave – was independently conceived of by Weiss (1972), who performed a detailed design study for such an experiment. R. Forward, a former student of J. Weber's, built the world's first prototype gravity wave interferometer in the 1970's at Hughes Research Laboratories (Forward 1978). This early work was followed by efforts at Munich, Glasgow, MIT, Caltech, Orsay, and more recently

ISAS in Japan. As with the resonant bar detectors, the sensitivities of the prototype interferometers have improved by several orders of magnitude over the first detectors. Unlike bar detectors, the interferometers will require an increase in scale of about two orders of magnitude (arm lengths of several kilometers are needed) before they will be able to reach a sensitivity thought to be sufficient to detect gravity waves. At the moment there are four groups worldwide planning to build large baseline interferometers, so that at last the adjective 'prototype' can be dropped: a Caltech/MIT collaboration (LIGO) planning to build two interferometers in the United States (Vogt 1989); a Max Planck/Glasgow collaboration planning a detector in Germany (Hough et al. 1989); a French/Italian antenna planned for northern Italy (Brillet 1989); and an Australian proposal for a site in western Australia (Blair 1989).

While it is true that gravity waves have not yet been directly detected, a discussion of the history of gravity waves would be severely lacking if it did not mention that the existence of gravitational radiation has been all but proven by the observations of the binary pulsar system PSR 1913+16 initiated by J. Taylor (Taylor and Weisberg 1982). The measured rate of decay of the orbital period of the two neutron stars agrees with the theoretical prediction – using general relativity – which takes into account the energy the system is expected to radiate in the form of gravitational radiation.

1.2 Physics of gravitational radiation

The wave solution to Einstein's equations. Much of the physics of general relativity is contained in the metric, $g_{\mu\nu}$. The inherent nonlinearity of general relativity in general makes the computation of the metric very difficult if not impossible, but here on earth the gravitational fields are always weak enough so that they can be described by the so-called linearized theory. In this weak field limit, the metric can be approximated as

$$g_{\mu\nu} \approx \eta_{\mu\nu} + h_{\mu\nu}\,, \quad |h_{\mu\nu}| \ll 1\,, \tag{1}$$

where $\eta_{\mu\nu}$ is the Minkowski metric. The weak-field Einstein equations in vacuum then take the form (with a suitable choice of gauge)

$$\left(-\frac{1}{c^2}\frac{\partial^2}{\partial t^2} + \nabla^2\right) h_{\mu\nu} = 0. \tag{2}$$

This is clearly a wave equation and the solution can be written in terms of a traveling plane wave

$$h_{\mu\nu} = h_0 \epsilon_{\mu\nu} e^{ik_\mu x^\mu}\,, \tag{3}$$

provided that k_μ satisfies $k_\mu k^\mu = 0$. With a further choice of gauge known as the transverse-traceless gauge, the components of the (polarization) tensor are much constrained. For a frame in which the wave is traveling in the z direction, the origin

of the adjectives 'transverse-traceless' becomes clear, as the tensor $\epsilon_{\mu\nu}$ takes the form

$$\epsilon_{\mu\nu} = \begin{pmatrix} 0 & 0 & 0 & 0 \\ 0 & \epsilon_{xx} & \epsilon_{xy} & 0 \\ 0 & \epsilon_{xy} & -\epsilon_{xx} & 0 \\ 0 & 0 & 0 & 0 \end{pmatrix}. \tag{4}$$

Since the strength of the wave can be contained in the parameter h_0, the elements of the polarization tensor can be restricted to the values ϵ_{ij}= 0,1. Just as for an electromagnetic wave propagating in free space, the fields are transverse to the direction of propagation.

Effect on free masses. This analogy between electromagnetic waves and gravitational waves is a useful one; applying it further, we expect a gravity wave to produce a force on a massive particle. In general relativity, the geodesic equation corresponds to the equation of motion in non-relativistic physics. Using the transverse-traceless gauge, the geodesic equation shows that the coordinate position of a free particle in fact does not change in the presence of a gravity wave. The *proper* distance $ds^2 = g_{\mu\nu}dx^\mu dx^\nu$ between two particles, however, one located at the origin and the other at x=x_0, y=z=0, is affected by a gravity wave (assuming ϵ_{xx}=1):

$$\triangle s = \int_0^{x_0} |g_{xx}|^{1/2} dx \approx [1 + \tfrac{1}{2}h_0]x_0 \,. \tag{5}$$

The gravity wave produces a relative 'displacement' of two particles, in the sense of the proper distance between them, that is proportional to their initial separation. Furthermore, since h_{yy}=$-h_{xx}$, the proper distance between the particle at the origin and a particle at y=y_0, x=z=0 is $\triangle s \approx [1 - \frac{1}{2}h_0]y_0$. The assignment $|\epsilon_{xx}| = 1, |\epsilon_{xy}| = 0$ corresponds to the linear polarization state labeled '+' (plus). The other choice $|\epsilon_{xx}| = 0, |\epsilon_{xy}| = 1$ is denoted by the term '×' (cross) polarization. The effect of gravity waves with these two polarization states on a ring of free particles is shown in Figure 1.1 in terms of the proper distance relative to a particle at the center.

The effects of gravity waves can also be analyzed in a 'rigid' coordinate system whose coordinate lengths are unaffected by the wave. Using this picture, a '+' polarized wave traveling in the z direction will produce a force on a particle at x=x_0, y=z=0, of magnitude $F = \frac{1}{2}m\ddot{h}_0x_0$ in the x direction. The resulting displacement, in the familiar sense of the word, is thus $\delta x = \frac{1}{2}h_0x_0$; that is, the gravity wave produces a tidal force.

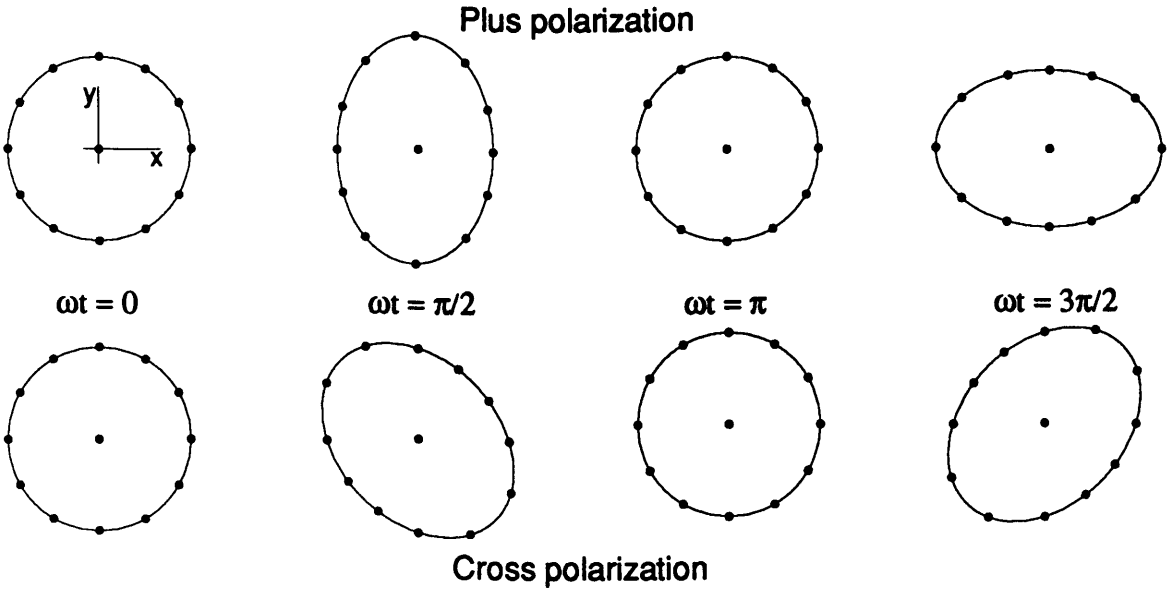

Fig. 1.1 Effect of the two linear polarization states of a gravity wave on a ring of free particles.

In either picture the induced 'displacement' between two particles is proportional to the separation of the particles. It is thus common to regard h as a strain, i.e. a gravity wave of field amplitude h produces a strain of magnitude h.

Generation and strength of gravity waves. The expected strength and frequencies of gravity waves impinging upon the earth will obviously dictate the detector sensitivity required for a reasonable chance of detection. The required sensitivity will drive the choice of technologies, and so it is important to examine source strength estimates in order to arrive at a sensitivity goal.

An estimate of the field strength can be made based upon the linearized theory. Gravitational radiation is produced by the oscillating multipole moments of the mass distribution of a system. Mass conservation rules out monopole radiation (just as charge conservation does so in E&M), and momentum conservation (linear and angular) rules out gravitational dipole radiation. Quadrupole radiation is the lowest order allowed form, and thus usually the dominant form. In this case the wave field is proportional to $\ddot{Q}$, the second time derivative of the quadrupole moment of the source, and if it is to carry away energy it must decay as $(1/r)$, where r is the distance to the source. Dimensional analysis using the constants of general relativity then gives the field strength to be $h \sim (G/c^4)\ddot{Q}/r$, where G is the gravitational constant and c is the speed of light. The quadrupole moment is of order $Q \sim MR^2$, where M is the mass and R the size of the source. Therefore $\ddot{Q}$ is roughly that fraction of the kinetic energy associated with the quadrupolar, or non-spherical, motion of the source, ${E_{\rm kin}}^{\rm ns}$:

$$h \sim \frac{G}{c^4}\frac{E_{\rm kin}^{\rm ns}}{r} \sim 10^{-20}\left(\frac{E_{\rm kin}^{\rm ns}}{M_\odot c^2}\right)\left(\frac{10\,{\rm Mpc}}{r}\right). \qquad (6)$$

It is clear that a source in the Virgo Cluster, 10 Mpc distant, could not be expected to radiate gravitational radiation having a strength larger than $h \sim 10^{-20}$ at the earth. It is also clear that terrestrial sources produce hopelessly small strains.

More detailed estimates of wave strengths can be made and applied to specific types of sources; Thorne (1987) gives a review of such calculations. Sources of gravity waves can be classified in three ways: burst, periodic, and stochastic sources.

Burst sources produce waves lasting only a few cycles and include coalescing compact binaries (neutron-stars and black-holes), supernovae and other stellar collapses, and the infall of massive objects to a black hole. For the collapse accompanying a supernova, for example, the field strength at a distance r from the source in terms of the total energy ΔE_{GW} emitted in gravitational radiation and the characteristic frequency f of the collapse, is estimated to be (Thorne 1987):

$$h \sim 3 \times 10^{-20} \left(\frac{\Delta E_{GW}}{M_\odot c^2} \right)^{1/2} \left(\frac{1\,\mathrm{kHz}}{f} \right)^{1/2} \left(\frac{10\,\mathrm{Mpc}}{r} \right). \tag{7}$$

A supernova in the Virgo cluster might produce an $h \sim 2 \times 10^{-22}$ if the gravitational wave output is 10^{-4} solar masses and is radiated at 1 kHz.

Periodic sources produce sinusoids (or combinations of sinusoids) that last for long times and include rotating neutron stars and binary stars. A non-axisymmetric neutron star of ellipticity ϵ, rotating with a frequency f at a distance r will produce a gravity wave amplitude of (Thorne 1987):

$$h \approx 8 \times 10^{-20} \epsilon \left(\frac{f}{1\,\mathrm{kHz}} \right)^2 \left(\frac{10\,\mathrm{kpc}}{r} \right). \tag{8}$$

Ignorance of the ellipticities of known pulsars prevents the accurate prediction of their radiation field strength, but as an example, a pulsar with a not unreasonable ellipticity of $\epsilon = 10^{-6}$ at a distance of 10 kpc (the distance to the center of our galaxy) and rotation frequency of 500 Hz would produce a strain of $h \approx 2 \times 10^{-26}$. This is very small but the fact that the signal is periodic would enable the experimenter to use a long integration time and optimal filtering.

Finally, stochastic radiation is a random noise of gravity waves as might have been produced by some cosmological event in the early evolution of the universe. The existence and strength of these sources are very uncertain; see Thorne (1987) for a review.

The frequencies of gravity waves emitted by some of the strongest sources have already been alluded to. The highest frequency waves would come from stellar collapses to neutron stars or black holes, emitting radiation in a burst containing frequencies up to about 10 kHz. The low frequency limit will come not from the sources, which emit waves down to very low (sub-millihertz) frequencies, but from the ability to isolate the detectors from the earth's vibrations, and ultimately from the unshieldable gravitational gradients arising from density fluctuations in the earth and atmosphere (Saulson 1984).

1.3 Physics of interferometers

Effect of a gravity wave on an interferometer. Fig. 1.1 reveals the basic idea of using an interferometer to detect gravity waves. Consider the diagram for the '+' polarization wave. The test mass at the origin is the beamsplitter and the test masses lying on the positive x and y axes are mirrors forming the arms of a Michelson interferometer. All masses are hung from pendula so that they are free to move at frequencies above their pendulum resonance. The light measures the proper distance as shown in Fig 1.1. If a gravity wave passes in the z direction, one arm will lengthen and the other will shorten. The light beams in the two arms will then accrue a relative phase shift as they travel from the beamsplitter to the arm end mirrors and back to the beamsplitter. When the beams recombine this phase shift will produce a shift in the interference fringe, and the resulting intensity change is a measure of the gravity wave strength.

If each arm is of length l (the distance from the beamsplitter to an arm end mirror) then for one phase of the gravity wave the changes in the x and y arm lengths will be $\Delta l_x = \frac{1}{2}hl$ and $\Delta l_y = -\frac{1}{2}hl$. The optical path length change in each arm is thus hl, and so the relative phase change between the two interfering beams is $\Delta\phi_d = 4\pi hl/\lambda$. (This is correct only for gravity wave periods much greater than the arm transit time; the frequency response of interferometric detectors is treated below.)

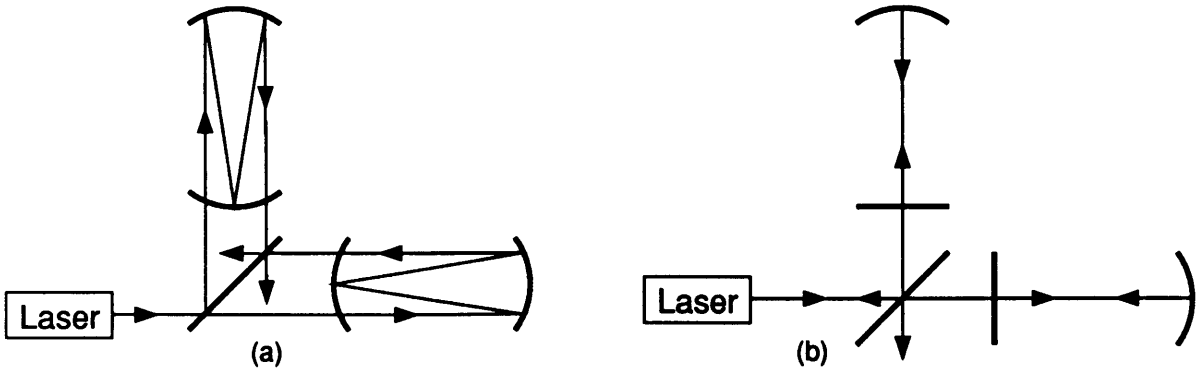

Fig. 1.2 The two light storage methods used in prototypes: (a) Delay line, (b) Fabry-Perot cavity.

For a given wave amplitude h, the arm length change (dl) can be made larger by increasing the arm length (dl=$hl/2$). The phase shift per arm for a given arm length change ($d\phi/dl$) can be made larger by arranging for the light to be stored in the arms of the interferometer, so that the light samples the mirror displacement more than once. (For the simple one-pass arrangement, ($d\phi/dl$)=$4\pi/\lambda$). Two such storage schemes have been used in prototypes. Figure 1.2a shows a delay-line interferometer, where each beam makes $2b$ distinct passes (only four are shown) in an arm before it interferes at the beamsplitter. This arrangement has a length-to-phase conversion of $d\phi/dl = 4\pi b/\lambda$, where b is also the number of spots on each end mirror. The

other scheme, Fig. 1.2b, uses a resonant Fabry-Perot cavity as the storage element in each arm. Here the end mirrors are of maximum reflectivity and the near mirrors have some transmission, T_1. For small deviations from resonance, the Fabry-Perot has a length-to-phase conversion of $d\phi/dl = 8F/\lambda \approx 16\pi/T_1\lambda$, where F is the finesse of the cavity (see Appendix A).

Frequency and angular response. The optical phase shift is increased by increasing the arm storage time only up to a point: if the storage time is longer than half the gravity wave period, then the phase shift built up during one half-cycle of the wave will be removed during the next half-cycle. Clearly for the delay line (or single arm mirror) case, if the arm storage time is equal to an integral number of gravity wave periods there is no net phase shift. The frequency response of such an interferometer is computed as follows. Consider a gravity wave of amplitude $h = h_0 e^{i\omega t}$, optimum polarization and normally incident upon the detector, whose arms lay on the x and y axes. The space-time interval for a photon, $ds^2 = g_{\mu\nu}dx^\mu dx^\nu = 0$, to first order in h takes the form, $cdt = \left(1 \pm h_0 e^{i\omega t}\right)dx$. The $+$ sign applies to one of the axes and the $-$ sign to the other. For each arm, this must be integrated along the light path as the light makes the round trip from the beamsplitter. The integral can be done over the arm storage time, τ_s=$2bl/c$. The differential phase shift between the two beams is then

$$\delta\phi_d = \int_{t-\tau_s}^{t} \omega_0 h_0 e^{i\omega t} dt = \frac{2\omega_0 h_0 \sin(\omega\tau_s/2)}{\omega} e^{i\omega(t-\tau_s/2)} = \tau_s \omega_0 \mathrm{sinc}(\omega\tau_s/2) h_0 e^{i\omega(t-\tau_s/2)} , \tag{9}$$

where ω_0 is the light frequency and sinc(x)=sinx/x. The transfer function of the differential phase to a gravity wave, $\delta\phi(f)/h(f)$, thus has amplitude

$$\left|\frac{\delta\phi}{h}\right|_{DL} = \tau_s \omega_0 \mathrm{sinc}(\omega\tau_s/2) , \tag{10}$$

and a phase factor $e^{-i\omega\tau_s/2}$.

For the Fabry-Perot arm configuration, the transfer function is found by adding the phase contributions generated on each of the infinite number of round trips. This is done in Appendix A, and gives, in the limit where the length of the interferometer is small compared to the gravitational wavelength ($f \ll l/c$),

$$\left|\frac{\delta\phi}{h}\right|_{FP} = \frac{(4\omega_0\tau_s)}{\sqrt{\left(1+(2\omega\tau_s)^2\right)}} , \tag{11}$$

where the storage time is $\tau_s = Fl/c\pi \approx 2l/cT_1$. The two transfer functions are shown in Figure 1.3; the storage times are picked so that the low frequency sensitivities are the same. Note that for high frequencies, $\omega\tau_s \gg 1$, the response becomes

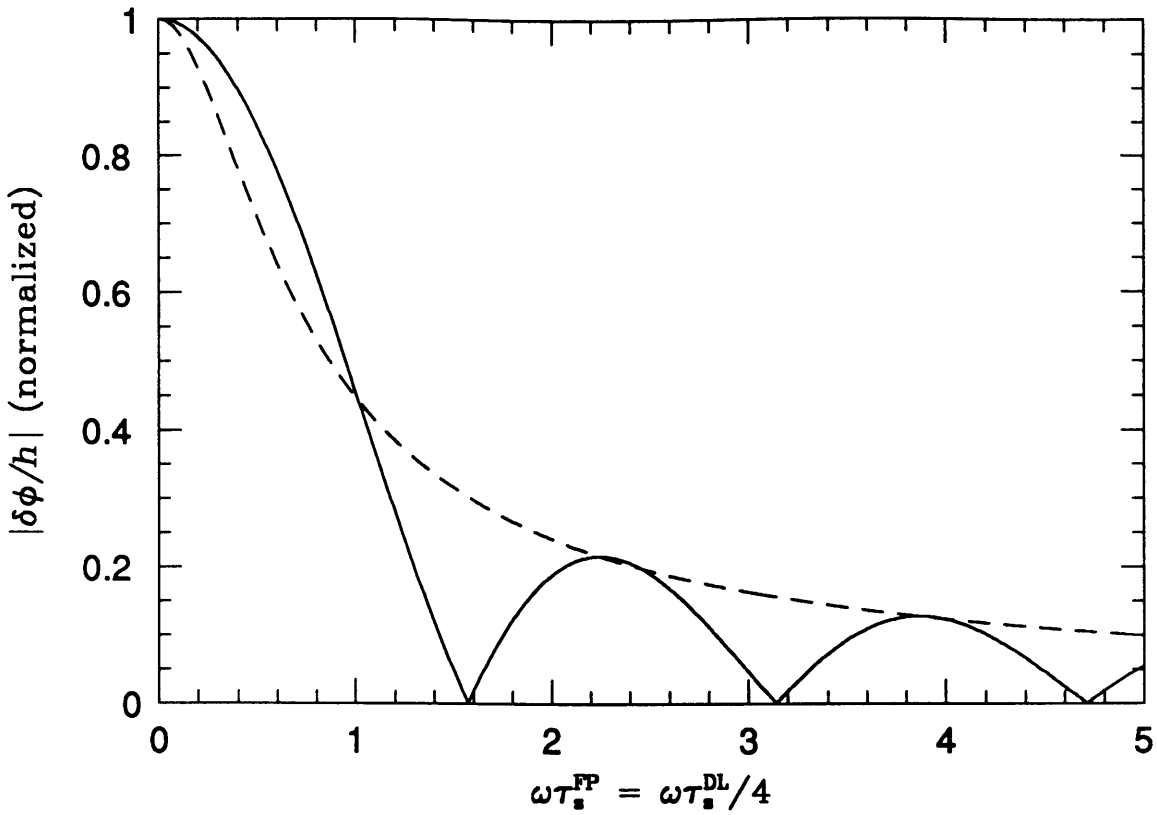

Fig. 1.3 Transfer functions for the delay-line (solid curve) and Fabry-Perot (dashed line) interferometers. The low frequency sensitivities are set to be equal by choosing $\tau_s^{FP} = \tau_s^{DL}/4$.

independent of the storage time; it saturates at a level of $|\delta\phi/h| = 2\omega_0/\omega$ for both types of detector.

If the gravity wave is not normally incident on the detector and contains both '+' and '×' polarizations, the relative arm length change will be reduced. If the detector has its arms along the x and y axes, and the wave vector has polar angles (θ,ϕ) the wave-induced relative arm length change is

$$\Delta l/l = \tfrac{1}{2}(1+\cos^2\theta)\cos 2\phi\, h_+ + \cos\theta \sin 2\phi\, h_\times \,. \tag{12}$$

The angular response is quite broad. For unpolarized gravity waves, the response is zero only for $\theta=\pi/2$, $\phi=n\pi/4$.

Noise sources: the shot-noise limit. The sensitivity of an interferometer depends not only on the conversion of gravitational wave strain (mirror displacement) to optical phase shift, but also on the ability to measure the optical phase. At best, the ability to measure the phase is limited by photon counting statistics. The laser light can be described by a coherent state, for which the counting statistics follow a Poisson distribution. Applying the Weiner-Kinchine theorem to this random arrival of photons at the photodetector gives the amplitude spectral density of the photon arrival rate to be $\delta\dot{n}(f) = \sqrt{2\langle\dot{n}\rangle}$, in units of (number per unit time)/$(\text{Hz})^{1/2}$. If the average laser power incident on the photodetector is $P_{\rm dc}$ and the photodetector

quantum efficiency is η, then the detected photon rate is $\langle \dot{n} \rangle = \eta P_{\rm dc}/{\rm h}\nu$, where h is Planck's constant. The amplitude spectral density of the power fluctuations is then $\delta P(f) = \sqrt{2{\rm h}\nu P_{\rm dc}/\eta}$.

The equivalent phase noise due to the shot noise depends on the specific technique used to detect the signal; two such techniques, in-line and external modulation, are discussed later in this thesis. The simplest, though impractical, technique is to operate the interferometer at the fringe half power point and measure directly the power fluctuations. This is not a practical technique because in a real laser the amplitude is not shot-noise limited in the gravity wave frequency band, and it is difficult to subtract out the amplitude noise to a level where shot-noise dominates. In addition, middle-of-the-fringe operation is incompatible with the technique of recycling, discussed in section 1.6. Nevertheless, given a perfect laser, the phase sensitivity of this theoretical interferometer represents a maximum phase sensitivity for any signal detection technique, and so it is interesting to analyze.

In an interferometer with no loss and perfect interference between the two arm beams, the power at the anti-symmetric output in terms of the differential arm phase is

$$P = \frac{1}{2} P_0 (1 - \cos \phi_d) \,, \tag{13}$$

where P_0 is the input power. The maximum slope occurs at $\phi_{\rm d}{=}\pi/2$ and is equal to $dP/d\phi_d = \frac{1}{2}P_0$. The sensitivity can be doubled by also detecting the light at the symmetric output, which, since it is also at the $P{=}(1/2)P_0$ point, has $dP/d\phi_d = \frac{1}{2}P_0$. The total detected power is then P_0, giving an equivalent phase sensitivity of

$$\delta\phi_d(f) = \left(\frac{d\phi_d}{dP}\right)\delta P(f) = \sqrt{\frac{2{\rm h}\nu}{\eta P_0}} \quad \left({\rm radians}/\sqrt{\rm Hz}\right). \tag{14}$$

In terms of the photocurrent, $I{=}\eta P(e/{\rm h}\nu)$, this is $\delta\phi_d(f) = \sqrt{2e/I_0}$, where e is the electron charge and I_0 is the photocurrent on a bright fringe. As an example, for an effective laser power of $\eta P{=}1$ watt, and $\lambda{=}0.5$ μm (green) light, the shot-noise equivalent phase fluctuations are $\delta\phi_d(f) = 8.9 \times 10^{-10}$ rad/$\sqrt{\rm Hz}$; this implies the ability to measure a phase shift of 10^{-9} of a fringe in a one second integration time. The shot noise limited sensitivity to a gravity wave strain is then $h(f) = |\delta\phi/h|^{-1}\delta\phi_d(f)$, with $|\delta\phi/{\rm h}|$ as given for the two types of detectors. The sensitivity to a *signal* improves with the square root of the allowed integration time, which depends on the length and type of the signal.

Noise sources: thermal and seismic noise. The measurement of the optical phase does not of course discriminate the source of the phase shift: it is necessary not only to have good phase sensitivity but also to reduce the effects of any phenomena (other than gravity waves) capable of producing a phase shift. The most important noise sources in addition to shot noise are thermal and seismic noise. Both produce random motions of the mirrors; the effect of these noise sources on the strain

sensitivity, assuming they act independently at the end points, is thus inversely proportional to the interferometer arm length.

The fluctuation-dissipation theorem states that any dissipative system will experience thermally driven fluctuations in its modes. Such thermal noise effects arise in two places in an interferometer: through dissipation in the flexure of the suspension systems used to make the mirrors 'free' for frequencies higher than the pendulum resonance; and through dissipation of the internal modes of the mirrors. In the gravity wave frequency band, the suspension thermal noise is due to above-resonance excitation of the fundamental mode, and the mirror internal thermal noise comes from below-resonance motion. The quantitative behavior depends on the materials used (see Saulson 1990), but in general the thermal noise contribution to the mirror motion varies as $\delta x(f) \propto \sqrt{\mathrm{T/mQ}}$, where T is the temperature, m the mass and Q the quality factor of the oscillator.

Seismic noise is simply the motion of the ground transmitted through the isolation and suspension system to the mirrors. The ground noise spectrum varies from site to site. In the lab at MIT, the ground motion is roughly $\delta x(f) = 10^{-7}\mathrm{m}/\sqrt{\mathrm{Hz}}$ from 1 Hz to 10 Hz; at 10–100 Hz the spectrum falls as $(1/f)^4$. At quieter spots typical of a potential long-baseline interferometer site, the ground motion at 1–10 Hz is $\delta x(f) = 10^{-9}\mathrm{m}/\sqrt{\mathrm{Hz}}$, falling as $(1/f)^2$ above 10 Hz. The ground noise is filtered above about 1 Hz by the mirror suspension, and by many orders of magnitude near 100 Hz and above by several layers of mass-spring isolators. Designing and building an isolation system which will provide adequate filtering is the subject of current research. The ground noise at the points of support of the mirrors is nearly uncorrelated, so if the mirror motion due to ground noise is $\delta x_{\mathrm{m}}(f)$, the equivalent strain noise is $h(f) \approx 2\delta x_{\mathrm{m}}(f)/l$.

It is expected that seismic noise will dominate the noise of a long-baseline interferometer at frequencies below about 50 Hz. The suspension thermal noise is likely to dominate at mid-frequencies, in the 50–150 Hz region. At higher frequencies, the noise will be dominated by photon shot noise.

Other noise sources, the standard quantum limit. There are of course other noise sources which, though not expected to be a limiting noise source in an initial large baseline interferometer, could become limiting if the already mentioned noise sources are much reduced. Fluctuations in the number of gas molecules in the optical beam path produce fluctuations in the optical phase and thus put a requirement on the vacuum level. Phase noise from residual gas is found to scale as $1/l^{3/4}$. Fluctuating gravitational gradients due to density fluctuations in the earth and atmosphere produce uncorrelated mirror motions above a few Hertz. The equivalent strain noise scales as $1/l$, but for realistic arm lengths of a few kilometers this unshieldable noise source sets a lower limit of about 10 Hz on the gravity wave band of an earth-based detector. These noise sources are shown in Figure 1.4 in section 1.5. Noise sources associated with optical phenomena are discussed in chapter 2.

In chapter 2 the random forces on the mirrors due to laser intensity fluctuations are discussed. These initially symmetric power fluctuations produce differential mirror motions through imbalances in the system. There are also inherently asymmetric radiation pressure fluctuations that are responsible for what is known as the standard quantum limit of an interferometer. The full explanation of the effect was first given by Caves (1980, 1981). The field in each arm is a superposition of the single mode laser field and the vacuum fluctuations in that mode, uncorrelated in the two arms, which enter through the anti-symmetric port of the beamsplitter. That part of the intensity due to the cross term between these two fields exerts a fluctuating radiation pressure on the mirrors. In a cavity arm interferometer, the equivalent strain noise due to this effect is $h(f) = \sqrt{P_0 \mathrm{h}\nu}/\pi^2 c T_1 l m f^2$, where m is the mirror mass, P_0 is the power incident on the beamsplitter, and ν is the optical frequency. The radiation pressure noise is proportional to the square root of the optical power while the shot noise is inversely proportional to the square root of the power, so there exists a minimum in the total noise due to optical field fluctuations. With this optimum power (which is much larger than that available with current technology), the quantum noise limited strain sensitivity is

$$h(f) = \sqrt{\frac{\mathrm{h}}{\pi m}} \frac{1}{\pi l f} \approx 3.6 \times 10^{-24} \left(\frac{10\,\mathrm{kg}}{m}\right)^{1/2} \left(\frac{4\,\mathrm{km}}{l}\right) \left(\frac{100\,\mathrm{Hz}}{f}\right). \qquad (15)$$

This is known as the standard quantum limit. It will not be a limiting noise in initial long baseline detectors.

1.4 Overview of prototype interferometers

An interferometer built with suspended and seismically isolated masses and operating in vacuum, but with laboratory sized arm lengths, is what I call a prototype gravity wave interferometer. While such interferometers do not have the length necessary for a realistic chance of gravity wave detection, they are vital for developing many aspects of the technology and understanding the noise sources. The major noise sources limiting the phase and position (mirror motion) sensitivity of an interferometer do not depend on the arm length, so it is possible to investigate these noise sources at the level they will affect a large baseline interferometer's phase and displacement sensitivity.

In addition to studying noise behavior, a prototype interferometer is used to develop techniques for servo-control of the detector's alignment and interferometric length, detecting the differential phase shift at the anti-symmetric output, damping the pendulum modes of the suspended mirrors, stabilizing the laser frequency, ... the list goes on.

The list of current prototype interferometers consists of two with Fabry-Perot cavities in the arms and two using delay lines. The Fabry-Perot interferometers are being operated at Caltech, where the arm length is 40 m, and at the University of Glasgow, where the arm length is 10 m. Both systems are not in fact Michelson interferometers. The beams reflected from the arm cavities are not recombined and

interfered at the beamsplitter. Instead, the laser frequency is locked to the resonance of one of the arm cavities and the difference between the locked laser frequency and the resonance of the other arm cavity is a measure of the differential arm length (Spero 1986). The best position sensitivity attained at Caltech is 1×10^{-18} m/$\sqrt{\text{Hz}}$ for frequencies near 800 Hz. The system at Glasgow has reached a sensitivity of 1.2×10^{-18} m/$\sqrt{\text{Hz}}$ over a 1 kHz bandwidth around 2 kHz (Ward et al. 1987).

The delay line interferometer at the Max-Planck-Institut in Garching has an arm length of 30 m. The equivalent displacement sensitivity of this detector has reached the 2.5×10^{-18} m/$\sqrt{\text{Hz}}$ level for nearly all frequencies above 1 kHz, limited by photon shot noise with 0.23 W of bright fringe power (Shoemaker et al. 1988). The delay line prototype at the Institute of Space and Astronautical Science, Tokyo is modeled after the MPI detector and has a 10 m arm length. Kawamura et al. (1989) report a maximum position sensitivity of 1.6×10^{-17} m/$\sqrt{\text{Hz}}$ at frequencies near 2 kHz. A 0.5 m arm length delay line prototype was built at MIT and operated until 1987, achieving a sensitivity of 6×10^{-17} m/$\sqrt{\text{Hz}}$ at frequencies above 6 kHz (Livas et al. 1986).

1.5 Specifications of a long-baseline interferometer

Most of the gravity wave strength estimates presented in section 1.2 are very uncertain due to ignorance of the rate of occurrence – or even the existence – of the sources, or lack of knowledge of the efficiency of a process. The most certain source is the coalescence of neutron star binaries in distant galaxies, so the consideration of such a source is a one way to arrive at a sensitivity goal for a long base line interferometer.

The coalescence will produce a gravitational wave chirp, with frequencies sweeping from tens of Hertz to 1 kHz in a few minutes. The rate of such events is estimated to be three per year if one looks out to a distance of 100 Mpc; the strength of the waves produced at such a distance is estimated to be $h \sim 10^{-21}$, nearly independent of frequency, for a typical binary. In order for two separated interferometers to detect such a source, the wave amplitude must be about a factor of 10 larger than the interferometer sensitivity, $h_{\text{detection}} \simeq 10 h_{\text{rms}}$. This factor of 10 ensures a statistically significant detection of bursts, considering them to occur at a rate of three per year, with random polarizations and arrival directions, in detectors which are free from non-Gaussian noise bursts.

To detect a coalescence at 30 Mpc, the sensitivity would have to be $h \simeq h(f)\sqrt{\text{BW}} \leq 3 \times 10^{-22}$ (the factor of 10 margin has been assumed though the rate for events of this amplitude will probably be less than three times a year). With a detection bandwidth of BW $\sim$ 100 Hz, the interferometer strain sensitivity must be $h(f) \lesssim h/\sqrt{\text{BW}} \approx 3 \times 10^{-23}/\sqrt{\text{Hz}}$ at frequencies around 100 Hz.

The interferometer must be long enough so that the random forces on the mirrors do not prohibit reaching this sensitivity level. Given the level of seismic and (suspension) thermal noise, this requires an arm length of at least a few kilometers. The arm light storage time should be made no longer than the half-period of the

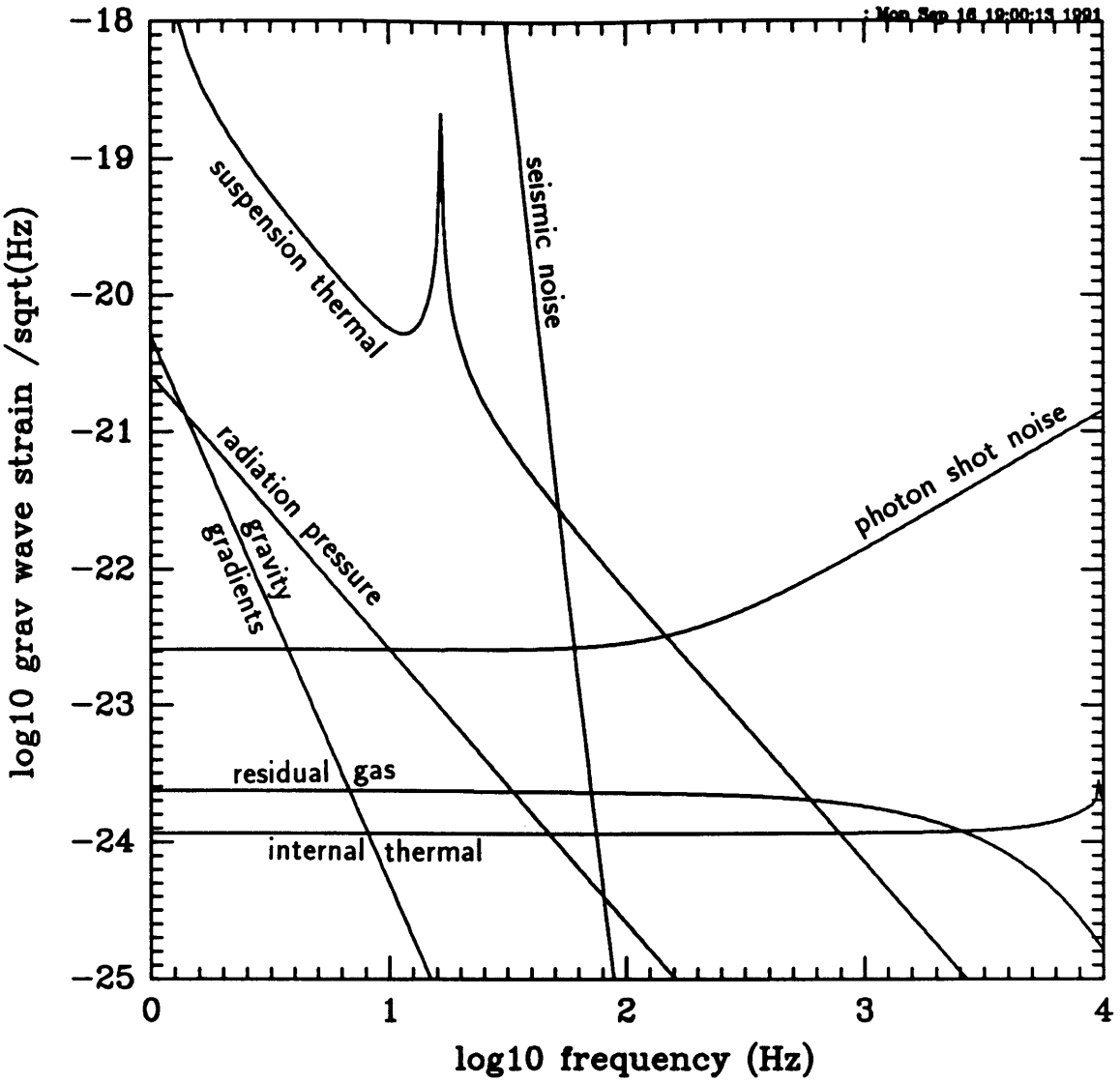

Fig. 1.4 Spectra of noise sources that will limit the sensitivity of a LIGO interferometer. The arm length is 4 km and the cavity storage time is $\tau_s = 0.44$ msec. The shot-noise is due to a circulating light power (i.e. power at the beamsplitter) of 45 W (resulting from an input power of 1.5W and a recycling gain of 30, e.g.) and wavelength $\lambda = 0.51$ μm. The seismic noise is due to the typical ground noise spectrum, as given in the text, filtered by 5 stages of passive isolation and the mirror pendulum, $f_0 = 1$ Hz. The mirror internal thermal noise is that of a 10 kg, Q=10^6, viscously damped test mass. The pendulum thermal noise comes from a Q=10^7, viscously damped pendulum (the vertical resonance of the pendulum shows up at 16 Hz). The gas noise is due to 10^{-8} torr of N_2.

frequency at which shot-noise no longer dominates. Choosing a knee frequency for a Fabry-Perot system of $f_k = 1/4\pi\tau_s \approx 200$ Hz gives a strain to phase conversion, for an optical wavelength of 0.5 μm, of $|\delta\phi/h|_{f\leq 200\text{Hz}} \approx 4\omega_0\tau_s = 6 \times 10^{12}$ rad. The required phase sensitivity to reach the above strain sensitivity is thus $\delta\phi_d(f) = |\delta\phi/h|\, h(f) \approx 2 \times 10^{-10}\,\text{rad}/\sqrt{\text{Hz}}$. At the minimum, this requires an effective optical power of $\eta P = 2\text{h}\nu_0/(\delta\phi_d(f))^2 \approx 20$ W.

The design of the initial interferometer for the Laser Interferometer Gravitational-wave Observatory (LIGO) uses a 4 km arm length and Fabry-Perot cavities as the storage elements in the arms (Vogt 1989). The beams will be optically recombined rather than separately detected as in current prototypes. An advantage of the Fabry-Perot design is that the required mirror diameter is smaller than for an equally long delay line; more interferometers can then be operated in the same vacuum system. The storage time of the arms will be $\tau_s = 0.5$–1 msec, giving a 3 dB frequency of $f_k = 100$–200 Hz. Figure 1.4 shows how the noise sources discussed in section 1.3 will limit the performance of a LIGO interferometer.

Another basic requirement of a gravity wave detector is that there be more than one interferometer being operated at widely separated sites. Nobody will believe a claimed gravity wave detection unless the signal appears in the output of more than one interferometer; a separation of the order of the size of the continental United States should ensure that any non-gravity wave effects capable of producing signals will be uncorrelated at the two sites. A wide separation also makes it easier to get information on the source location from the relative timing of the two signals.

1.6 Techniques for increasing strain sensitivity

The interferometer designs discussed up until know could be called first generation designs; they consist of a Michelson interferometer with either delay lines or Fabry-Perot cavities as the storage elements. Second generation designs include one or more proposed techniques for increasing the sensitivity to a gravity wave strain, $h(f) = |\delta\phi/h|^{-1}\delta\phi_d(f)$, capitalizing either on an increase in the effective light power and thus a decrease in $\delta\phi_d(f)$, or on increase in the conversion of strain to phase shift, $|\delta\phi/h|$. Many of these techniques are discussed by Vinet et al. (1988).

The technique of standard or broadband recycling, suggested by Drever (1982), adds another mirror to the interferometer at the input to the system, making the entire interferometer into a resonant cavity. This increases the circulating power in the arms by at most the reciprocal of the total interferometer loss, thereby increasing the shot noise limited phase sensitivity by the square root of this factor, without altering the bandwidth of the interferometer. Light recycling, as it is also called, has been tested on a small one-bounce Michelson interferometer by Man et al. (1990). The technique of broadband recycling, as applied to a Fabry-Perot interferometer, is the subject of chapters 4 and 5 of this thesis.

The idea behind both resonant and dual recycling is to make the interferometer resonant not only at the laser frequency ν_0 (as in broadband recycling), but also at a frequency $\nu_0 + f_g$ (or $\nu_0 - f_g$), where f_g is the gravity wave frequency. That is, the interferometer is resonant at the carrier and at one of the gravity wave induced sidebands of the carrier. This sideband is thus resonantly enhanced by a factor corresponding to the finesse of the sideband resonator. The increase in the phase shift (signal) occurs of course only at and around a single gravity wave frequency. The bandwidth of the system is then determined by the finesse (i.e. the losses) of

the sideband resonator, and is roughly $\Delta f_g \approx 1/\tau_{sb}$, where τ_{sb} is the storage time of the sideband in the interferometer.

This narrow-banding idea and a method for implementing it known as resonant recycling were first suggested by Drever (1982). An alternate optical configuration for producing the two resonances (at the carrier and the gravity wave sideband) due to Meers (1988) is known as dual recycling. Narrow band operation of a detector would be useful for the detection of periodic sources and a stochastic background of gravitational waves. Since all types of recycling depend on the total interferometer optical loss being low, they are useful for increasing the sensitivity to gravitational waves only in a large baseline interferometer (see chapter 4.2). Strain and Meers (1991) have tested dual recycling on a small one-bounce Michelson interferometer.

A suggestion for circumventing the photon shot noise limit by using light with modified statistical properties has been made by Caves (1981). The vacuum fluctuations responsible for the radiation pressure fluctuations mentioned above can also be blamed for the shot noise. Caves has shown that by 'squeezing the vacuum' (i.e. reducing the fluctuations in one component of the field while increasing the fluctuations in the quadrature component), the photon shot noise can be reduced in exchange for increasing the radiation pressure fluctuations. The technique has the same effect has increasing the laser power. The increase in sensitivity achievable depends on the optical configuration of the interferometer; see Gea-Banacloche and Leuchs (1987) for further discussions of squeezed states applied to interferometers. The many practical difficulties involved probably put this technique into the category of third generation designs.

1.7 Purpose of this work and thesis outline

There are a number of optical and electronic techniques being planned for use in a long baseline interferometer that had not been tested in an interferometer. A prototype interferometer (in vacuum and with isolated, hanging masses) is not necessary for the investigation of many of these techniques. A relatively small interferometer with mirrors fixed to the ground (optical table) and operating in air is useful for tests which do not require being able to achieve a gravity-wave-detector level of shot-noise limited position sensitivity in the gravity wave band. This thesis discusses work done on such a fixed-mirror interferometer in investigating some of these heretofore untested techniques.

Some noise sources affect a fixed-mirror interferometer in the same way as a gravity wave interferometer; these usually involve optical imperfections creating phase noise. Chapter 2 discusses how the noise behavior of the laser influences the sensitivity of an interferometer.

A long baseline Fabry-Perot interferometer requires optical recombination of the beams if recycling techniques are to be used. Chapter 3 discusses an experiment on optical recombination using the technique of 'in-line modulation'.

A long baseline interferometer requires at least 30 W of effective light power (see section 1.5). This much power in a single frequency is not available with Argon lasers; the LIGO plans on achieving this with an input power of $\sim$ 1.5W and a factor of 30 enhancement gained from broadband recycling. The subject of chapters 4 and 5 is recycling: chapter 4 presents the theory of broadband recycling and chapter 5 discusses the results of experiments on a recycled Fabry-Perot arm (fixed-mirror) interferometer.

The in-line modulation technique of chapter 3 is a convenient means of generating a signal at the interferometer output that is proportional to the differential arm phase. Limitations of the electro-optic phase modulators used in the interferometer arms make this technique unsuitable for recycling. Chapter 6 presents the theory and experimental results of a more practical method of extracting the phase shift (or gravity wave signal) called 'external modulation'.

Throughout the thesis remarks are made about the application and scaling of the techniques investigated in these experiments to a full-scale gravity wave detector. Some final comments on this topic and a summation of the thesis are made in the final chapter.

2 The laser and its noise behavior

2.1 The laser

A Michelson interferometer is designed to be sensitive to the optical phase difference between its arms and thus in principle is insensitive to common-mode fluctuations of the input light. This insensitivity is impossible to achieve in practice. In general, an asymmetry between the two arms permits fluctuations in the input light to couple to the output signal. This chapter describes the various types of fluctuations of the laser light source and the ways in which these fluctuations can appear in the interferometer output.

The laser used in all of the experiments is an Ar^+ ion laser, specifically a Spectra-Physics model 2020–05. A wavelength selective (narrow bandpass) output coupling mirror allows only the 514.5 nm line to oscillate. An intra-cavity etalon performs further wavelength selection so that only one longitudinal mode has sufficient gain to lase. Finally, an intra-cavity aperture restricts the output spatial mode to be TEM_{00}. The base laser thus emits an electromagnetic field at a single frequency.

2.2 Frequency fluctuations

This frequency is not constant in time, however, due to fluctuations in the optical path length of the laser cavity. These frequency fluctuations can couple into the output signal of the interferometer in the following ways: via a static storage time difference in the two arms, and through the interference of scattered light with the main beam. In a Fabry-Perot arm interferometer, light that is not matched to the fundamental modes of the cavities can also serve to convert frequency noise to an output signal.

In each case, the fields which are compared at the beamsplitter originated from the laser at different times, and a fluctuation of the laser field phase (or frequency) is converted into a fluctuation of the differential arm phase. An interferometer arm converts a frequency fluctuation, $\delta\nu$, into a phase fluctuation by $\delta\phi = (d\phi/d\nu)_{\rm arm}\delta\nu$. For a delay line $(d\phi/d\nu) = 2\pi bl/c$ where l is the arm length and b the number of bounces, while for a cavity $(d\phi/d\nu) = 8lF/c$ where F is the finesse of the cavity. A storage time asymmetry in the arms then results in a differential arm phase, which for a cavity system can be written as:

$$\delta\phi(f) \approx \left\langle \left(\frac{d\phi}{d\nu}\right) \right\rangle \left[\frac{\Delta l}{\langle l \rangle} + \frac{\Delta F}{\langle F \rangle}\right] \delta\nu(f) \,. \tag{16}$$

For the cavities in these experiments, $(d\phi/d\nu) = 2.8 \times 10^{-6}$ rad/Hz. If the cavities are matched to 1%, this gives $\delta\phi(f) = 2.8 \times 10^{-8}\,\delta\nu(f)$.

Frequency noise can also corrupt the system through the phase fluctuations produced by the interference between the main beams and scattered light (light that has taken a different path to get to the output). If a stationary scattering site scatters a fraction σ of the main field into the detected beam, and this scattered light interferes with the main beam after a time different than the arm storage time by a factor γ, it will contribute a differential arm phase of

$$\delta\phi(f) \sim 2\pi\sigma(\gamma\tau_{\rm st})\delta\nu(f) \approx (1/4)(d\phi/d\nu)(\sigma\gamma)\delta\nu(f) \,. \tag{17}$$

The product $(\sigma\gamma)$ for any system is probably less than the fractional imbalance in the arms, so that the scattering contribution is less than the asymmetry contribution. For an interferometer with cavities in the arms, light that is not coupled into the cavities (higher order modes) contributes in a similar way; in this case σ is the fractional difference (relative to the main beam) between the unmatched light in the two arms, and f will be nearly one since the higher order modes travel only to the near mirrors of the cavities. In theory, both of these effects can be reduced by detecting only the signal in the spatial mode of the main beam, through the use of an output filter-cavity or single-mode fiber.

2.3 Frequency stabilization

This sensitivity requires that the frequency noise be sufficiently small so that it does not compromise the sensitivity in the frequency regime where measurements are being made: for our fixed mass prototype this is in the tens of kilohertz, for LIGO this is the region from 100 Hz to a few kilohertz. The frequency noise of an unstabilized Ar^+ laser does not in general satisfy this requirement. In fact the frequency fluctuations of an unstabilized Ar^+ ion laser are much greater than the fluctuations of the resonant frequency of a typical passive optical Fabry-Perot cavity, such as used in the interferometer arms, at all but very high frequencies. It is thus also desirable to pre-stabilize the frequency to such a cavity to reduce the frequency fluctuations of the field incident upon subsequent optical cavities.

Small reductions of the frequency fluctuations at low frequencies ($\leq$ 100 Hz) can be made by quieting the water flow that cools the laser tube, but for substantial reductions the frequency must be actively stabilized. In these experiments the laser frequency is stabilized to a reference Fabry-Perot cavity using a technique that has become known as 'Pound-Drever reflection locking' (Drever et al. 1983). This is a well developed technique which uses the frequency-dependent field reflected from a cavity to derive an error signal proportional to the instantaneous frequency fluctuation of the laser; this error signal is then used to control the laser frequency. This technique is discussed, in addition to Drever et al., in Salomon et al. (1988) and Hamilton (1989); the scheme has been applied to argon lasers (Kerr et al. 1985), dye lasers (Hall and Hänsch 1984, Hough et al. 1984), He-Ne lasers (Salomon et al. 1988) and Nd:YAG lasers (Shoemaker et al. 1989). Appendix A presents the response of a Fabry-Perot cavity to an electric field and shows how a discriminant for the laser frequency/cavity length is generated. The purpose of the discussion here is to document the particular servo system used for these experiments, since, as is clear from the numerous references, there are many ways of implementing the technique.

Figure 2.1 shows the optics and electronics used to stabilize the laser frequency. A Pockels cell is mounted in the laser cavity to provide wideband control of the cavity

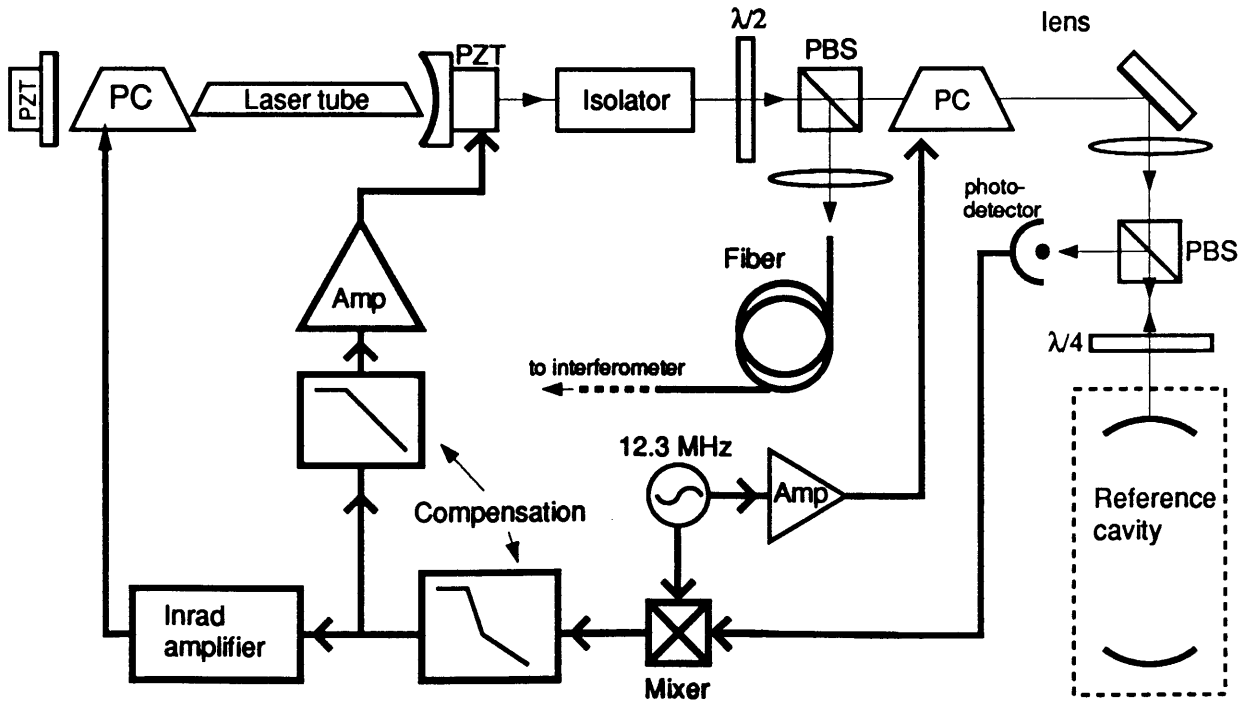

Fig. 2.1 Laser frequency stabilization (PC is a Pockels cell and PBS is a polarizing beamsplitter)

optical path length; it is made of a Brewster angle cut pair of ADP crystals, Gsänger Optische model PM 25, that produces a phase retardation at 514 nm of $\lambda/2$ for an

applied voltage of 900 V. The introduction of the Pockels cell into the cavity reduces the laser output power by approximately a factor of 2. In this configuration, the laser emits a maximum power of 0.5 W (if the plasma tube is new). The laser mirrors have been removed from the laser frame and mounted directly on the optical table. This allows mounting of both mirrors on piezo-electric transducers, giving further control of the resonator length; the output coupler is mounted on a relatively large range (3 μm motion for 1000 V), 'slow' (f_{rcs} = 4 kHz) three element Burleigh PZT, and the rear mirror is mounted on a small (.95″ diam. x .05″), 'fast' (f_{rcs} = 250 kHz) PZT disc. The 'fast' PZT is not actually used in this implementation of the control loop, but it can be used for high frequency control if one desires to remove the Pockels cell from the cavity.

After exiting the laser, the beam passes through a Faraday isolator and then a half-wave plate and polarizing beamsplitter that are used to control the relative power sent to the reference cavity and the interferometer-feeding fiber. The reference beam is phase modulated (by another PM 25) at f_{mod} = 12.33 MHz with a modulation index of $m \sim 0.3$ before entering the cavity. A f = 50 cm lens matches the laser beam spatial mode to the cavity's fundamental mode. A folding mirror and a rotatable piece of glass allow angle and position alignment, though with an annoying coupling between the two, of the beam to the optical axis of the cavity. The polarizing beamsplitter and quarter-wave plate in front of the cavity direct the reflected beam onto the rf-photodetector. The photodetector output is demodulated, filtered and amplified, and sent to the output coupler PZT and the intra-cavity Pockels cell to complete the loop.

The reference cavity is approximately 30 cm long; the structure which holds the cavity mirrors is made of invar and is wrapped in acoustic shielding. The finesse of the cavity is 200, thus the linewidth (free-spectral range/finesse) of the cavity is about 2.5 MHz. Approximately 70% of the incident light is typically coupled into the TEM_{00} mode of the cavity, limited by alignment. The intensity reflection coefficient of the cavity on resonance is R_{cav}= 0.28.

The rf-photodetector was designed and developed in this lab by Rainer Weiss and Joe Giaime. It uses an EG&G SGD-200 silicon photodiode reverse biased at 100 V. The photocurrent is turned into a voltage with an inductive load which, in parallel with the capacitance of the photodiode, is resonant at the modulation frequency, with a Q of 3–4. Two stages of amplification follow, a cascode FET-transistor stage and an operational amplifier stage. The input noise of the photodetector is equivalent to the shot noise from a DC photocurrent of 35 μA. The photodetector output is (3–pole Butterworth) low-pass filtered at 18 MHz to remove any signal at harmonics of the modulation frequency before entering the Mini-Circuits ZAY-1B double-balanced mixer. The IF output of the mixer is low-passed at 7 MHz to remove any signal remaining at f_{mod}. This error signal is then sent through a compensation network. For the initial locking this is a single pole at 100 Hz; for normal operation, a pole-zero pair at 100 Hz–100 kHz is added and the low frequency gain increased.

In addition, a 1.3 MHz zero compensates for the roll-off of the cavity response. The signal is amplified by a wideband high-voltage (±85 V) amplifier and applied to the intra-cavity Pockels cell; it is also further filtered with a pole at 0.5 Hz, sent through a 0–1000 V range amplifier, and applied to the PZT on the laser output coupler. The maximum unity-gain frequency (u.g.f.) is about 700 kHz with the single-pole compensation, and about 300 kHz with the normal compensation.

Figure 2.2 shows a closed-loop transfer function of the servo operating in the normal state. Because of the large gain at low frequencies, it is difficult to measure the closed-loop response below 5 kHz, but the response must decrease as $1/f^2$ down to 100 Hz. Figure 2.3 shows the spectral density of the frequency noise for the

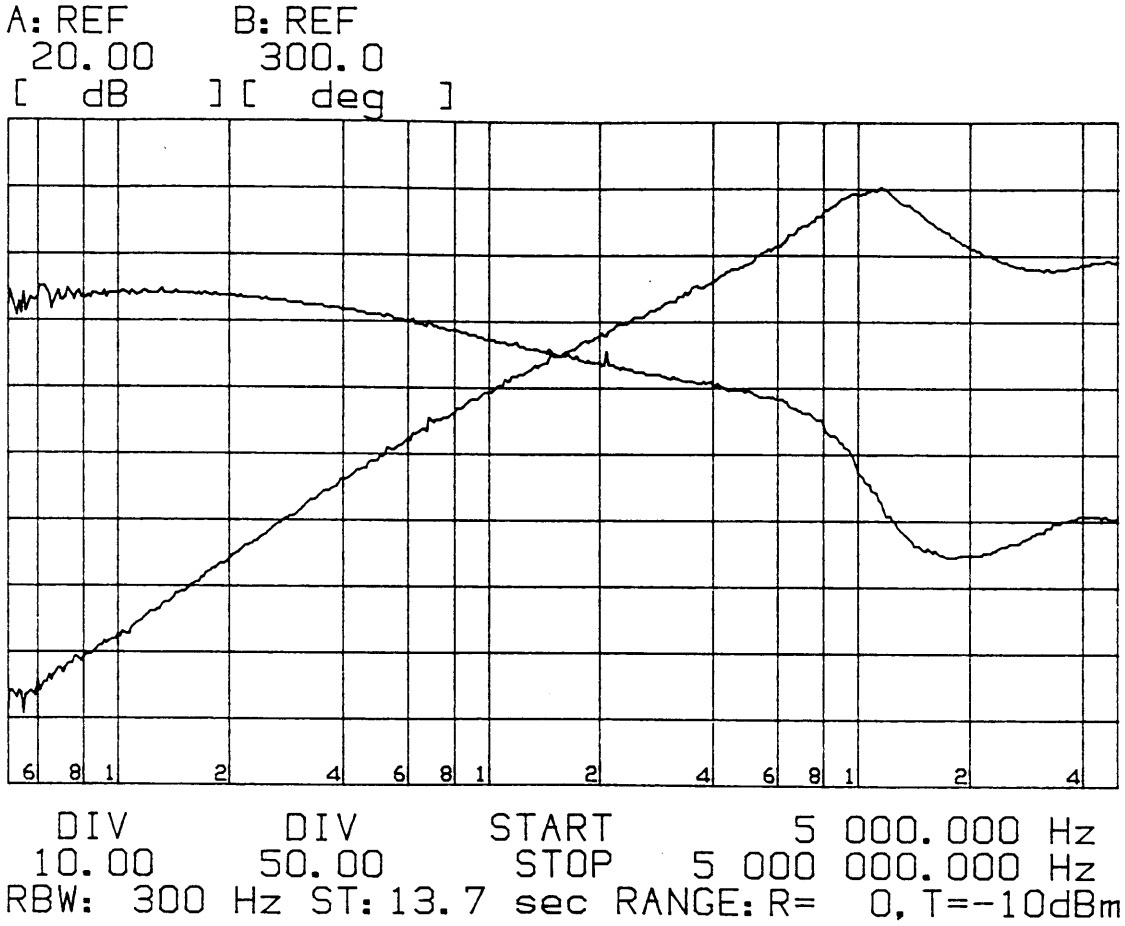

Fig. 2.2 Closed-loop transfer function of the laser frequency stabilization servo from 5 kHz-5 MHz. Curve A is the magnitude and B is the phase.

unstabilized and stabilized cases, as measured by separate Fabry-Perot cavity. The servo loop suppresses the frequency noise by an amount equal to the open loop gain up to the point where the frequency noise has reached the noise limit of the servo system; beyond this point the frequency follows the noise in the loop. For 0.8 ma of photocurrent through the rf-photodiode (about 3 mW of light power), this noise is dominated by the shot noise of the light and, in terms of an equivalent frequency

noise, is at about the $0.4\text{Hz}/\sqrt{\text{Hz}}$ level. Figure 2.3 shows that the stabilized frequency noise has reached this level in the band from 20–40 kHz. Figure 2.3 also shows the

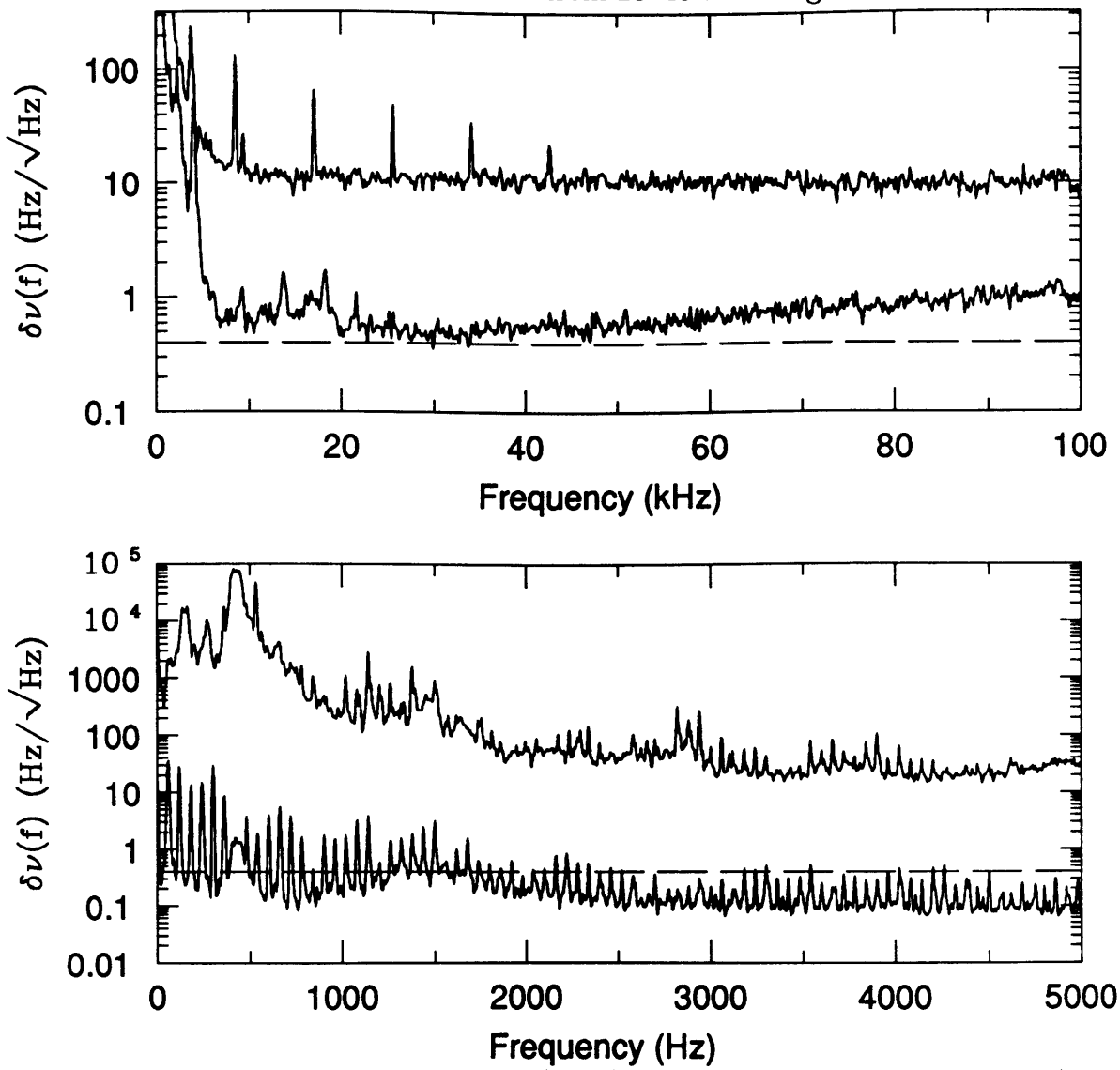

Fig. 2.3 Top: Unstabilized frequency noise (upper) and stabilized frequency noise (lower), as measured by a separate 'measurement' cavity. The data is meaningful above about 5 kHz. Bottom: Unstabilized freq. noise (upper) and stabilized error signal (lower). In both cases, the dashed line is the shot-noise limited level of the frequency stabilization loop.

unstabilized frequency noise and the stabilized error signal of the loop from 0–5 kHz. In most of this band the *error* signal is held below the equivalent shot-noise limited level, indicating that in these regions the difference between the laser frequency and the resonant frequency of the reference cavity is servo-controlled to the $0.4\ \text{Hz}/\sqrt{\text{Hz}}$ level. An accurate measurement of the frequency noise in this region, would require comparison with a separate cavity, for which the effects of acoustic and seismic noise and the shot noise are below this limit. With such a sufficiently stable reference cavity and enough optical power, the frequency noise would just be reduced from the unstabilized level by a factor equal to the open-loop gain in the servo.

2.4 Laser amplitude noise

Laser amplitude noise can appear at the interferometer output through the fringe detection system and through an imbalance in the power in the two arms. The phase modulation-demodulation techniques used to recover the output signal are susceptible to laser amplitude noise at and around the modulation frequency, since signals at frequencies $f_m \pm f$ are mixed down to signals at f. The optical phase is thus modulated at a frequency where the laser is shot-noise limited; for a typical argon laser this is ≥ 5 MHz. When the interferometer is on a dark fringe the demodulated signal is at a null, independent of the light amplitude. Deviations from the null point, however, allow laser power fluctuations in the measurement frequency band to appear as a signal at the output. The demodulated output depends linearly on the arm phase difference for small deviations about the null point, so that the apparent phase fluctuations due to laser power fluctuations are

$$\delta\phi(f) = \frac{\delta P(f)}{P}\,\delta\phi_0\,, \tag{18}$$

where $\delta\phi_0$ is the static offset from zero (modulo 2π) differential arm phase. In fact the average differential arm phase is kept to zero (up to any offsets in the servo electronics which can be made negligible), but the root-mean-square (rms) deviation is non-zero. Since the fluctuations contributing to the rms deviation have a much lower frequency than the signals of interest, it is a reasonable approximation to replace the static offset, $\delta\phi_0$, by the rms deviation, $\delta\phi_{\rm rms}$, in the above formula.

For example, to reach the $\delta\phi_d(f) = 3 \times 10^{-9}\,\mathrm{rad}/\sqrt{\mathrm{Hz}}$ level (the shot-noise due to 100 mW of effective optical power, a few times more than ever used in these experiments) with a fractional power fluctuation of $3\times10^{-6}/\sqrt{\mathrm{Hz}}$ (Fig. 2.4), requires an rms phase deviation of $\delta\phi_{\rm rms} \leq 10^{-3}$rad.

Laser power fluctuations also exert a fluctuating force on the arm mirrors through radiation pressure, which leads, in a free-mass interferometer, to motions of the mirrors. If the power in the two arms is not the same, these forces will be of differing magnitude, resulting in differential arm motions. If the fractional imbalance in the power circulating in the arm cavities ($P_{\rm circ}$) is β, the resulting differential mirror motion is

$$\delta x(f) = \frac{\delta P(f)}{P}\,\frac{2P_{\rm circ}\beta}{mc(2\pi f)^2}\,\frac{1}{\sqrt{1+(4\pi\tau_{\rm st}f)^2}}\,, \tag{19}$$

where m is the mass of a cavity mirror, and the last factor accounts for the filtering effect of the cavity ($\tau_{\rm st}$ is the cavity storage time).

The amplitude noise of the laser is shown in Figure 2.4. The laser is equipped with a rudimentary power stabilization circuit. It compares a small fraction of the emitted light with a reference, and feeds the resulting error signal back to the power supply. The servo reduces the power fluctuations by about a factor of 10 below 100 Hz, and has a unity gain frequency of about 1 kHz. No efforts were made to further

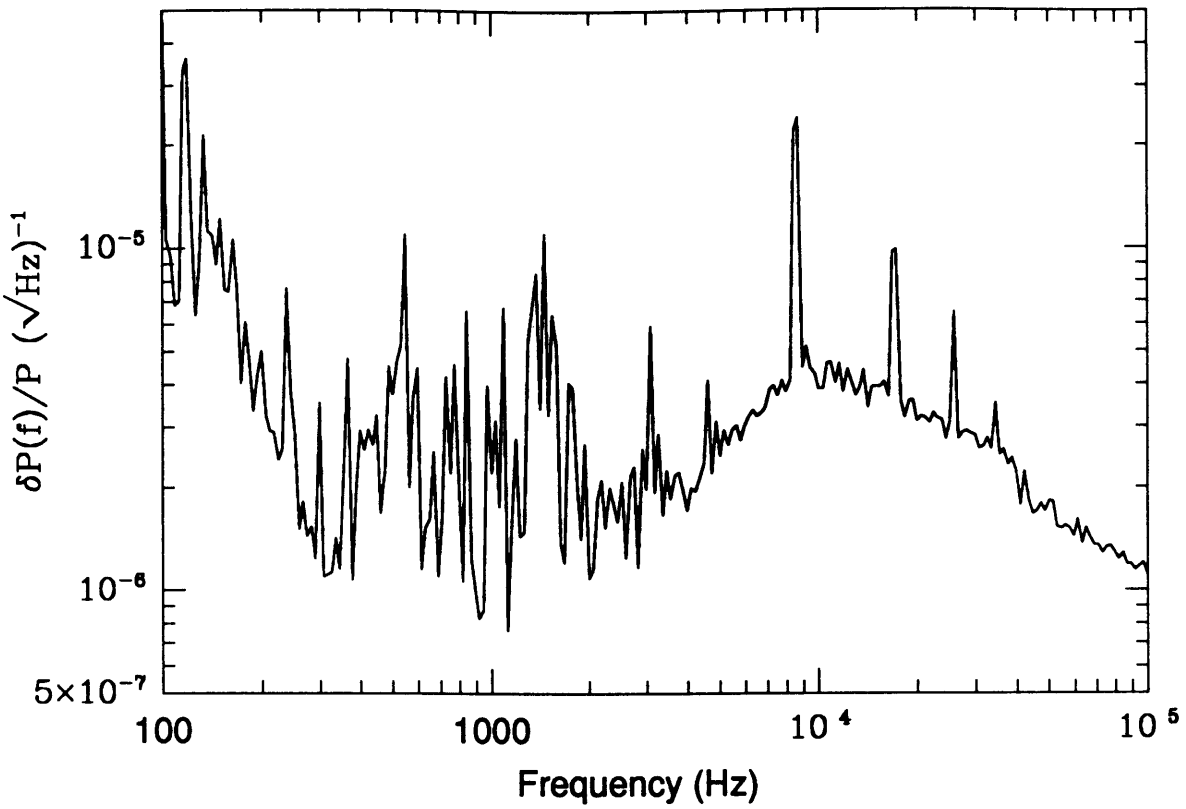

Fig. 2.4. Power fluctuations of the laser. Shot-noise is at the $\delta P(f)/P = 8 \times 10^{-9}$ level. The detected power is $P_{dct} = 20$ mW.

stabilize the laser power for the experiments in this thesis. The fluctuating radiation pressure does not bother fixed mirrors, and it was always possible to operate with a small enough deviation from the dark fringe so that the laser amplitude sensitivity was insignificant.

2.5 Laser beam geometry fluctuations

Spatial asymmetries in the arms leave the output susceptible to beam geometry fluctuations. Possible geometry fluctuations are jitter in the angular or lateral position of the beam, or changes in its mode form. The spatial asymmetry could be due to misalignment, an arm length asymmetry, or differing wavefront distortions in the arms.

Measurements of the beam geometry fluctuations of the laser were not made, but the technique of delivering the laser beam to the interferometer with a single-mode optical fiber, suggested by Weiss, was used. This greatly suppresses the intrinsic beam jitter of the laser. Shoemaker et al. (1986) measured the angular and lateral position noise of the output of such a fiber. The beam directly from the argon laser showed lateral position noise of $\delta s(f) \approx (10^{-4}/f^2)$ m/$\sqrt{\text{Hz}}$ for $f \geq 100$ Hz. After the fiber, an upper limit of $\delta s(f) \leq 10^{-11}$ m/$\sqrt{\text{Hz}}$ for $f \geq 200$ Hz was obtained. The upper limit for the angular position noise was $\delta\alpha(f) \leq 3\times10^{-12}$rad/$\sqrt{\text{Hz}}$. Shoemaker et al. also measured the beam jitter suppression of the other passive approach to

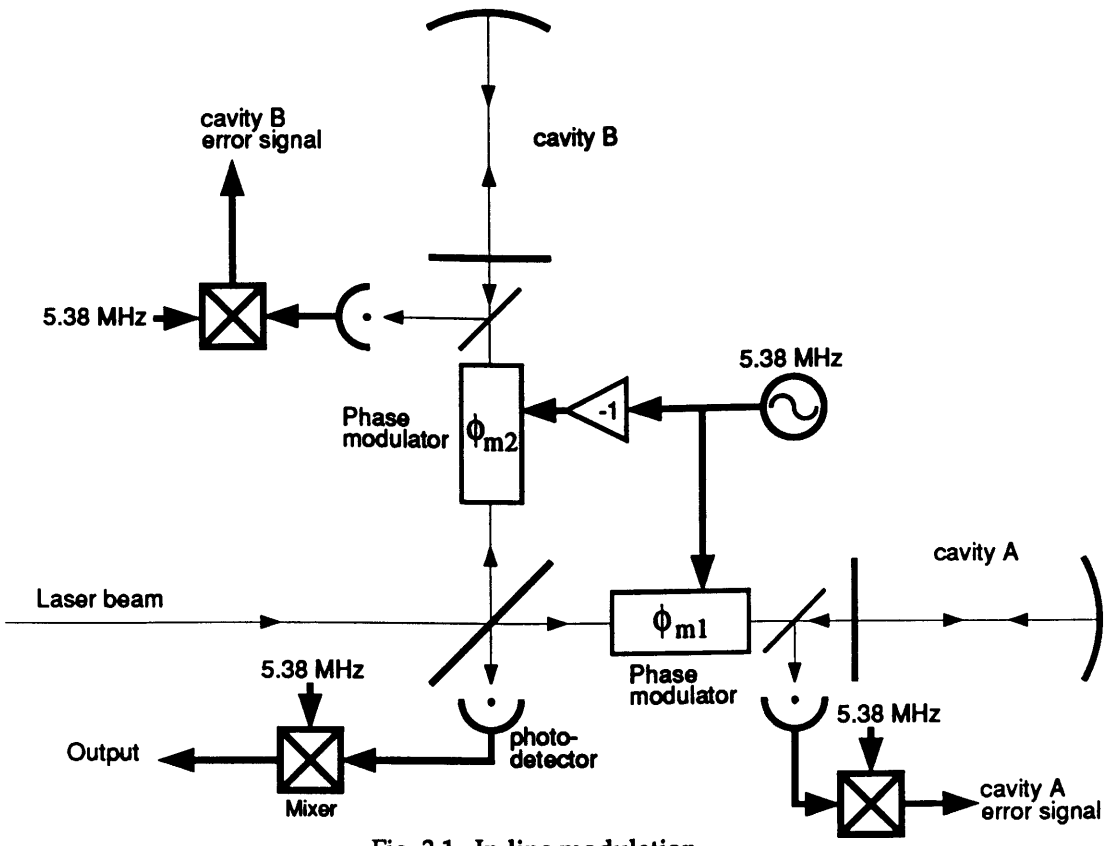

Fig. 3.1 In-line modulation.

improve beam quality: a Fabry-Perot cavity used in transmission (Maischberger et al. 1979 and Rüdiger et al. 1981). The measured lateral fluctuations for this method were 3–10 times higher than the upper limits for the fiber output, but were likely limited by mechanical excitation of the 'mode-cleaning' cavity. In principle, a very high degree of geometry fluctuation suppression can be achieved with a resonant cavity (Rüdiger et al. 1981).

3 In-line modulation

The first experiment on an optically recombined Fabry-Perot arm interferometer employed Pockels cell phase modulators in the arms of the interferometer, between the beamsplitter and the two cavities; this technique has been named 'in-line modulation'. A nearly complete description of the experiment can be found in the paper "Prototype Michelson interferometer with Fabry-Perot cavities", by D. Shoemaker, P.Fritschel, J. Giaime, N. Christensen, and R. Weiss, published in *Applied Optics*, vol. 30, p. 3133. The discussion here is essentially the same as in the paper.

Layout and measured properties. Figure 3.1 shows the relevant optics and signal detection electronics of the experiment. The interferometer is constructed with commercial mirror mounts on small optical tables bolted to the circular bottom plate

of a 1.5 m diam vacuum tank. This bottom plate is isolated from seismic ground motion with rubber-damped springs, giving horizontal and vertical resonances of about 4 Hz. The vacuum tank is closed, but not pumped out, during the experiment. The entire tank is overpressured with filtered air. The cavity mirrors and the space between them are protected by glass tubes filled with very clean (filtered to 0.1 μm particle size with 99.99% efficiency) boil-off from liquid N_2 or with He gas. Sound absorbing material (SONEX 1) inside the tank is used to absorb acoustic noise.

The single-mode fiber which feeds the light into the tank (see section 2.3) is terminated in a mount with a grin lens (not shown); the output of the fiber-grin lens assembly is a nearly collimated beam (see Christensen 1990 for a description of this assembly). This beam is mode matched to the FP cavities with a single positive lens and isolated by two Faraday isolators in series (see Fig. 5.1). The light falls on a disk beamsplitter and is sent (in each arm) through a Pockels cell and into the 47 cm long FP cavity. A fraction (3%) of the reflected light is sent to a photodetector; the rest returns to the beamsplitter where it interferes with the light in the other arm. The light leaving the anti-symmetric output is detected. The light leaving the symmetric port (coincident with the incoming light) is rejected by the Faraday isolator.

The FP cavities have a plano-spherical geometry, with a 1 m radius of curvature rear mirror. The flat input mirror has transmission $T = 2.8\%$, the rear mirror has maximum reflectivity (with approx. 17 ppm transmission), giving a finesse of F=220 and a linewidth of 1.4 MHz. The reflectivity of each cavity on resonance is $R_{\mathrm{cav}} = 97.5\%$. The total mirror losses are inferred to by 160 ppm. See section 5.1 for a further discussion of the mirror properties. The matching of the input beam to the fundamental mode of each cavity is $M = 95\%$. To the precision of our measurements (approx. $\pm 5\%$), there is no difference between the two cavities in terms of matching, finesse, or losses.

The mirror transmissions and losses, and thus cavity finesses, are similar to those to be used in the full scale interferometers. This means that the experiment was not designed to have the optimum position sensitivity but instead was meant to investigate optical characteristics such as contrast and losses, the servos and fringe detection, and the sensitivity and its limits in a regime of interest to a full scale system.

The far mirrors of the FPs can be blocked, leaving a simple Michelson interferometer (MI). The contrast of this interferometer, without Pockels cells in place, is $C = (I_{\mathrm{max}} - I_{\mathrm{max}})/(I_{\mathrm{max}} + I_{\mathrm{max}}) = 0.996$; with the Pockels cells (Gsänger PM-25) in place, the contrast becomes $C = 0.989$. Later experiments which had remote alignment controls (PZT's) on the mirrors showed an even higher contrast, C=0.9995, without Pockels cells, so the earlier *sans* Pockels cells contrast was probably limited by our ability to align the system. With the FP in the arms and locked on resonance, the contrast is $C = 0.986$.

Servo and measurement systems. The rf-reflection technique is used to maintain each arm cavity resonant with the laser light. For this experiment, the laser

frequency is locked to cavity A (rather than to a separate cavity as described in section 2.3), and cavity B is then locked to the stabilized laser light.

The laser frequency servo loop is as described in section 2.3, with an additional Sallen-Key circuit that can be added to the loop to give extra gain in the vicinity of 80 kHz (at the expense of a reduced gain around 40 kHz). With the Sallen-Key circuit, the frequency noise at 80 kHz is held to the shot-noise limit of $0.3\text{Hz}/\sqrt{\text{Hz}}$.

The servo compensation for the cavity B lock is similar to that for the laser, except that the pole-zero pair for the normal operating condition is at 1 Hz and 3 kHz. The actuator for this servo is a PZT on the input coupling mirror of cavity B, which has a pronounced (Q=15) resonance at 24 kHz. To allow a higher unity-gain frequency, a passive anti-resonance circuit in the compensation network is used to cancel this resonance. The unity-frequency is then 4.5 kHz, which is sufficient to make the excursions from the cavity resonance acceptably small.

The Michelson path length difference is also modulated by the Pockels cells in the arms, since they are driven out of phase. However, the level of modulation is significantly reduced by the optical arrangement that has the light passing two times through the modulators. In the first pass, the carrier has two sidebands at $\pm f_{\text{m}}$ put on it (for a modulation index small enough that the higher sidebands can be ignored). This beam is reflected from a cavity. The sidebands are outside the resonance curve of the FP, and thus are shifted by 0 and 2π radians after reflection. The carrier, which is resonant with the cavity, is shifted by π radian upon reflection. The reflected light passes again through the modulator; new sidebands are put on the reflected carrier, which are out of phase with the sidebands that were put on in the first pass through. Thus, there is a cancellation of the modulation.

The quality of the cancellation is a function of several parameters. First, the amount of light absorbed in the cavities: for these cavities, all but 2.5% of the light is reflected. Second, the ratio of the modulation frequency to the cavity linewidth: for the 1.4 MHz linewidth and 5.38 MHz modulation, the reflected sidebands are not at 0° and 360°, but at 13° and (360°−13°). Finally, the distance between the modulator and the cavity input mirror: the transit time causes an additional phase between the original and second sidebands, contributing about 3° of phase delay. When the modulation is small enough that only the first sidebands need be considered, the effect of the double-passing on the signal, expressed as the ratio of the ω_m signal in the double-passed case I^{dp} to the signal for a single pass I^{sp}, is

$$\frac{I^{\text{dp}}(\omega_m)}{I^{\text{sp}}(\omega_m)} = J_0^2(\Gamma)\left\{\left(1-\sqrt{R_{\text{cav}}}\right)^2 + \left[\sin\left(2\omega_m l/c + \phi_{\text{cav}}\right)\right]^2\right\}^{1/2}, \qquad (20)$$

where Γ is the modulation index for a single pass through the modulator, R_{cav} is the intensity reflection coefficient of the cavity on-resonance, l is the distance from the modulator to the cavity, and ϕ_{cav} is the phase shift added to the $\omega_0 \pm \omega_m$ sidebands upon reflection from the cavity. In this case, the amplitude term, $\left(1-\sqrt{R_{\text{cav}}}\right)^2 = (1-.987)^2 = 1.7\times10^{-4}$, is very small, and the signal comes almost entirely from the

phase shift term, $[\sin 16^\circ]^2 = 7.6 \times 10^{-2}$. This gives a signal ratio of $I^{\rm dp}/I^{\rm sp} = 1/3.7$ for a typical Γ of 0.16. The measurements of this reduction compare the ω_m signal of the FP MI and the simple MI. In the simple MI the modulation is nearly doubled on the second pass, so that the signal ratio should be $I^{\rm FPMI}/I^{\rm MI} = 1/7.4$, which is in fair agreement with the directly observed ratio of 1/9. The result of the cancellation is that, in these experiments, the optimum modulation depth cannot be reached; this will be discussed further below. Note that the cavity lock (for which the signal is picked off before the second modulator pass) does not suffer from this cancellation.

However, there is sufficient signal to hold the Michelson to a dark fringe and to make measurements of the signal-to-noise ratio. The demodulated signal from the photodetector at the anti-symmetric output is put through a compensation network similar to those above, with a pole at 160 Hz for initial locking and a pole-zero pair at 1 Hz-3 kHz for normal operation. The filtered signal is amplified with a high-voltage amplifier and sent to one of the Pockels cells. A unity-gain frequency of 5 kHz is attainable and sufficient. The error signal of this loop is analyzed above the unity-gain frequency to obtain the displacement noise spectrum. It is calibrated in displacement using a second PZT mounted on the cavity B input coupling mirror: the signal for a given applied 35 kHz signal can be seen in both the FP MI and the simple MI, where the absolute magnitude can be determined either from the known sensitivity of the Pockels cell or from the calibration-signal size directly compared with the Michelson output fringe amplitude.

Signal sensitivity, noise sources. Figure 3.2 shows the spectrum, expressed as equivalent mirror displacement noise of a single arm mirror, of the interferometer. The photocurrent on the Michelson bright fringe for these measurements is 7.3 ma (about 30 mW of bright fringe power). The top flat curve is the displacement noise of the simple Michelson; note the lack of features at frequencies above 20 kHz. This noise level is at (within 1 or 2 dB of) the shot-noise limit for the measurement. This is determined by replacing the laser light on the anti-symmetric photodetector with an incandescent light source that produces the same photocurrent.

The spectrum for the FP MI is the middle, rapidly falling, curve in Fig. 3.2. At low frequencies ($<$ 30 kHz) acoustic noise is dominant. This noise source determines the servo loop characteristics that are required, as it is against these large fluctuations that the system must be held on-resonance or on the dark fringe. In the 30–100 kHz band, a number of resonances can be seen. These are probably thermally driven resonances in the FP cavity mirror supports and are consistent with masses and resonance Q's in the system. This noise source is the practical limit to the obtainable sensitivity with this interferometer constructed of mirrors in conventional mounts. This measurement is taken with He in the glass tubes protecting the cavity mirrors. With N_2 in the tubes, the resonances of the glass tubes are seen in the spectrum because they produce larger fluctuations in the index of refraction of the intra-cavity gas, due to the higher polarizability of N_2.

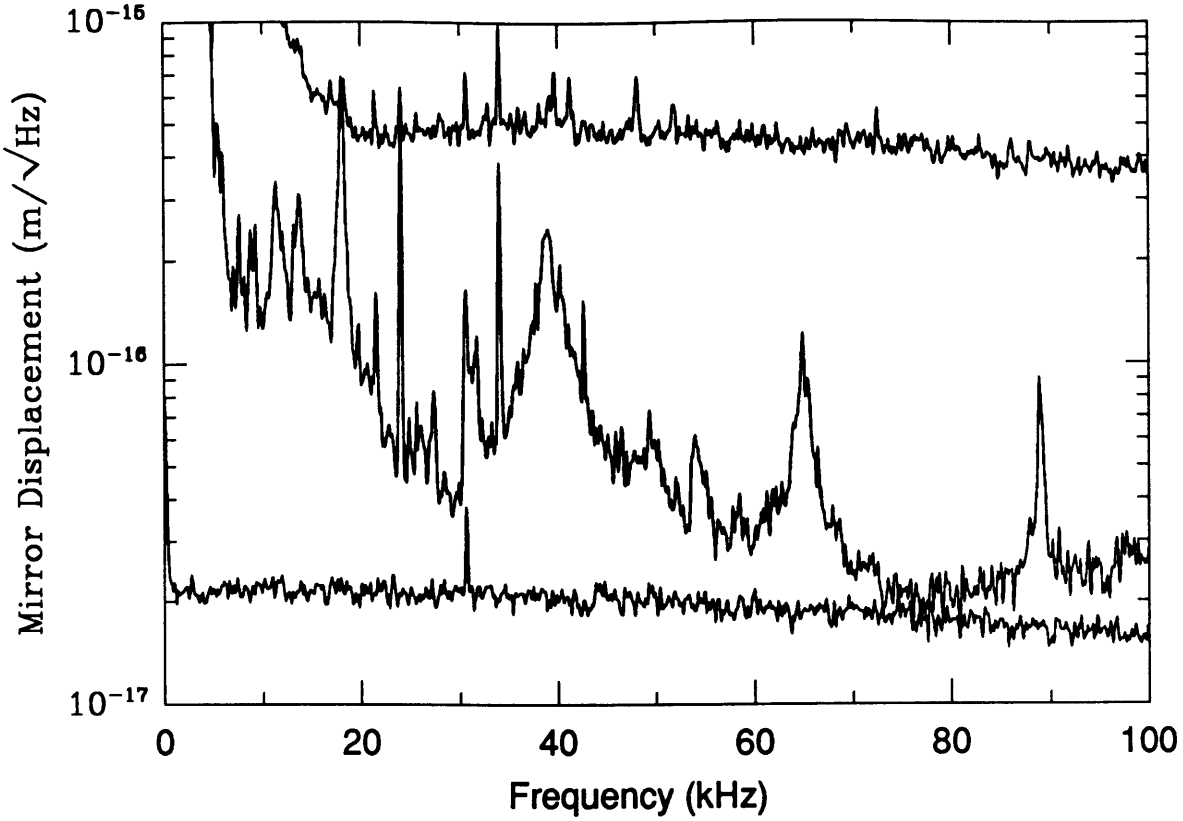

Fig. 3.2 Interferometer spectrum: Top curve, the simple one-bounce Michelson interferometer; middle curve, the Fabry-Perot arm Michelson; bottom curve, the shot-noise for the FP MI measurement.

In a region between 70 and 85 kHz, the spectrum closely approaches the shot-noise limit, as determined by the light bulb test. The light bulb noise is the bottom trace in Fig. 3.2. The equivalent displacement noise due to the shot-noise is $2.05 \times 10^{-17}\,\mathrm{m}/\sqrt{\mathrm{Hz}}$, and the displacement noise for the interferometer at 75 kHz is 1–2 dB higher than this.[1] The increase in sensitivity obtained by adding the cavities is roughly a factor of 25. This is reduced from the ideal factor of $4/T_1 = 143$ because of the reduction in modulation depth.

By impressing a known frequency modulation on the laser, the sensitivity of the FP MI to frequency fluctuations is measured to be $2.5 \times 10^{-17}\,\mathrm{m/Hz}$. This can be interpreted as a difference in storage times of the two cavities of one part in 2000 (eq. 16). The calculated position noise that results, given the frequency noise at 80 kHz of $0.3\,\mathrm{Hz}/\sqrt{\mathrm{Hz}}$, is at a level of $7.5 \times 10^{-18}\,\mathrm{m}/\sqrt{\mathrm{Hz}}$, a factor of nearly 3 below the shot-noise limited position sensitivity.

A thorough calculation of the sensitivity of this instrument that properly takes into account the double passing of the modulator is quite complicated. However, for small modulation, where $J_1(\Gamma)$ is linear with Γ, the double-passing is approximately equivalent to reducing the modulation depth (see also Appendix B for a test of this

[1] This small difference between the light bulb shot-noise and the interferometer noise may be explained by the fact that, because of the internal phase modulation, the light power at the anti-symmetric output of the interferometer varies in time, and the associated shot-noise is non-stationary. The effect of this is discussed by Niebauer et al. (1991).

approximation). The sensitivity of a single-passed FP MI is derived in Appendix B; this formula can be used here if the single-pass modulation index is replaced with the reduced index. For frequencies less than the pole frequency of the arm cavities, the sensitivity to a motion of one cavity mirror is

$$\delta x(f) = \left(\frac{\lambda}{8F}\right)\left(\frac{2e}{I_{\rm max}+I_{\rm min}}\right)^{1/2}\left(\frac{[1-CJ_0(2\Gamma_{\rm net})+2I_{\rm det}/(I_{\rm max}+I_{\rm min})]^{1/2}}{2MJ_0(\Gamma_{\rm net})J_1(\Gamma_{\rm net})}\right). \tag{21}$$

Here $I_{\rm max}$ is the photocurrent on the bright fringe, and $I_{\rm min}$ is the photocurrent on the dark fringe without modulation, both measured at the interferometer output; $I_{\rm dct}$ is the current that would produce a shot-noise equal to the electronic noise contribution of the photodetector.

The first factor in the sensitivity formula is the conversion of mirror displacement to optical phase shift; for these cavities, with a finesse of F=220, this has a value of 2.9×10^{-10} m/rad. The second factor is the equivalent phase noise due to the shot-noise. For this measurement, $I_{\rm max}=7.3$ ma and $I_{\rm min}=0.2$ ma, so the phase noise is $\phi_d(f)=6.6\times10^{-9}\,{\rm rad}/\sqrt{\rm Hz}$. The first two factors together give the ideal shot-noise limited displacement sensitivity, which for this measurement is $1.9\times10^{-18}\,{\rm m}/\sqrt{\rm Hz}$. The third factor takes in account the non-unity contrast and mode-matching, and the electronic noise and has a value of 1 for a perfect system. For the measurement presented, the contrast is $C=.95$, the mode-matching is $M=.95$, $I_{\rm dct}=0.016$ ma, and $\Gamma_{\rm nct}=.036$, which has been reduced by the measured factor of 9. The third factor has a value of 7.2 for these parameters. The calculated shot-noise limited displacement sensitivity is then $1.37\times10^{-17}\,{\rm m}/\sqrt{\rm Hz}$. This is a factor of 1.5 lower than the measured shot-noise sensitivity.

If the detector noise is negligible and the mode-matching is perfect, the third factor in the sensitivity depends only on the contrast and the modulation: $f(C,\Gamma)=[1-CJ_0(2\Gamma)]^{1/2}/J_0(\Gamma)J_1(\Gamma)$. The function $f(C,\Gamma)$ is plotted in Figure 3.3 as a function of Γ for several values of the contrast, C, which shows a mild but important dependence of the optimum sensitivity on the contrast. For the case here of $C=.95$, the optimum modulation index is $\Gamma=0.55$ (much higher than 0.036), for which $f(C,\Gamma)/M=1.2$ (rather than 7.2).

The shot-noise limited displacement sensitivity for the simple MI is also derived in Appendix B. For a motion of one arm mirror, this is

$$\delta x(f) = \left(\frac{\lambda}{4\pi}\right)\left(\frac{2e}{I_{\rm max}+I_{\rm min}}\right)^{1/2}\left(\frac{[1-CJ_0(2\Gamma)+2I_{\rm det}/(I_{\rm max}+I_{\rm min})]^{1/2}}{CJ_1(2\Gamma)}\right). \tag{22}$$

For the measurement shown in Fig. 3.2, $I_{\rm max}=7.3$ ma, $I_{\rm min}=.073$ ma, $C=0.98$, $\Gamma=0.32$, and $I_{\rm dct}=.016$ ma, giving a calculated sensitivity of $3.16\times10^{-16}\,{\rm m}/\sqrt{\rm Hz}$. This is a factor of 1.5 lower than the measured sensitivity of $4.8\times10^{-16}\,{\rm m}/\sqrt{\rm Hz}$ (Fig. 3.2 top curve). The measured shot-noise limited sensitivity for both the FP MI and the MI is a factor of 1.5 higher than the calculated sensitivity. A possible resolution

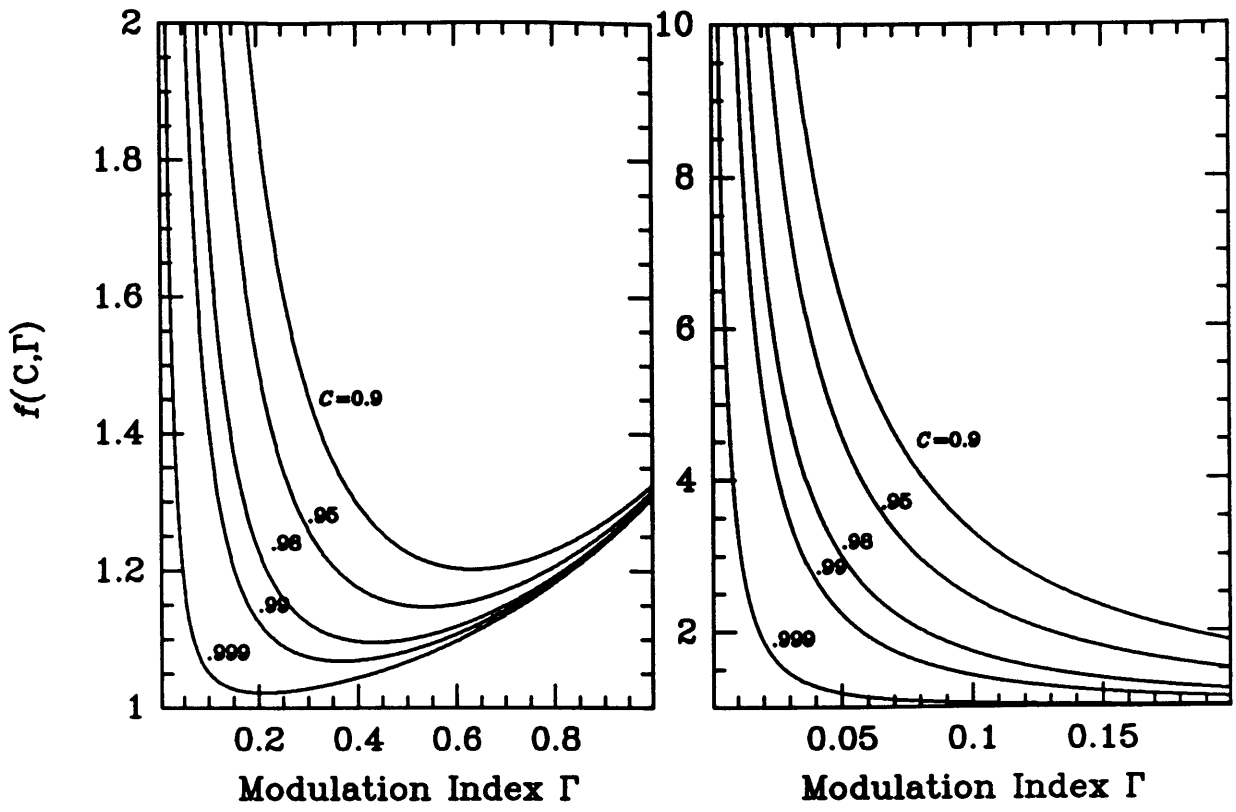

Fig. 3.3 The function $f(C,\Gamma)$ vs. Γ for five values of the contrast, C. The left graph shows the minimum of f and the optimum Γ for each C, while the right graph shows the effects on f of a less-than-optimum Γ.

of the discrepancy is that the calibration of the spectrum of Fig. 3.2 is off by this factor (i.e. the calibration-PZT motion is off by a factor of 1.5).

Scaling and limitations. The in-line Pockels cells (PCs), though they provide a differential phase modulation with a minimum of optical complexity, present the major limitation to scaling this configuration. The limitations come mainly from wavefront distortions produced by a non-uniform index of refraction across a cell, and the exacerbation of this problem as the optical power is increased. Differing wavefront distortions in the two arms, in addition to leaving the output sensitive to beam geometry fluctuations as mentioned above, limit the overlap between the two beams, and thus limit the contrast of the interferometer. If we take the fractional power coming out of the beamsplitter in the best case, C=0.989 and $I_{\rm min}/I_{\rm max} = 5.5 \times 10^{-3}$, as being entirely the result of wavefront distortions from the Pockels cells, this corresponds to an average wavefront error due to the PCs of $\phi \approx 2\sqrt{I_{\rm min}/I_{\rm max}} = 0.15$ radian, or approximately $\lambda/40$. These Pockels cells are Gsänger PM-25's, made of ADP.

A contrast degradation such as this affects the sensitivity of the interferometer in two ways. The shot-noise limited sensitivity gets poorer as the contrast is reduced as shown in Fig. 3.3. In addition, a contrast degradation will limit the power build-up

in a recycled interferometer. Recycling, discussed in the next chapter, is a technique for increasing the power in an interferometer. The degree to which the power is increased (the recycling gain) is limited by the optical losses in the interferometer. In this case, the contrast defect due to the Pockels cells corresponds to a loss of 5.5 $\times$ 10^{-3} of the input power.

Another problem is that these Pockels cells do not appear to be capable of passing high light power with impunity to the spatial quality of the beam. We did not observe any limitations with the 35 mW of light power available to us, but Maischberger et al. (1987) report problems with powers much greater than this. They studied a simple one-bounce Michelson interferometer with ADP Pockels cells (also Gsänger PM-25's) in the arms, and employed recycling to increase the light power. They saw near shot-noise limited performance for a circulating power of P = 550 mW, but the noise level did not reduce with a further increase in the power. They attributed this phenomenon to contrast degradation due to increased wavefront distortion in the Pockels cells. Though the threshold for damage to the crystal itself is much higher than this (Gsänger specifies the maximum optical power to be 100 W), the important criteria here is the level at which the sensitivity of the interferometer is limited, and this appears to be not much more than 0.5 W. These results are for the particular crystal ADP, and it is quite possible that some other nonlinear crystal might be able to pass more power with minimal beam distortion. The crystal Mg:$LiNbO_3$ is a possible candidate, and the question deserves more research.

In a full scale interferometer the beam is 5–10 cm in diameter, and since phase modulating crystals of a sufficient size are not available (the PM-25s have a 5 mm square aperture), beam reducing/expanding telescopes would be needed in the arms. The complexity of such a system is not attractive.

This in-line experiment suffered greatly from the modulation cancellation effect. In a larger system, however, this effect can be countered by making the distance between the modulator and the cavity long enough so that the rf-frequency accrues a phase shift of π upon propagating from the modulator to the cavity and back to the modulator. That is, we require $2k_{rf}l = \pi$ or equivalently $l = \lambda_{rf}/4$, where l is the distance from the modulator to the cavity in each arm. In this case, if there is no additional phase shift on the sidebands from the cavity, the modulation will be enhanced rather than cancelled. For example, if the modulation frequency is 10 MHz, λ_{rf} =30 m and we require l =7.5 m. Or, a combination of propagation and cavity phase shifts could be used to attain a total phase shift of something close to π. In short, the modulation cancellation effect is not a fundamental problem for in-line modulation.

4 Recycling: theory

4.1 Simple theory of recycling

The basic optical arrangement of broadband recycling is shown in Figure 4.1. The average power at the anti-symmetric output of the Michelson interferometer is

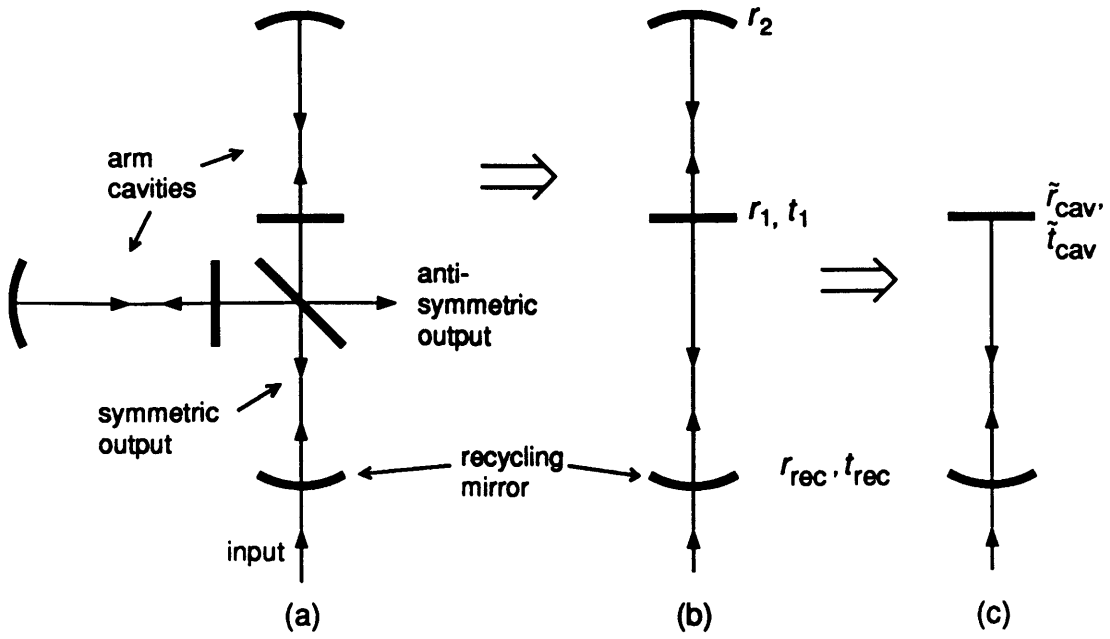

Fig. 4.1. (a) The optical elements of a recycled Michelson interferometer with Fabry-Perot cavities in the arms. (b) When the interferometer is operating at the dark fringe of the anti-symmetric output, the two arms and beamsplitter are modeled by one arm cavity, creating a three-mirror cavity. (c) The arm cavity is then modeled by a single mirror, having reflection and transmission coefficients of a Fabry-Perot cavity.

equal to

$$P_{\text{anti}} = \frac{1}{2} P_0 \left(1 - C \cos\left(\overline{\phi}_d\right)\right), \tag{23}$$

where $\overline{\phi}_d$ is the average phase difference between the two arms, and $P_0 = P_{\max} + P_{\min}$, where $P_{\max}$ is the output power on the bright fringe $(\overline{\phi}_d = \pi)$ and $P_{\min}$ the output power on the dark fringe $(\overline{\phi}_d = 0)$. The contrast is $C = (P_{\max} - P_{\min})/(P_{\max} + P_{\min})$. The interferometer is operated about the point $\overline{\phi}_d = 0$, *i.e.*, the dark fringe. The fluctuating phase difference, $\phi_d(f)$, can be measured either by differentially phase modulating the light in the two arms and then demodulating the output signal (in-line modulation), or by interfering the output field with a phase modulated reference field ('external modulation', see chapter 6). In a well balanced interferometer, dark fringe operation implies that nearly all the light (to the extent that power is not lost due to imperfect optics) exits through the symmetric output and travels back towards the light source. From the standpoint of the input laser beam the interferometer looks like a mirror of reflectivity somewhat less than unity due to losses in the optics and an imperfect contrast. The power circulating in the interferometer can be increased by making an optical cavity with a 'recycling' mirror at the input of the interferometer as the cavity input mirror and with the interferometer forming the rear mirror (Fig. 4.1b, c).

The ratio of the internal power to the input power for a simple two mirror Fabry-Perot cavity on resonance is

$$P_{\rm int}/P_0 = \frac{T_1}{\left(1-\sqrt{R_1R_2}\right)^2} = \frac{T_1}{\left(1-\sqrt{(1-A_1-T_1)(1-A_2)}\right)^2}\,, \qquad (24)$$

where T_i, R_i, and A_i are the power transmission, reflection, and loss coefficients respectively of the input mirror ($i=1$) or the rear mirror ($i=2$). Any transmission of the rear mirror is included in the loss A_2, so that $1-R_2 = A_2$. Applied to a recycled interferometer, T_1 is the transmission of the recycling mirror, R_2 is the reflectivity and A_2 the loss of the interferometer operating on the dark fringe. The ratio $P_{\rm int}/P_0$ is dubbed the recycling gain, $G_{\rm rcc}$. For a given R_2 and input mirror loss A_1, the ratio $P_{\rm int}/P_0$ is a maximum for

$$T_1 = (1-A_1)(1-R_2(1-A_1))\,. \qquad (25)$$

With this simple Fabry-Perot model for recycling, the maximum increase in the interferometer circulating power is then

$$G_{\rm rec}^{\rm max} = P_{\rm int}^{\rm max}/P_0 = \frac{1}{A_2 + A_1/(1-A_1)} \approx \frac{1}{A_2+A_1}\,. \qquad (26)$$

The basic result is that the maximum recycling gain is equal to 1/(total loss).

Broadband recycling thus gives an increase in the output signal by a factor of $G_{\rm rcc}$ and a corresponding reduction of the equivalent phase noise by a factor of $\sqrt{G_{\rm rec}}$. The signal, proportional to the phase difference between the arms, exits directly through the anti-symmetric output and thus is not recycled and experiences only a single arm storage time. This means that the frequency response of the output signal to a phase difference in the arms is not affected by standard recycling: the signal-to-noise ratio is increased by a factor of $\sqrt{G_{\rm rec}}$ without changing the bandwidth of the interferometer, thus the name broadband recycling. A complete discussion of the frequency response of this and other interferometer configurations is given by Meers (1989).

A further point is worth noting. For the case of a single mirror or a delay line in each arm, the interferometer, as viewed from the symmetric side of the beamsplitter, does indeed look like a simple mirror and can be (conceptually) replaced, in the limit of perfect contrast, with a mirror of amplitude reflection coefficient $r_{\rm equiv} = (r_{\rm arm})^b$, where $r_{\rm arm}$ is the amplitude reflection coefficient of an arm mirror and b is the number of bounces in an arm. For the configuration with cavities in the arms, however, the interferometer must be replaced with a 'mirror' having the more complicated amplitude reflection coefficient of a Fabry-Perot cavity. The model for the recycled interferometer is now a three mirror cavity (Fig. 4.1b). This leads to some interesting mode coupling phenomena which are discussed in the following sections.

4.2 Length scaling

As a technique for increasing the position sensitivity of an interferometer in the practically accessible gravity wave band (100 Hz $< f <$ a few kilohertz), broadband recycling only makes sense on a large-scale (several kilometer arm lengths) interferometer. The reasoning is as follows: In order to optimize the position sensitivity, the light should be stored in each arm for a time comparable to half the period of the lowest frequency gravity wave, f_0, the interferometer is designed to detect. For prototype-scale interferometers (arm lengths tens of meters or less), this requirement leads to a very large number ($\geq 10^4$) of equivalent bounces in the arms. For a Fabry-Perot of length l, input mirror intensity transmission T_1 and total mirror loss A, this translates into choosing the cavity energy storage time, $\tau_{st} \approx 2l/c\,(T_1 + A)$ to be $\tau_{st} = 1/4\pi f_0 \approx 1$ msec. This can be achieved by making the arm input mirror transmission very low, but then, given the loss in current state-of-the-art mirrors (10–100 ppm), a majority of the light would be lost (absorbed or scattered) in the arms. In this case broadband recycling cannot give a significant increase in power. In a full-scale interferometer (arm lengths of a few kilometers), however, the equivalent number of bounces required is much less (on the order of 30) and the fractional power lost in the arms is a few percent or less. In this case, a power gain of around 30 is realistic. For fixed mirror losses, the power lost in a cavity is inversely proportional to the input mirror transmission, and so the recycling gain in an optimally designed interferometer scales with the arm length, $L_{\rm arm}$. Thus the increase in position sensitivity possible with broadband recycling scales as $\sqrt{L_{\rm arm}}$.

Note also that for a given strain-to-optical phase shift conversion, the arm cavity finesse, and thus the power build-up in the arm cavities, is inversely proportional to the arm length. If there is a restrictive limit on the optical power incident on the mirrors, this is another argument for a long arm length.

4.3 Field expressions

This section starts a more detailed treatment of a recycled Fabry-Perot arm interferometer. Expressions for the electric fields at various points in the interferometer are given. A somewhat simplified optical arrangement is shown in Figure 4.2. The simplifications made are that the beamsplitter is assumed to be 50–50, and the two arm cavities have the same mirror properties and nominal length (though not the same interferometric length). The transmission coefficient $t_{\rm p}$ can be used to account for any other common loss in the recycling cavity, such as from an extra beamsplitter-plate or loss in the Michelson beamsplitter.

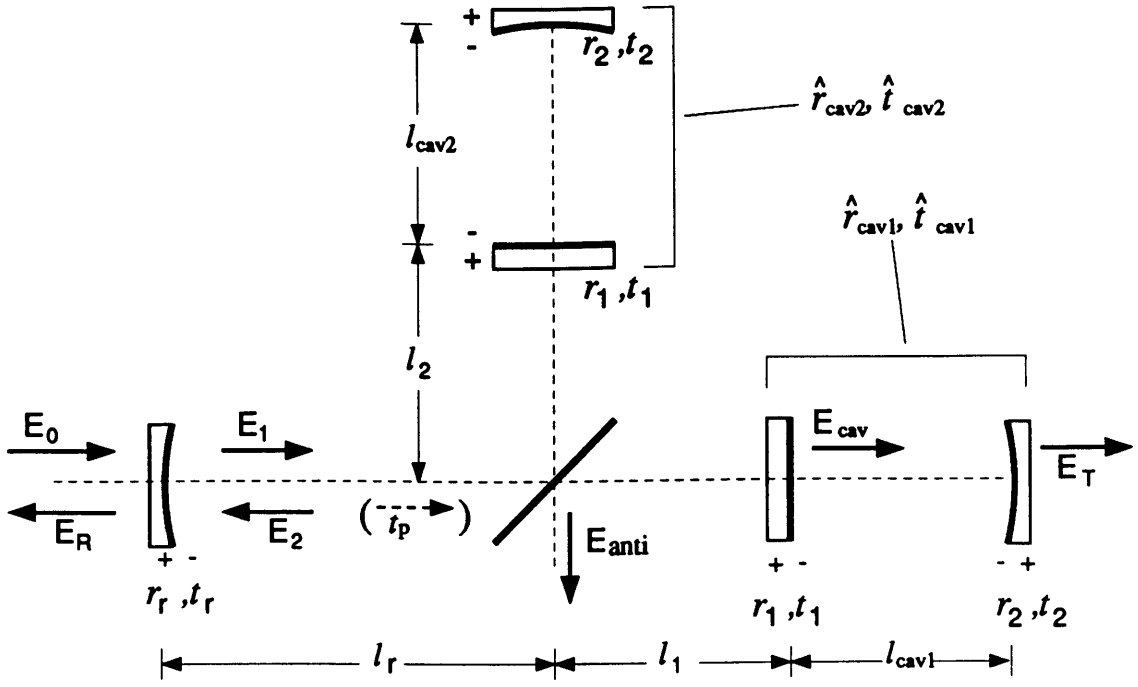

Fig. 4.2 Definitions for calculation of the electric fields. The ˆ above $\hat{r}_{cav}$ and $\hat{t}_{cav}$ indicates that these are complex quantities. The +/- signs for the mirrors indicate the sign convention for reflection from the denoted side of the mirror. (The r's and t's are all positive.)

The following further definitions are made:

$$\begin{aligned} \hat{r}_{cav1} &= r_c(\theta_1)e^{i\phi_1(\theta_1)} \equiv r_{c1}e^{i(\phi_c+\phi_d)} \\ \hat{r}_{cav2} &= r_c(\theta_2)e^{i\phi_2(\theta_2)} \equiv r_{c2}e^{i(\phi_c-\phi_d)} , \end{aligned} \tag{27}$$

and

$$l_1 \equiv l_c + l_d , \quad l_2 \equiv l_c - l_d . \tag{28}$$

That is, the phase shifts from the cavities and the beamsplitter-cavity distances are explicitly broken up into common and differential parts. The independent parameter $\theta_i = 2\omega l_{cavi}/c$, is a dimensionless expression for the optical frequency deviation from the cavity resonance, where ω is the optical frequency in radians per second, l_{cavi} is the length of cavity i, and c is the speed of light.

In terms of this parameter and the individual mirror coefficients as defined in Fig. 4.2, the amplitude reflection and transmission coefficients of a Fabry-Perot cavity are (Appendix A):

$$\hat{r}_{cav} = \frac{r_1 - r_2(r_1^2 + t_1^2)e^{i\theta}}{1 - r_1 r_2 e^{i\theta}} , \quad \hat{t}_{cav} = \frac{t_1 t_2 e^{i\theta/2}}{1 - r_1 r_2 e^{i\theta}} . \tag{29}$$

The fields at the recycling mirror can be computed by use of a transfer function method. Let T_{ij} be the transfer function of field E_i to field E_j; that is, T_{12} is the ratio E_2/E_1. Then recycling cavity internal field is:

$$E_1 = t_r E_0 - r_r E_2 = t_r E_0 - r_r T_{12} E_1 ,$$
$$\frac{E_1}{E_0} = \frac{t_r}{1 + r_r T_{12}} . \tag{30}$$

The reflected field is:

$$E_R = r_r E_0 + t_r E_2 = r_r E_0 + t_r^2 (T_{12}/(1 + r_r T_{12})) E_0 ,$$
$$\frac{E_R}{E_0} = \frac{r_r + (r_r^2 + t_r^2) T_{12}}{1 + r_r T_{12}} . \tag{31}$$

The transfer function T_{12} is:

$$T_{12} = \frac{1}{2} t_p^2 e^{2ik(l_r + l_c)} e^{i\phi_c} \left[r_{c1} e^{2ikl_d} e^{i\phi_d} + r_{c2} e^{-2ikl_d} e^{-i\phi_d} \right] . \tag{32}$$

The contrast is one in this model. (Note for a two mirror cavity, the transfer function is simply $T_{12} = -r_2 e^{i\theta}$, yielding the expression for $\hat{r}_{cav}$ above.) In the case where the cavities are operating anti-symmetrically about resonance, $\phi_c = \pi$ and $r_{c1} = r_{c2} = r_c$, the transfer function is:

$$T_{12} = -r_c t_p^2 e^{2ik(l_r + l_c)} \cos(2kl_d + \phi_d) . \tag{33}$$

The recycling cavity internal field is a maximum when the field reflected from the recycling mirror is a minimum, i.e. zero. Defining the power loss of the recycling mirror as A_r, the condition $E_R = 0$ occurs for:

$$r_r + (1 - A_r) T_{12} = 0 . \tag{34}$$

This requires $2k(l_r + l_c) = 0 \bmod 2\pi$. Taking ϕ_d to be a small fluctuating phase, so that $\cos(\phi_d) \approx 1$, and imposing the dark fringe condition $2kl_d = 0 \bmod 2\pi$ leads to the choice

$$r_r = (1 - A_r) r_c t_p^2 . \tag{35}$$

The internal field is then:

$$\frac{E_1}{E_0} = \left(\frac{1 - A_r}{1 - (1 - A_r) r_c^2 t_p^4} \right)^{1/2} = \sqrt{G_{rec}} . \tag{36}$$

The field at the anti-symmetric output, with respect to the internal field E_1, is

$$\frac{E_{anti}}{E_1} = \frac{1}{2} t_p e^{ik(l_r + 2l_c)} e^{i\phi_c} \left[r_{c1} e^{2ikl_d} e^{i\phi_d} - r_{c2} e^{-2ikl_d} e^{-i\phi_d} \right] . \tag{37}$$

With the cavities operating about resonance and the output at the dark fringe, this becomes

$$\frac{E_{anti}}{E_1} = -i r_c t_p e^{ik(l_r + 2l_c)} \sin \phi_d . \tag{38}$$

With respect to the input field, the output field is of course $E_{anti}/E_0 = (E_{anti}/E_1)\sqrt{G_{rec}}$.

4.4 Mode structure of recycled interferometer

If there is no differential phase between the two arms ($2kl_d + \phi_d = 0 \bmod 2\pi$), the beamsplitter and the two cavities can be conceptually replaced by a single cavity, to form a three mirror cavity. It is worthwhile to examine the mode structure of this simplified optical arrangement (Fig. 4.1b).

Expressed in terms of the individual mirror properties, the expression for the field inside the recycling cavity for this three mirror arrangement becomes (setting $t_p = 1$):

$$\frac{E_1}{E_0} = \frac{t_r(1 - r_1 r_2 e^{i\theta_1})}{1 - r_1 r_2 e^{i\theta_1} + r_r(r_1 - r_2(r_1^2 + t_1^2)\, e^{i\theta_1})\, e^{i\theta_2}} , \tag{39}$$

where $\theta_1 = 2\omega l_{cav}/c$ and $\theta_2 = 2\omega l_r/c$. The double resonance condition of recycling corresponds to $\theta_1 = 2n\pi$ and $\theta_2 = 2m\pi$. The linewidth of the combined cavity, $\Delta\nu_{rcc}$, is defined as the full-width-at-half-maximum of the recycling cavity internal power curve as a function of the optical frequency. Some manipulation of the above expression gives, when the loss is dominated by the arm cavity and the optimum recycling mirror has been chosen (T_1 = loss),

$$\Delta\nu_{rec} \approx \Delta\nu_{cav}(1 - R_{cav})/2 , \tag{40}$$

where $\Delta\nu_{cav}$ is the linewidth (FWHM) of the isolated arm cavity and $R_{cav} = r_c(0)^2$ is the power reflection coefficient of the arm cavity on resonance. Since for a low-loss system, R_{cav} is near one, this is a much narrower linewidth than that of an arm cavity.

The resonance condition in the recycling cavity is determined by requiring the round trip phase to be an integral number of 2π radians. The round trip phase consists of propagation phase and arm cavity reflection phase: $2kl_r + \phi_{cav} = n2\pi$, for resonance in the recycling cavity. At the double resonance condition, corresponding to an optical frequency ν_0, the cavity reflection phase is $\phi_{cav} = \pi$. If the fsr of the recycling cavity is smaller than the fsr of the arm cavity ($l_r > l_c$), the next resonance of the recycling cavity occurs when $\phi_{cav} \approx 0$ rad, i.e. the light is not resonant in the arm cavity. The nest resonance of the recycling cavity thus occurs at a frequency $\nu \approx \nu_0 \pm c/4l_r$.

The mode structure of such a three mirror cavity is shown is Figure 4.3. The cavity lengths are those of the coupled cavity experiment described in section 5.2: $l_r = 5.0$ m; $l_{cav} = 0.48$ m. The mirror parameters also correspond to those in that experiment: $T_r = .28$; $A_r = .01$; $T_1 = .028$; $A_1 = A_2 = 3\times10^{-4}$; $T_2 = 0$; ${T_p}^2 = .91$.

For a full-scale interferometer, the arm cavity length will be much greater than the recycling cavity length, producing a quite different mode structure. Consider the parameters of a long baseline interferometer: $l_{cav} = 4.01$ km; $l_r = 10$ m; $T_r = .027$; $T_1 = .03$; $A_r = A_1 = A_2 = 10^{-4}$. The recycling gain, given no other losses than those listed, is theoretically $G_{rcc} = 37$. The bandwidth of an isolated arm cavity is $c/2lF = 185$ Hz, and with a recycling gain of 37 the combined cavity linewidth will

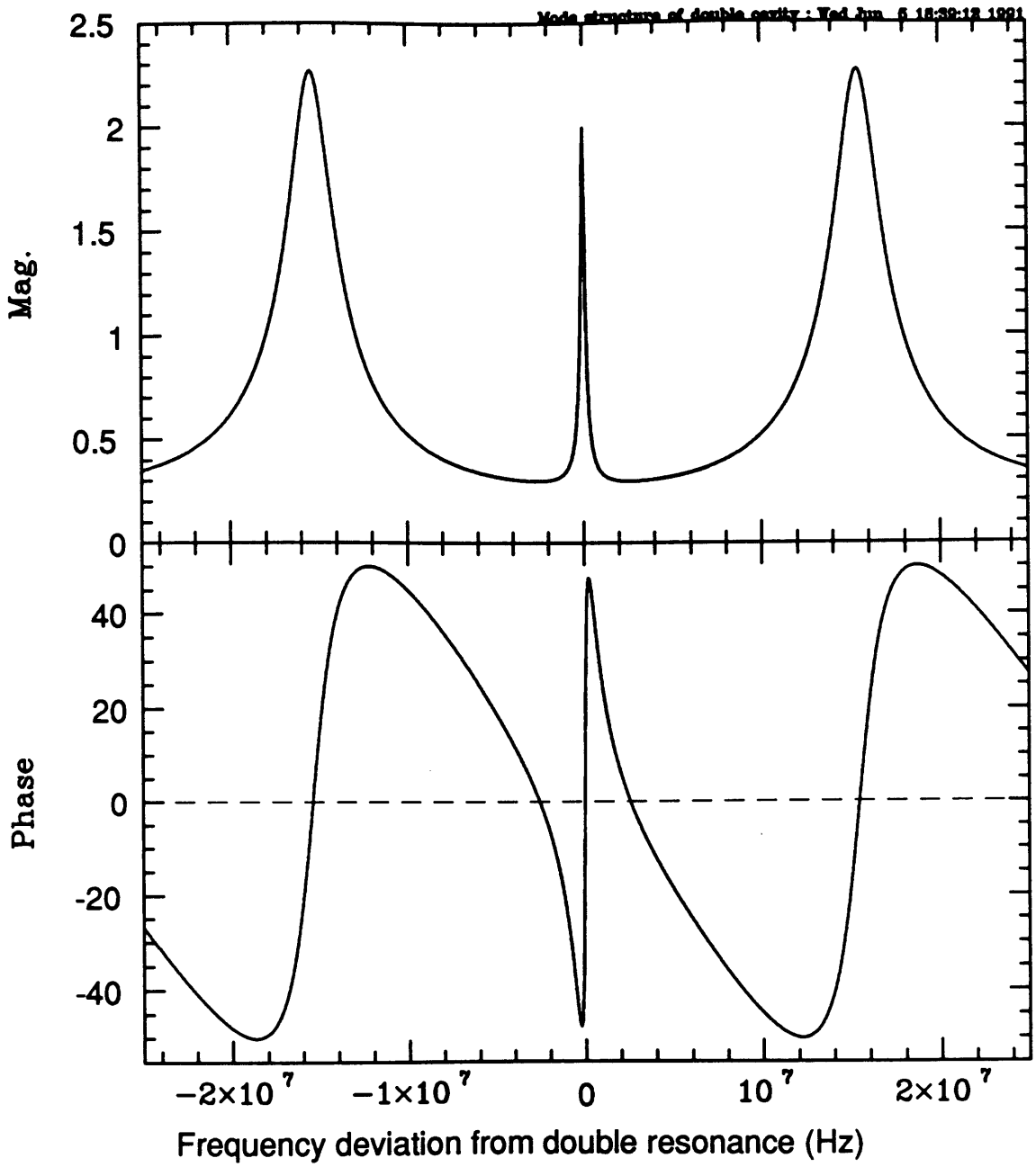

Fig. 4.3. Mode structure of a three mirror cavity. Plotted is the field in the recycling cavity (eq. 39), for the cavity parameters of the experiment in chapter 5.2. The full width at the 3 dB points of the central peak is 200 kHz.

be $\Delta\nu_{\rm rec} \approx 2.5$ Hz. The free-spectral-range of the arm cavity is 37.5 kHz. In the vicinity of the double resonance, the mode structure will be as in Figure 4.4, where the recycling cavity internal power is plotted.

The next resonance of the recycling cavity will appear at a frequency shift of $c/4l_r = \pm 7.5$ MHz from the double resonance. This next resonance is complicated by the resonances of the arm cavities, which appear every 37.5 kHz, as shown in Figure 4.5 where the amplitude and phase of the recycling cavity internal field is

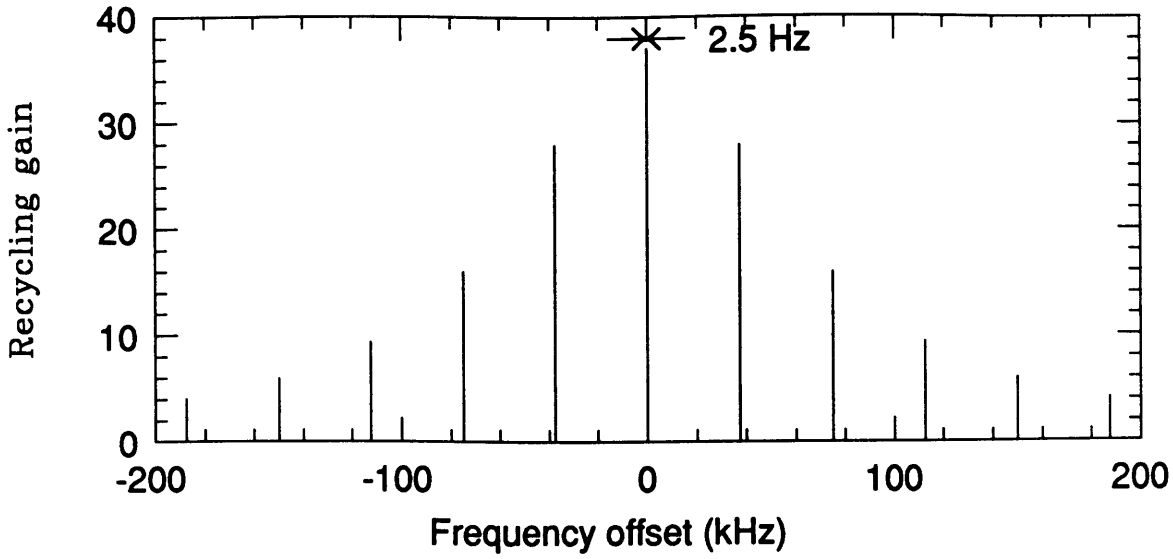

Fig. 4.4 Recycling cavity internal power around the double resonance for a long baseline interferometer. The free-spectral-range of the arm cavity is 37.5 kHz. The interferometer parameters are given in the text.

plotted. The arm cavity length has been tuned ($l_{\rm cav} = 4.01$ km) so that the center of the recycling cavity resonance falls halfway between two arm cavity resonances.

5 Recycling: experiments

5.1 Choice of arm mirror parameters

In order to have any chance of achieving a significant recycling power gain, the loss in the arm cavities must be small. This requires that the transmission of the cavity input mirrors must be much greater than the mirror loss. For these experiments, the cavity finesse is chosen to be as high as possible within this limitation of keeping the cavity losses low. In the limit where the input transmission is much greater than the mirror loss, the on-resonance power reflection coefficient for a Fabry-Perot cavity is

$$R_{\rm cav} = 1 - \frac{4(A_1 + A_2 + T_2)}{T_1}. \tag{41}$$

The mirror losses $(A_1 + A_2 + T_2)$ are in effect multiplied by the factor $(4/T_1)$.

The mirrors in these experiments are made from Corning grade 0A glass, 'superpolished' by Optics Technology to an rms surface roughness < 1 Å. The dielectric coatings are ion-beam sputtered by PMS. The per mirror loss of ~ 100 ppm available at the time of coating (December 1989) drove the choice of $T_1 = 2.8\%$. These parameters would give a cavity loss of $1 - R_{\rm cav} \approx 3\%$. (This does not include the loss due to reflections from the (anti-reflection coated) first surface of the cavity input mirror.) This is about what we observe for fresh mirrors, but they tend to get more lossy with exposure to the atmosphere.

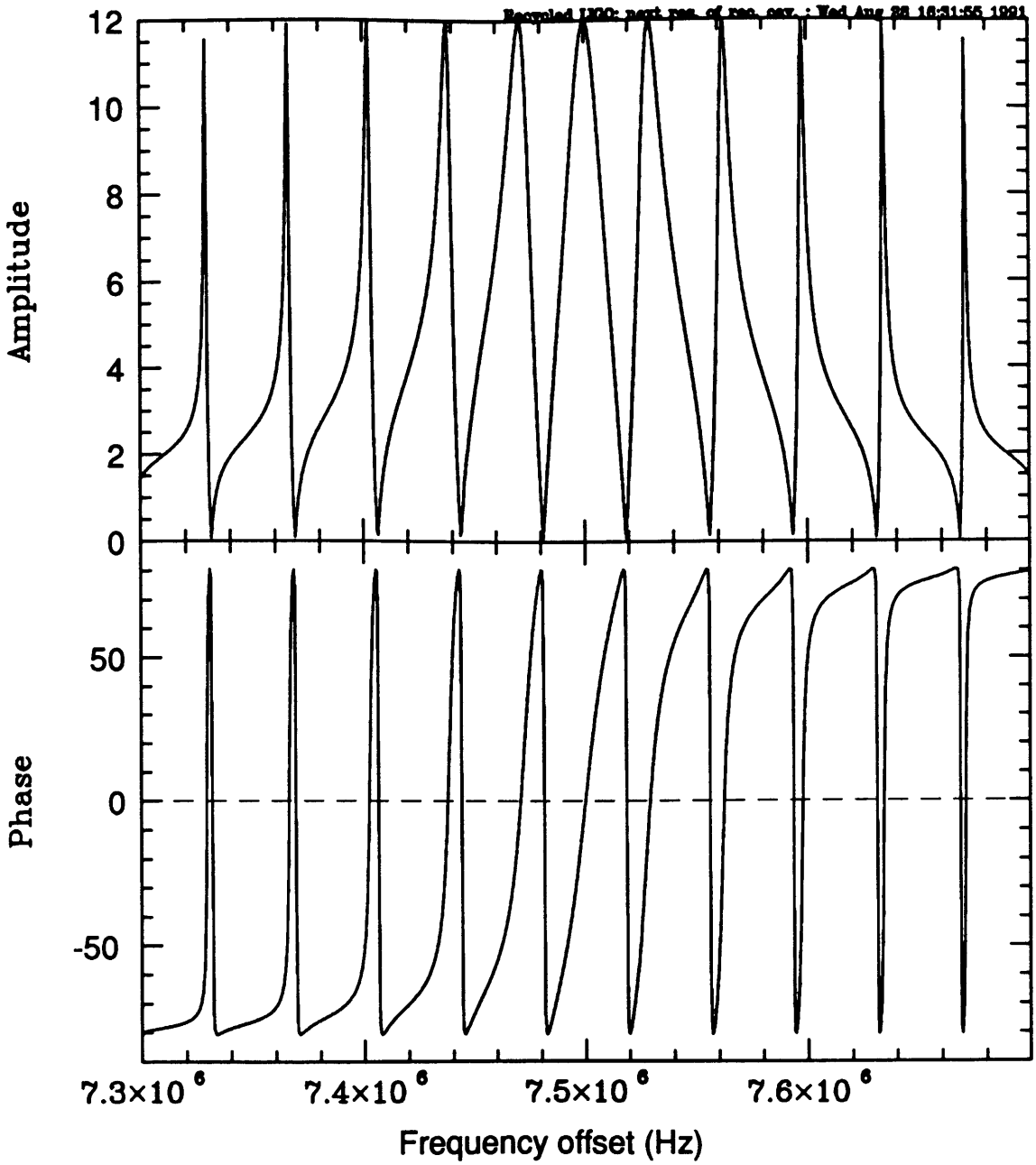

Fig. 4.5 Recycling cavity internal field around the first next resonance of the recycling cavity for a long baseline interferometer. The center of the resonance occurs at an offset of 7.5 MHz from the double resonance. The interferometer parameters are given in the text.

5.2 Coupled cavities: 5 m recycling cavity

Purpose. The first recycling experiment performed was the recycling of a single cavity: this is the three-mirror or coupled cavity as described above. Such an experiment allows us to look with this simpler geometry at questions that are in common with a complete Fabry-Perot arm interferometer, such as mode matching and coupling, sensitivity to misalignment, and understanding the power gain realized.

Another issue is the generation of an error signal for holding the arm cavity on resonance. The standard phase modulation/reflection lock method is clearly affected by the mode structure shown in Figure 4.3. In order for a significant amount of the modulation sidebands to enter the recycling cavity, the modulation frequency must be chosen to be $f_m \approx \pm(c/4l_r)(2n+1)$. In order to test this idea of modulating at the next free-spectral-range, the recycling cavity length must be long enough to bring the modulation frequency down to a reasonable value. We chose $l_r \approx 5$ m, so that $c/4l_r \approx 15$ MHz.

Experimental setup. The optical and servo system is depicted in Figure 5.1. The 4.84 m recycling cavity length (defined as the path length from the recycling

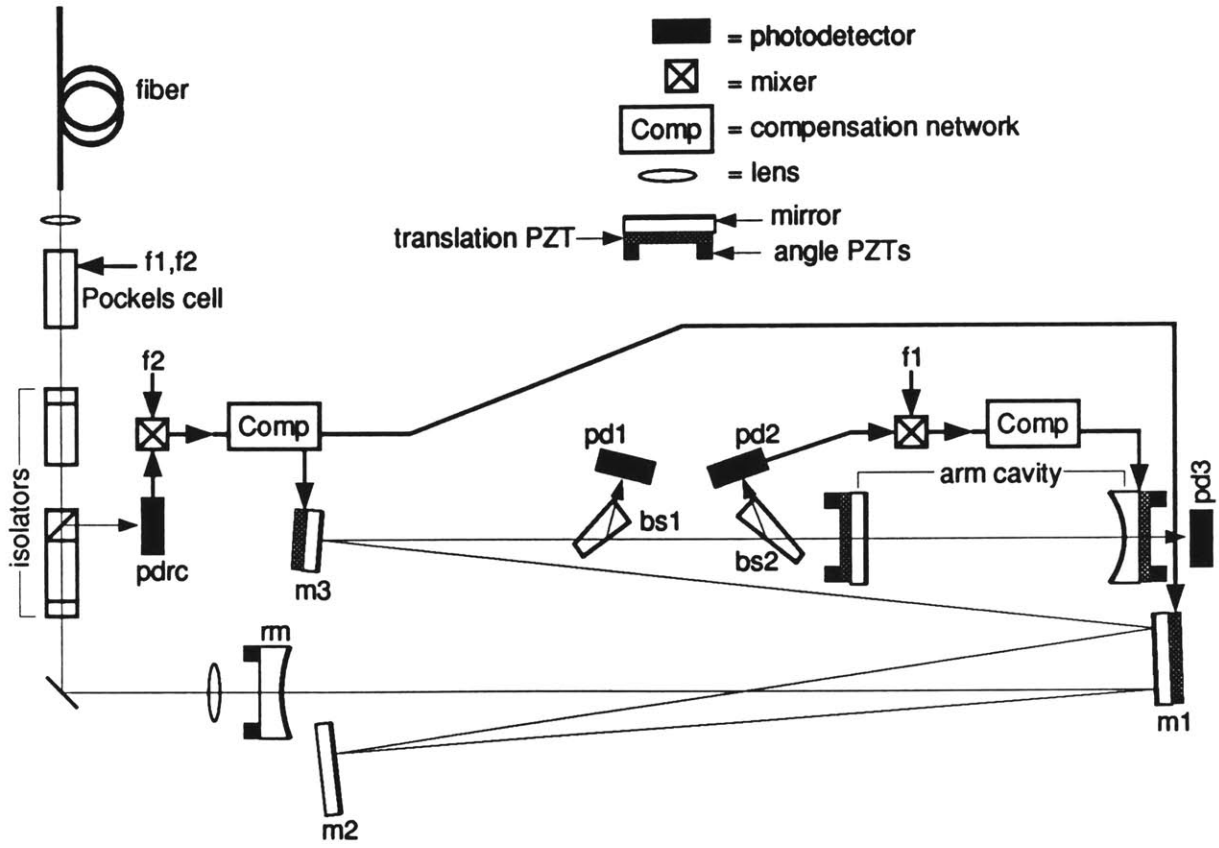

Fig. 5.1. Setup for coupled cavity experiment.

mirror to the arm cavity input mirror) is achieved by multiple traversals of a ~ 1 m diameter table. The arm cavity is 47 cm long and formed of a flat $T = 2.8\%$ input mirror and a concave 1 m radius of curvature high reflectivity rear mirror, both $1''$ diam. The beam size at the arm input flat (the waist) is $\omega_0 = 0.286$ mm. At a distance 4.95 m from this point, the beam has a radius $\omega = 2.88$ mm and a phase front radius of curvature of R = 5 m. The spatial modes in the individual cavities can then be matched by using a concave R = 5 m recycling mirror placed 4.95 m

from the arm input mirror. We found that the best matching occurred at a distance of 4.84 m, indicating a 2% error in the recycling mirror curvature. A series of three lenses matches the output of the fiber-grin assembly to this coupled cavity mode.

The arm cavity mirrors and the recycling mirror (**rm**) are equipped with PZTs that provide about 3 mrad of remote alignment control in each of the two pertinent angular degrees-of-freedom. The translation PZTs each provide about 1 μm of movement. The arm mirror translation PZTs are each made of two 1″ o.d./0.5″ i.d. PZT washers, with resonant frequency $\sim$ 30 kHz. The PZT on mirror **m3** is a small disc ($f_0 \sim 200$ kHz) of the type used on the laser high reflector (2.2). Mirror **m1** is mounted on a Burleigh PZ-80 ($f_0 \sim 4$ kHz).

The beamsplitter **bs1** is a 5 degree wedge, mounted so that one face is at Brewster's angle, presenting negligible reflection loss. Photodetector **pd1** measures the beam reflected from **bs1** (0.8% of the incident power is reflected); this gives a measure of the power inside the recycling cavity and/or the power incident on the arm cavity. Beamsplitter **bs2** is a 3 degree wedge, again with one face at Brewster's angle. It directs 0.5% of the light reflected from the arm cavity onto the photodetector **pd2**, an rf-photodetector of the type described in chapter 2.2, tuned for f_1 = 15 MHz. (A more economical arrangement would be to use one beamsplitter plate and detect the beams reflected in opposite directions. The two splitter arrangement used anticipated the requirements of a recycled (two arm) interferometer, where it was thought that a splitter in each arm and a splitter between the recycling mirror and the main beamsplitter would be needed. This particular design was not actually implemented. A disadvantage of using wedges is that they expand the beam in one direction.) The light reflected from the recycling cavity is measured with **pdrc**, an rf-photodetector tuned for f_2 = 5.38 MHz.

Generation of error signals. Error signals for the arm cavity and recycling cavity lengths are generated with the rf phase-modulation/demodulation technique. In general, the signal at the modulation frequency f_m is proportional to $J_0(m)J_1(m)\sin\phi$, where ϕ is the difference between the carrier phase and the average phase of the two sidebands at $f_0 \pm f_m$ (Appendix A). For small deviations from ϕ=0, the sensitivity of the rf signal to a length or frequency change is then proportional to $J_0(m)J_1(m)\,d\phi/d\theta$, where $d\theta = 2\omega dl/c + 2ld\omega/c$.

The arm cavity error signal is derived from the light reflected from the arm cavity and works as follows: Consider a deviation from resonance of the isolated arm cavity. This produces a change in the carrier phase, Φ, of $(d\Phi_{cav}/d\theta_c)_{\theta_c=0} \approx 4/T_1$ (for $A << T_1$), where $\theta_c = 2\omega l_c/c$ and T_1 is the transmission of the input mirror. If the sidebands are sufficiently outside the bandwidth of the cavity, their phase is not changed, $d\Phi^{sb}/d\theta_c \approx 0$.

In the coupled cavity configuration, the carrier phase shift is increased because of the additional storage in the recycling cavity. In general for a two mirror cavity, if $d\theta_c$ is the (incremental) round trip phase shift in a cavity operating about resonance ($\theta_c = \theta_0 + d\theta_c$, $\theta_0 = n2\pi$), the phase shift of the cavity internal field, Φ_{int}, is related

by $d\Phi_{\rm int}/d\theta_{\rm c} = \sqrt{R_1 R_2}/(1-\sqrt{R_1 R_2})$. For the coupled cavities, the phase shift of the recycling cavity internal carrier due to an arm cavity length change is then

$$\left(\frac{d\Phi_{\rm cav}}{d\theta_{\rm c}}\right)\left(\frac{d\Phi_{\rm int}}{d\Phi_{\rm cav}}\right) \approx \frac{4}{T_1}\,\frac{\sqrt{R_{\rm r}R_{\rm c}}}{1-\sqrt{R_{\rm r}R_{\rm c}}}\,. \tag{42}$$

If the sidebands are sufficiently outside the arm cavity resonance, their phase is still not significantly changed, $d\Phi^{\rm sb}_{\rm int}/d\theta_{\rm c} \approx 0$. In this case, $d\phi = d\Phi_{\rm int}$. Additional losses in the recycling cavity can be included by multiplying $R_{\rm r}R_{\rm c}$ by an effective reflectivity $R_{\rm eff} \approx 1 - A$, where A is the round trip loss due to these additional elements.

Ideally the arm cavity error signal would be sensitive only to fluctuations in the arm cavity length. In fact the signal at $f_{\rm m} = f_1$ derived from the recycling cavity internal field is also sensitive to the recycling cavity length, though to a lesser degree. The carrier phase shift due to a recycling cavity length change, $d\theta_{\rm r} = 2\omega\, dl_{\rm r}/c$, is as given above: $d\Phi_{\rm int}/d\theta_{\rm r} = \sqrt{R_{\rm r}R_{\rm c}}/(1-\sqrt{R_{\rm r}R_{\rm c}})$. The phase of the sidebands is also sensitive to the recycling cavity length, since they are also resonant in the recycling cavity. The sidebands are not resonant in the arm cavity, though, so the factor $R_{\rm c}$ must be replaced with unity, so that: $d\Phi^{\rm sb}_{\rm int}/d\theta_{\rm r} = \sqrt{R_{\rm r}}/(1-\sqrt{R_{\rm r}})$. The signal at $f_{\rm m}$ due to a change in the recycling cavity length is then proportional to

$$\frac{d\phi}{d\theta_r} = \left(\frac{d\Phi^{\rm sb}_{\rm int} - d\Phi_{\rm int}}{d\theta_{\rm r}}\right) = \frac{\sqrt{R_{\rm r}}\,(1-\sqrt{R_{\rm c}})}{(1-\sqrt{R_{\rm r}})\,(1-\sqrt{R_{\rm r}R_{\rm c}})}\,. \tag{43}$$

It is time to put some numbers into these equations. The transmission of the recycling mirror is $T_{\rm r} = 28\%$, and the estimated loss is $A_{\rm r} = 1\%$, so $R_{\rm r} = 0.71$. The on-resonance reflectivity of the arm cavity is $R_{\rm c} = 0.92$. There is an additional 8% loss in the recycling cavity (see below), giving $R_{\rm cff} = 0.92$. The transmission of the arm cavity input mirror is $T_1 = 2.8\%$. The sensitivity to the arm cavity length is thus

$$\frac{d\phi}{d\theta_c} = \left(\frac{d\Phi_{\rm cav}}{d\theta_{\rm c}}\right)\left(\frac{d\Phi_{\rm int}}{d\Phi_{\rm cav}}\right) \approx \frac{4}{T_1}\,\frac{\sqrt{R_{\rm r}R_{\rm c}R_{\rm eff}}}{1-\sqrt{R_{\rm r}R_{\rm c}R_{\rm eff}}} = (143)(3.44) \approx 490\,. \tag{44}$$

The sensitivity to the recycling cavity length is

$$\frac{d\phi}{d\theta_r} = \left(\frac{d\Phi^{\rm sb}_{\rm int} - d\Phi_{\rm int}}{d\theta_{\rm r}}\right) = \frac{\sqrt{R_{\rm r}R_{\rm eff}}\,(1-\sqrt{R_{\rm c}})}{(1-\sqrt{R_{\rm r}R_{\rm eff}})\,(1-\sqrt{R_{\rm r}R_{\rm eff}R_{\rm c}})} \approx 0.8\,. \tag{45}$$

Thus the signal detected by **pd2** at $f_{\rm m}$=f_1 is about 600 times more sensitive to an arm cavity mirror motion than to an equivalent recycling cavity mirror motion.

Consider next the field reflected from the recycling cavity. The sensitivity of the signal at f_1 is again relatively small because both the carrier and the sidebands at $f_0 \pm f_1$ are resonant in the recycling cavity. The input beam can also be phase modulated at a frequency f_2, such that the resulting sidebands are not resonant in the recycling cavity. The phase of these sidebands is then not dependent on the recycling or arm

cavity length, and the full phase shift on the carrier will be detected by **pdrc** at f_2. The carrier phase shift depends on both the arm cavity and the recycling cavity lengths and is more sensitive to the arm cavity length by the factor of 140 above. But if the arm cavity is held on resonance (with the signal from **pd2**), fixing Φ_{cav}, the signal from **pdrc** at f_2 then depends primarily on the recycling cavity length (compromised by residual deviations of the arm cavity due to finite servo gain) and thus can be used to control this length.

Servo loops. The important requirement of the two servos (arm cavity and recycling cavity) is that they hold the cavities close enough to resonance that the variations in the power coupled into the cavities is negligible. (Negligible in this case means that the fluctuations do not compromise the measurements of the dc optical power stored in the cavities, something like $\delta P/P < 0.01$.) Given the ambient excitation of the mirrors, this requirement is easy to achieve with simple servo loops. The loop compensation for both servos is a simple pole, typically at 10–100 Hz, for the initial locking. Once locked, a pole/zero combination typically at 1Hz/1kHz is added to give more low frequency gain. The unity gain frequency of the arm cavity loop is 3–5 kHz, limited by the PZT resonance. Though it is not actually measured, the unity gain frequency of the recycling cavity lock can be higher than this because the mirror **m3** PZT resonance is much higher. For the recycling cavity loop, the signal is integrated further and applied to the slow PZT on mirror **m1** for more low frequency gain.

Losses and recycling gain. The recycling gain for this system is defined as the ratio of the power measured by **pd1** when both cavities are resonant to the power (in the fundamental mode) measured by **pd1** when the recycling mirror **rm**, and the other recycling cavity optics, is absent. This factor should be the same as the increase in the power transmitted by the (resonant) arm cavity for these two cases. The recycling mirror is not actually removed but rather is merely misaligned sufficiently so that there is no interference in the recycling cavity. The required misalignment is small enough that the alignment of the arm cavity to the incoming beam is not significantly affected. The signal detected by **pd1** when **rm** is misaligned is corrected for the transmission of **rm** ($T_r = 0.28$) and the other optics preceding **bs1** ($T_{othcr} = 0.95$), and also for the imperfect mode-matching of the input beam to the recycling cavity ($M = 0.9$), to obtain a measure of the power incident on the system.

The (corrected) measured increase in the power on **pd1** is a factor of 5.18. The power transmitted through the arm cavity (measured with **pd3**) also increases by this factor, but in this case no correction for mode-matching is necessary since only the TEM_{00} component is measured even in the non-recycled configuration. In order to relate the measured power increase to the expected increase, the system is modeled as a two mirror Fabry-Perot with the recycling mirror as the input mirror and the losses in the rest of the system lumped into the loss of the rear mirror. The ratio of

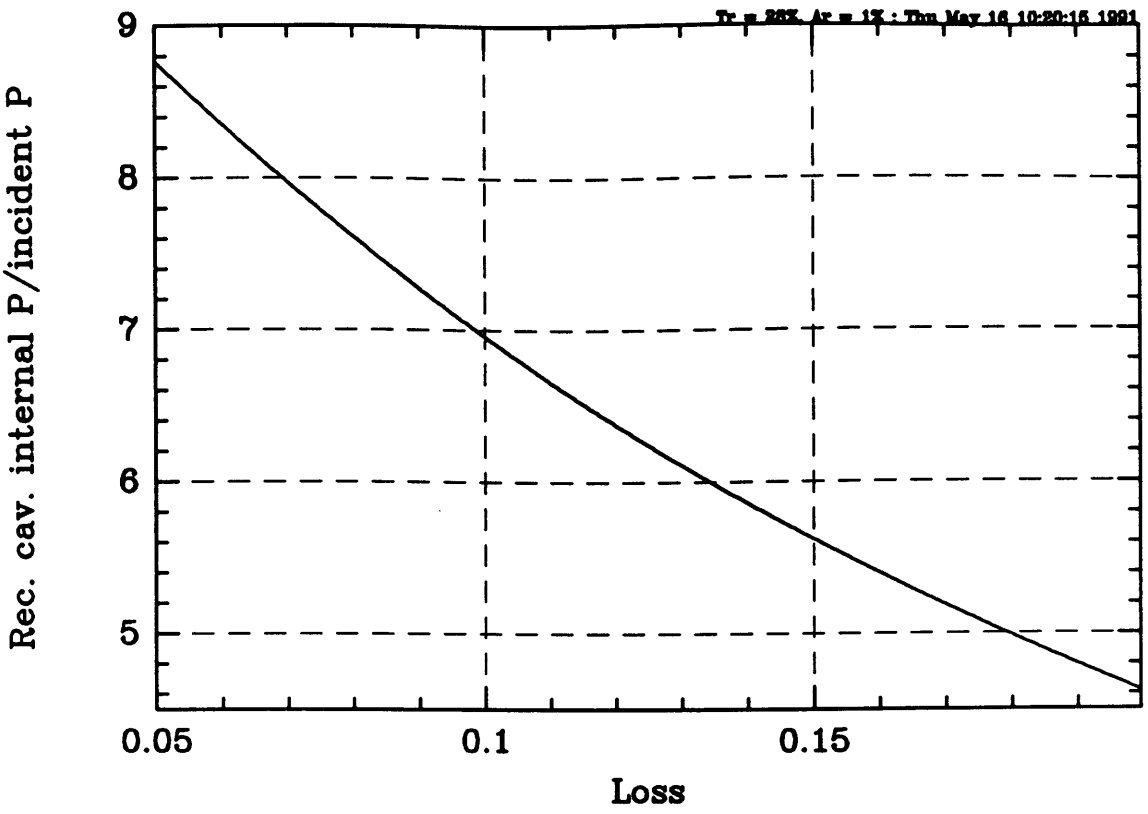

Fig. 5.2. Recycling gain model, eq. 46, plotted as a function of the rear mirror loss (corresponding to the arm cavity plus intra-recycling cavity (t_p) loss), for a recycling mirror transmission and loss of T_r=28% and A_r=1%.

the internal power to the incident power for such a two mirror cavity is

$$\frac{P_{\rm int}}{P_0} = \frac{T_r}{\left(1-\sqrt{(1-A_r-T_r)(1-A_2)}\right)^2}, \tag{46}$$

where any transmission of the rear mirror is included into the loss, A_2. For T_r = 28% and A_r = 1% (an estimate of the loss), this expression is plotted in Figure 5.2.

The measured gain of 5.18 implies a loss of A_2 = 17%. The loss on reflection from the resonant arm cavity is measured to be 8%, corresponding to a per mirror loss of 3×10^{-4}. The recycling cavity internal power gain can also be measured with the arm cavity off-resonance (but aligned), in which case the reflection coefficient is essentially one. In this case, the measured power gain is 7.24. Fig. 5.2 shows a gain of 7.24 for a loss of A_2 = 9%, consistent with the fact that the loss is known to be 8% less than the resonant arm case. The round trip losses of the components in the recycling cavity are (measured and estimated):

- arm cav. input mirror AR surface (est.): 1%
- **bs1** (meas.): 1.6%
- **bs2** (meas.): 1%
- **m1** & **m2** (est.): 0.1%

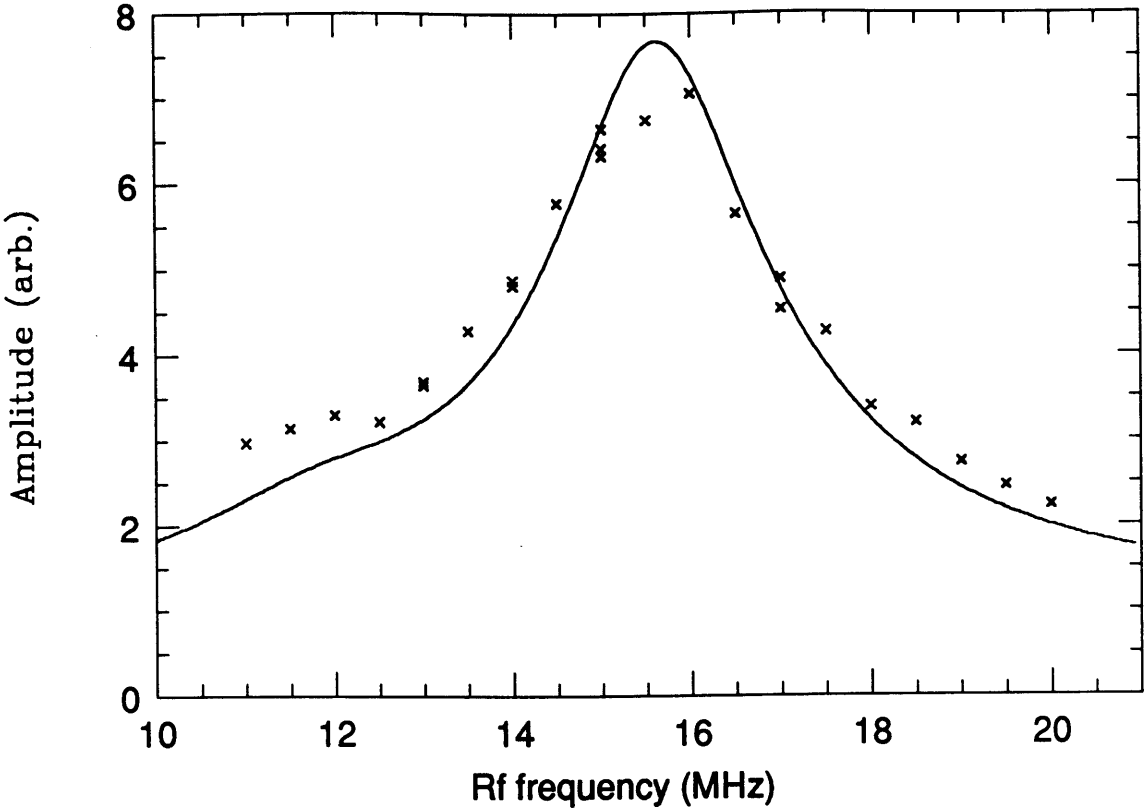

Fig. 5.3 Sensitivity of the error signal (at **pd2**) to the rf frequency. Also shown (smooth curve) is the lineshape of the recycling cavity.

- **m3** (est.): 1%
- Total: 4.7%

The estimated total loss is less than 9%. The mirrors **m1** and **m2** are low-loss mirrors with a nominal loss of $A = 10^{-4}$; it is quite likely that after prolonged exposure to the atmosphere the loss per reflection is much higher than this. Since there are six such reflections in one round trip, it is likely that the loss for **m1** and **m2** is much higher than 0.1%. Mirror **m3** is an ordinary laser-grade mirror, and the two-reflection loss could be higher than 1%.

Since this experiment was intended mainly as an investigation of the error signal generation and servo loop scheme, no further effort was made to explain all the implied loss.

Sensitivity to the modulation frequency. Because of the resonant build-up of the rf-sidebands in the recycling cavity, the signal produced at **pd2** by an arm cavity motion depends on the modulation frequency. This sensitivity is mapped out by varying the modulation frequency and measuring, with **pd2**, the signal produced by an 80 kHz modulation of the arm cavity length (created by applying an 80 kHz signal to the end mirror/PZT of the arm cavity). This measurement is shown in Figure 5.3. Also shown is the recycling cavity lineshape. This is measured by sweeping the length of the recycling cavity with the arm cavity off-resonance, and

recording the signal on **pd1** (a measure of the recycling cavity internal power). This is calibrated in terms of frequency by reference to a free-spectral-range of the recycling cavity. The square root of the voltage measured by **pd1** is plotted so that the curve represents the magnitude of the electric field versus frequency. The vertical scale and the horizontal displacement of this curve are adjusted for best agreement with the modulation frequency data.

Sensitivity to misalignment. The sensitivity of the arm cavity to misalignment of the arm cavity mirrors is determined by measuring the mirror rotation needed to reduce the power transmitted by the arm cavity by 15% from its peak value (an arbitrary but useful criterion). In the non-recycled configuration (arm cavity resonant, recycling mirror misaligned), the misalignment necessary is roughly the same for both arm cavity mirrors, and equal to $(1.5 \pm .3) \times 10^{-4}$ radians. In the recycled configuration (both cavities aligned and resonant), the misalignment required to reduce the transmitted power by 15% from maximum is again nearly the same for each arm cavity mirror: the misalignment for the rear mirror being $(3.5 \pm 0.9) \times 10^{-5}$ radians, and for the arm cavity input mirror $(4.6 \pm 0.6) \times 10^{-5}$ radians. This is roughly 4 times more sensitive than the solo arm cavity.

The misalignment sensitivity of the non-recycled cavity is straightforward to model. The coupling of the laser beam into the cavity is determined by the overlap of the beam's spatial mode with the fundamental mode of the cavity. The input beam is assumed to be entirely in the fundamental mode of the perfectly aligned cavity (i.e. the beam is perfectly mode-matched). The overlap of the input beam and the cavity mode can be calculated anywhere along the propagation direction of the beam, but it is simplest if done at the beam waist.

The mirror rotations can be restricted to a single plane without loss of generality, so the problem can be considered in one dimension; I'll make it the x dimension. In one dimension, the field distribution at the waist of the normalized lowest mode of the cavity is

$$u_0(x) = \left(\frac{2}{\pi x_0^2}\right)^{1/4} e^{-x^2/x_0^2}, \tag{47}$$

where x_0 is the waist size. For the plano-spherical cavity geometry, a rotation of the (rear) curved mirror leads to a displacement of the optic axis by an amount $a = \theta R$, where θ is the mirror rotation and R (=1 m) is the mirror radius of curvature. The input beam mode is then described by the distribution $u_0(x + a)$. The fraction of the input power coupled into the fundamental mode of the cavity is

$$\left| \int_{-\infty}^{\infty} u_0(x) u_0(x + a) dx \right|^2 = e^{-a^2/x_0^2} = e^{-\theta^2 R^2/x_0^2}. \tag{48}$$

A rotation of the (front) flat mirror produces a displacement of the optic axis by an amount $a = \theta(R - l)$, where l is the cavity length, and a rotation of the optic

axis by the mirror rotation angle θ. Let the cavity axis and mode be described using the original xz coordinate system, and let the input beam propagate in the z' direction, with field amplitude in the x' direction. The tilt of $x'z'$ system with respect to the xz system produces no change to first order in the magnitude of the input beam:$|u_0(x)| = |u_0(x')|(\cos\theta)^{-1}$. The phase, however, varies to first order along x: $\phi(x) = kx\sin\theta \approx k\theta x$. The fraction of the input power coupled into the cavity fundamental mode as a function of misalignment of flat input mirror is

$$\left| \int_{-\infty}^{\infty} u_0(x) u_0(x+a) e^{ik\theta(x+a)} dx \right|^2 = e^{-\theta^2(R-l)^2/x_0^2} e^{-x_0^2 k^2 \theta^2/4} . \qquad (49)$$

The data can be used to test the model at one point, when the fractional power coupling is $= 1 - 0.15 = 0.85$. For the arm cavity, $x_0 = 0.286$ mm. The model predicts a rear mirror rotation of 0.115 mrad, or a front mirror rotation of 0.158 mrad, will cause the power coupling to fall to 85% of the maximum. This is in fair agreement with the data. The uncertainty in the data comes from the fact that the PZT voltage increment required to reduce the power by 15% was not reproducible to much better than $\pm 20\%$; this is most likely due to nonlinearity and/or hysteresis in the PZTs. The calibrations of the angle producing PZTs have not been measured; the manufacturer specification is used to convert from applied voltage to displacement, and it is possible that a correct calibration could resolve some of the discrepancy.

A simple model for the misalignment sensitivity of the recycled cavity can be made by considering the optic axes in the two cavities to be independent, as follows: The mode in the arm cavity is assumed to be the fundamental mode of the isolated arm cavity, propagating along the cavity axis defined by the arm cavity front and rear mirrors. The mode in the recycling cavity is assumed to be the fundamental mode of the isolated recycling cavity (i.e. the cavity made up of the recycling mirror and the cavity input mirror), propagating along the axis defined by the recycling mirror and the arm cavity input mirror. It is assumed that each cavity remains resonant with the light (this condition is maintained by the servos). There are then two effects contributing to the misalignment sensitivity of the power coupled into the arm cavity. First, there is the effect treated above when a beam's propagation axis is not coincident with the cavity optics axis. The fractional power coupling is given by the above expressions, applied both to the coupling of the input beam to the recycling cavity and to the coupling of the recycling cavity mode to the arm cavity mode. Second, since the optic axes of the two cavities are not coincident in a misaligned system, the arm cavity reflection will present a higher loss to the recycling cavity. This is because that fraction of the beam incident on the arm cavity which is reflected into the mode of the recycling cavity is reduced. The power buildup in the recycling cavity (the recycling gain) will thus be reduced.

This model neglects any effects of the optic axis in one cavity influencing the optic axis in the other cavity. The model is correct in the limit that the arm cavity input mirror has no transmission, for then the arm cavity has no effect on the recycling cavity (but there is no power in the recycling cavity). It is not correct in the limit that the arm cavity input mirror transmission is unity, for then there is only one optic axis defined by the recycling mirror and the rear mirror.

Applying this model to the coupled cavities of Figure 5.1, a rotation of the arm cavity rear mirror produces a displacement of the arm cavity optic axis, but no change in the recycling cavity optic axis. The field reflected from the arm cavity, in terms of the recycling cavity mode, is $\sqrt{R_1}u_0(x) - (T_1\sqrt{R_2}/(1-\sqrt{R_1R_2}))e^{-a^2/2x_0^2}u_0(x+a)$. The first term is the (unshifted) direct reflection from the arm input mirror and the second term is the (displaced) stored beam. The field reflected into the $u_0(x)$ mode of the recycling cavity is thus

$$r_{\rm cav}(0)u_0(x) = \left[\sqrt{R_1} - \left(T_1\sqrt{R_2}/\left(1-\sqrt{R_1R_2}\right)\right)e^{-a^2/x_0^2}\right]u_0(x)\,. \qquad (50)$$

The effective recycling cavity loss due to the arm cavity reflection is $A_{\rm cav} = 1-r_{\rm cav}^2(0)$ and depends on the degree of misalignment.

The arm cavity optic axis displacement for which the arm cavity power drops to 85% of the maximum is $a = 0.03$ mm, as follows: The effective arm cavity reflection coefficient, given the mirror parameters, is $r_{\rm cav}(0) = \left[0.9857 - 1.9449e^{-a^2/x_0^2}\right] = -0.9379$, for $a = 0.04$mm and $x_0 = 0.286$ mm. The arm cavity loss, as viewed by the recycling cavity, is $A_{\rm cav} = 1 - r_{\rm cav}^2(0) = 0.120$, compared with an 8% loss when the arm cavity is perfectly aligned. The recycling gain for $T_{\rm r} = 28\%$, $A_{\rm r} = 1\%$, and a loss $A_2 = 9\% + 12.0\%$ (see Figure 5.2) is $G_{\rm rcc} = 4.44$. The power in the recycling cavity is thus a fraction, $4.51/5.18 = 0.857$, of the power when the system is aligned. A fraction $e^{-a^2/x_0^2} = 0.989$, of the recycling cavity power is coupled into the arm cavity. The coupling of the input beam to the arm cavity is thus reduced from the maximum (aligned case) by a factor $0.857\times0.989 = 0.85$. The arm cavity rear mirror rotation which produces an optic axis displacement of $a = 0.03$ mm is $\theta = 3 \times 10^{-5}$ rad. This is in good agreement with the measured sensitivity of $\theta = 3.5 \pm 0.9 \times 10^{-5}$ rad for an arm cavity power reduction of 15%.

Rotations of the arm cavity input mirror produce displacements and rotations of the optics axes of both cavities. The optic axes are rotated by the same angle, however, so they remain parallel. In this case the coupling of the input beam to the recycling cavity mode changes with alignment, the coupling being given by $e^{-a_{\rm r}^2/x_0^2}e^{-x_0^2k^2\theta^2/4}$, where the displacement of the recycling cavity axis at the waist is $a_{\rm r} = \theta(\mathrm{R_r} - l_{\rm rec}) = 0.05\theta$ m ($\mathrm{R_r}$ is the recycling mirror radius of curvature). The arm cavity input mirror rotation which reduces the coupling into the arm cavity by 15% is $\theta = 5 \times 10^{-5}$ rad, as follows: The coupling of the input beam to the recycling cavity mode for this misalignment is 0.992. The arm cavity effective reflection coefficient is $r_{\rm cav}(0) = \left[0.9857 - 1.9449e^{-a^2/x_0^2}\right] = -0.9393$, where the displacement

is $a = \theta(R_r + R_a - l_{rec} - l_{arm})$ (R_a is the arm cavity rear mirror radius of curvature). The effective cavity reflection loss is $A_{cav} = 11.8\%$. The recycling gain is then $G_{rcc} = 4.48$, a factor of 0.864 of the aligned recycling gain. The coupling of the recycling cavity mode to the arm cavity mode is $e^{-a^2/x_0^2} = 0.990$. The coupling of the input beam to the arm cavity is thus (.992)(.864)(.99) = 0.85. The calculated angle of .05 mrad required to reduce the coupling by this amount is in good agreement with the measured angle of .046 ±.006 mrad.

The measured misalignment sensitivities are not well known because the calibrations of the PZTs have not been measured, but the relative sensitivities for the non-recycled and recycled configurations should not suffer from this uncertainty. For of the arm cavity rear mirror, the required rotation to produce the 15% reduction is a factor of $4.3^{+2.6}_{-1.6}$ smaller in the recycled case. For the arm cavity input mirror, the required rotation is a factor of $3.3^{+1.2}_{-1.0}$ smaller in the recycled case. The model gives a factor of 3.83 for the rear mirror, and a factor of 3.04 for the front mirror.

This model for misalignment sensitivity is applied to a (large-scale) interferometer in chapter 5.4

5.3 Coupled cavities: short recycling cavity

Purpose. In order to reduce the losses in the recycling cavity, the two coupled cavity experiment was performed with a much shorter (0.5 m) recycling cavity, so that the folding mirrors in the 5 m cavity could be removed. This recycling cavity length is too short to use the technique of next free-spectral-range modulation with manageable rf electronics. An alternative technique for generating an arm cavity error signal is a low-frequency modulation of the arm cavity length followed by lock-in detection of the signal transmitted by the arm cavity. The purpose of this experiment is thus to investigate the coupled cavities with a higher recycling gain and to study this alternate scheme for error signal generation.

Setup. The setup for this more compact configuration is shown in Figure 5.4. The arm cavity is still 47 cm long; the recycling cavity is 53 cm long, and the

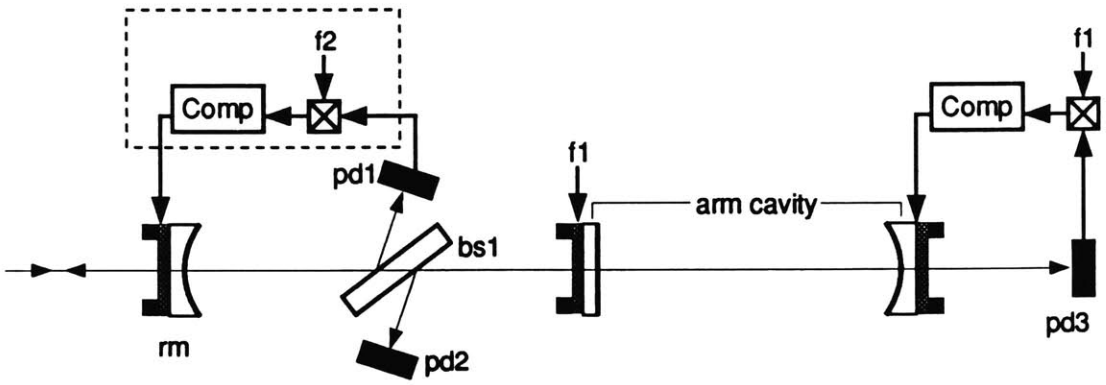

Fig. 5.4. Optical and electronic arrangement for the short recycling cavity experiment.

fundamental modes are matched by using a 1 m radius of curvature recycling mirror.

The beamsplitter **bs1** is a flat plate, mounted at an angle such that 1.6×10^{-4} of the incident light is reflected from each face. The input optics are the same as for the 5 m recycling cavity case, except that the mode-matching lenses are changed as required.

Generation of error signals. The length of the arm cavity is modulated at 60 kHz (f_1) with the arm cavity input mirror/PZT. The light transmitted by the arm cavity is detected by **pd3** and this signal is demodulated at 60 kHz. For modulation frequencies smaller than the cavity linewidth, the relative phase between the transmitted carrier and first sidebands is relatively insensitive to small deviations from resonance (see Fig. A4 in Appendix A). The relative amplitudes of the carrier and sidebands are however first order sensitive to deviations from resonance. (This is the opposite of what happens in the reflection-lock technique, where the relative phases are first order and the relative amplitudes second order sensitive to deviations from resonance.) The demodulated transmitted signal is thus zero when the carrier is at the stationary point in the amplitude curve, i.e. when the transmitted power is at a maximum. Hils and Hall (1987) give a complete treatment of this type of transmission-locking technique for a two mirror Fabry-Perot.

The action of the arm cavity servo is thus to maximize the transmitted power rather than to hold to zero the phase of the reflected field. For a solo cavity, the two techniques give a zero error signal at the same point, when the cavity is at the resonance length. In the coupled cavity configuration, the cavity length modulation works somewhat differently as explained below.

The field transmitted through the coupled cavities is (refer to Fig. 4.2 for definitions)

$$\begin{aligned}\frac{E_T}{E_0} &= \frac{t_r t_1 t_2 e^{i(\theta_r+\theta_c)/2}}{\left(1-r_1 r_2 e^{i\theta_c}\right)\left(1+r_r \hat{r}_{cav} e^{i\theta_r}\right)} \\ &= \frac{t_r t_1 t_2 e^{i(\theta_r+\theta_c)/2}}{1+r_r r_1 e^{i\theta_r}-r_1 r_2 e^{i\theta_c}-r_r r_2\left(r_1^2+t_1^2\right)e^{i(\theta_r+\theta_c)}}\,.\end{aligned} \tag{51}$$

The arm cavity length (θ_c) for which the transmitted power is a maximum depends upon the recycling cavity length (θ_r). For a fixed recycling cavity length, the point of maximum transmission occurs for an arm cavity length ($\theta_c{}^{max}$) of

$$\theta_c^{max} = \tan^{-1}\left[\frac{-r_r t_1^2 \sin(\theta_r)}{r_1\left(1+r_r^2\left(r_1^2+t_1^2\right)\right)+r_r\left(2r_1^2+t_1^2\right)\cos(\theta_r)}\right]. \tag{52}$$

In the limit where $r_r \to 0$ (no recycling mirror), $\theta_c \to 0$; that is, the maximum transmission occurs when the arm cavity is on resonance, as it should. Figure 5.5 shows the arm cavity phase at which the transmission is a maximum versus the recycling cavity phase for $T_1 = .028$, $A_1 = 10^{-4}$, and various values of the recycling mirror reflectivity. The value of $\theta_c{}^{max}$ is quite insensitive to the reflectivity of the recycling mirror, for reflectivities not too small. The slope of these curves at small recycling cavity phase is $d\theta_c/d\theta_r = -1/141$. The phase shift upon reflection from the

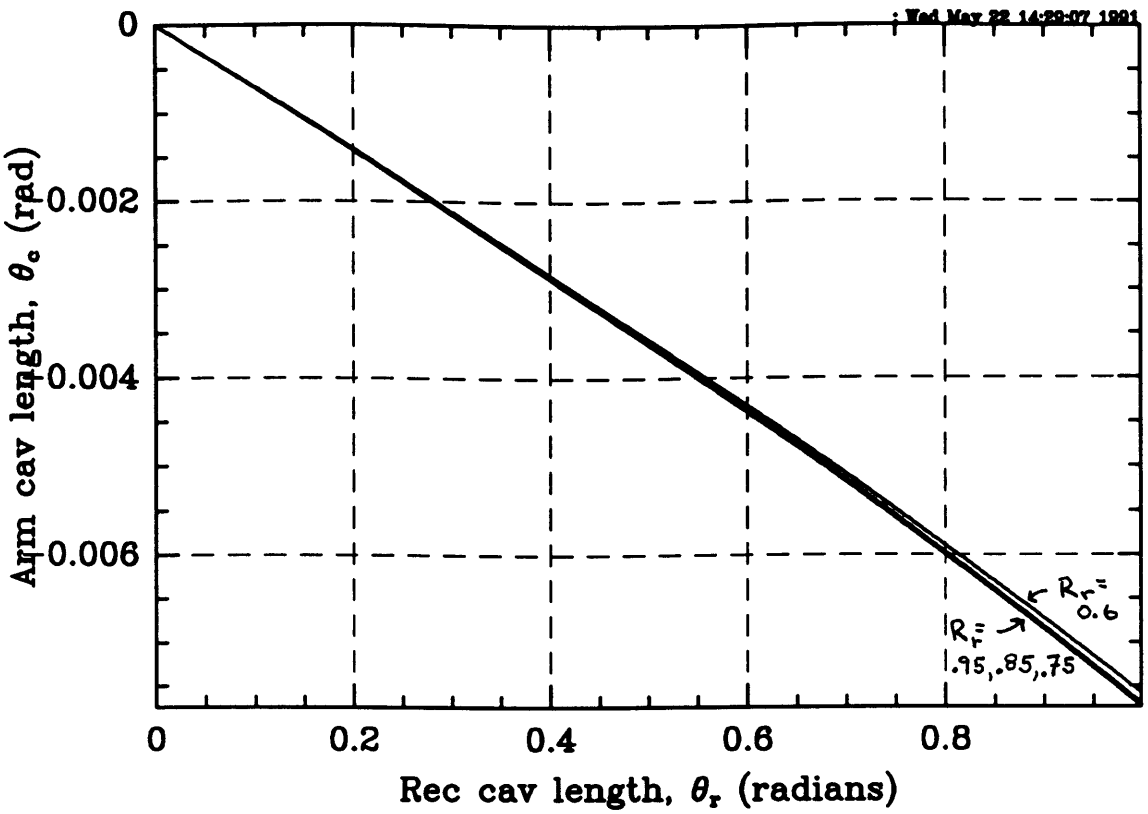

Fig. 5.5 Arm cavity propagation phase corresponding to maximum transmission versus recycling cavity propagation phase, for various values of the recycling mirror reflectivity. $T_1 = 0.028$; $A_1 = 10^{-4}$.

arm cavity (ϕ_c) is related to the arm cavity length by $d\phi_c/d\theta_c \approx 4/T_1 = 143$, and thus $d\phi_c/d\theta_r \approx -1$. So, for a given recycling cavity length, the maximum transmission of the coupled cavities occurs when the total round trip phase in the recycling cavity (made up of propagation phase, θ_r, and arm cavity reflection phase, ϕ_c) is very nearly 0 mod 2π. This means that the arm cavity servo, which operates by maximizing the power transmitted through the coupled cavities, holds the recycling cavity round trip phase to (nearly) zero, rather than keeping the arm cavity itself resonant. The arm cavity servo thus serves to stabilize the recycling cavity phase. For a dc-motion Δx_r of the recycling mirror, the servo thus induces a motion $-\Delta x_r/(4/T_1)$ of the arm cavity rear mirror, while a dc-motion Δx_c of the arm cavity rear mirror is compensated for by a motion $-\Delta x_c$ of that mirror. So the servo is less sensitive to changes in the recycling cavity length than to changes in the arm cavity length by a factor of about $4/T_1$ (= 143 in this experiment). Of course, if the recycling cavity length is constant and resonant ($\theta_r = 0$), the action of the arm cavity servo is just to hold the arm cavity on resonance.

While the arm cavity servo does stabilize both the arm cavity length and the recycling cavity phase as described above, it cannot hold the system at the point of overall maximum power, $\theta_r = \theta_c = n2\pi$. Figure 5.6 shows the power transmitted

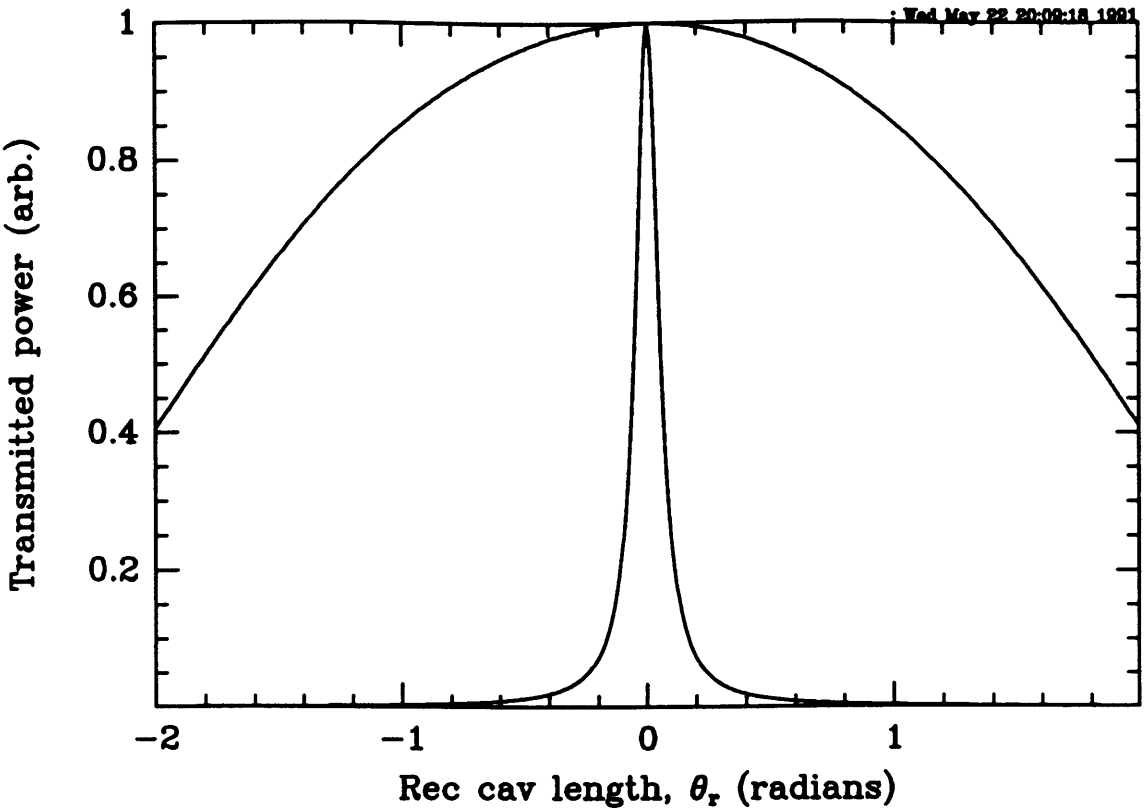

Fig. 5.6 Power transmitted through coupled cavities versus recycling cavity length. For the narrow curve, the arm cavity length is constant at $\theta_c = 0$; for the wide curve, the arm cavity length tracks to stay at a (local) maximum of transmission, $\theta_c = \theta_c{}^{max}$. $T_1 = .028$; $A_1 = 1.1\times10^{-4}$; $A_2 = 6\times10^{-5}$; $R_r = .92$.

through the coupled cavities as a function of the recycling cavity length for the cases when the arm cavity length is fixed at $\theta_c = 0$, and when the arm cavity length is servo-controlled to keep the transmitted power at a maximum with respect to the arm cavity length. For a fixed arm cavity length ($\theta_c = 0$), Fig. 5.6 shows a finesse of about $F = 2\pi/\Delta\theta_r^{fwhm} = 57$, appropriate to the recycling mirror reflectivity of $R_r = .92$ and arm cavity reflectivity of $R_c = .975$. With the arm cavity servo turned on, the 'finesse' is reduced to $F = 1.7$.

Servos. The length of the recycling cavity is stable enough in this experiment that accurate measurements of the overall maximum power can be made without actively stabilizing θ_r. A servo to hold $\theta_r = 0$ was nonetheless demonstrated using a lock-in detection of the recycling cavity internal power as follows. The recycling cavity length is modulated with the **rm** PZT at $f_2 \sim 10$ kHz. The signal detected by **pd1** is demodulated at f2 and the resulting error signal filtered and fed back to **rm**. The power in the recycling cavity is thus maximized. Note that the standard phase modulation reflection locking technique will not work well to stabilize the recycling cavity length. This is because the arm cavity servo holds the round trip phase in the recycling cavity (propagation phase plus cavity reflection phase) nearly constant

at zero, so that neither the carrier phase nor the sideband phase changes much with the recycling cavity length.

The arm cavity error signal is compensated in the standard way: a simple pole at 5 Hz for initial locking, and an additional 1 Hz/860 Hz pole/zero combination for subsequent operation, the unity gain frequency being a few kilohertz. The 60 kHz modulation frequency of the arm cavity length is much lower than the 700 kHz pole frequency of the isolated arm cavity, so that when the system is not recycled the 60 kHz sidebands have essentially zero phase shift with respect to the carrier. With recycling, the linewidth of this system becomes roughly 54 kHz and the pole frequency 27 kHz (see the section below on *Frequency response*). The 60 kHz sidebands thus acquire an additional phase shift of about 65° due to the cavity response. The consequence is that the phase of the local oscillator must be compensated for this when the system is recycled.

Losses and recycling gain. The on-resonance reflectivity of the arm cavity is $R_c = 0.95$, corresponding to an average mirror loss of 1.75×10^{-4} (somewhat cleaner mirrors than for the previous experiment). Of the recycling mirrors then available, the one closest to the optimum had a transmission of $T_r = 8.3\%$, and an estimated loss of $A_r = 0.6\%$. The beamsplitter **bs1** reflects 1.6×10^{-4} of the incident light from each face, for a round trip loss of 0.065%. The loss due to reflection from the AR surface of the arm cavity input mirror is not known, but probably less than the 1% estimated above since these mirrors have had less exposure to the environment (the manufacturer specified 0.2% reflection at the time of manufacture).

The recycling gain, as indicated by the increase in the arm cavity transmitted power (**pd3**), is 16.2 for this configuration. The recycling cavity internal power also increases by this factor, after correcting for the recycling cavity mode-matching of $M = 0.93$. With $T_r = .083$, $A_r = .006$, and additional losses of 5% from the cavity reflection, 0.4% from the arm input mirror AR surface, and 0.065% from **bs1** (for a total loss of 6.065%), the predicted recycling gain is (eq. 46) 16.0. This is in good agreement with the measured gain and indicates that the loss has perhaps been slightly overestimated.

Frequency response. As mentioned, the linewidth of the coupled system is about 54 kHz. The dependence of the transmitted power to the arm cavity length is seen by setting $\theta_r = 0$ in eq. 51:

$$\left.\frac{E_T}{E_0}\right|_{\theta_r=0} = \frac{t_r t_1 t_2 e^{i\theta_c/2}}{1 + r_r r_1 - r_2\left(r_1 + r_r\left(r_1^2 + t_1^2\right)\right)e^{i\theta_c}} = \frac{t_1' t_2' e^{i\theta_c/2}}{1 - r_1' r_2' e^{i\theta_c}} \,. \tag{53}$$

Thus for a constant recycling cavity length, $\theta_r = 0$, the system looks like a two mirror cavity, with $t_1' t_2' = t_r t_1 t_2/(1 + r_r r_1)$, and $r_1' r_2' = r_2\left(r_1 + r_r\left(r_1^2 + t_1^2\right)\right)/(1 + r_r r_1)$. The finesse is thus $F = \pi\sqrt{r_1' r_2'}/(1 - r_1' r_2')$. For this system, these parameters are $r_1' r_2' = 0.995$, which gives a finesse $F = 6000$. With the free-spectral-range of the arm cavity of 320 MHz, the equivalent linewidth due to arm cavity length changes is (320 MHz/6000) = 54 kHz.

The linewidth of the coupled cavity as defined by $\Delta\nu_{rcc}$ in section 4.4 corresponds to the full-width-half-maximum of the recycling cavity internal power as a function of the laser frequency. A numerical solution to eq. 39 gives in this case $\Delta\nu_{rcc}$ = 54 kHz. This linewidth can be seen by measuring the response of the coupled cavities to a frequency modulation of the laser. This experiment is performed by applying a frequency modulation to the laser using the intra-cavity Pockels cell, and detecting the signal reflected from the coupled cavities with the 15 MHz phase modulation/demodulation system. Above the unity gain frequency of the arm cavity servo ($\sim$ 5 kHz), the arm cavity does not hold the recycling cavity round trip phase to zero and the frequency response of the passive system is measured directly. The results of this measurement are shown in Figure 5.7. The frequency response of

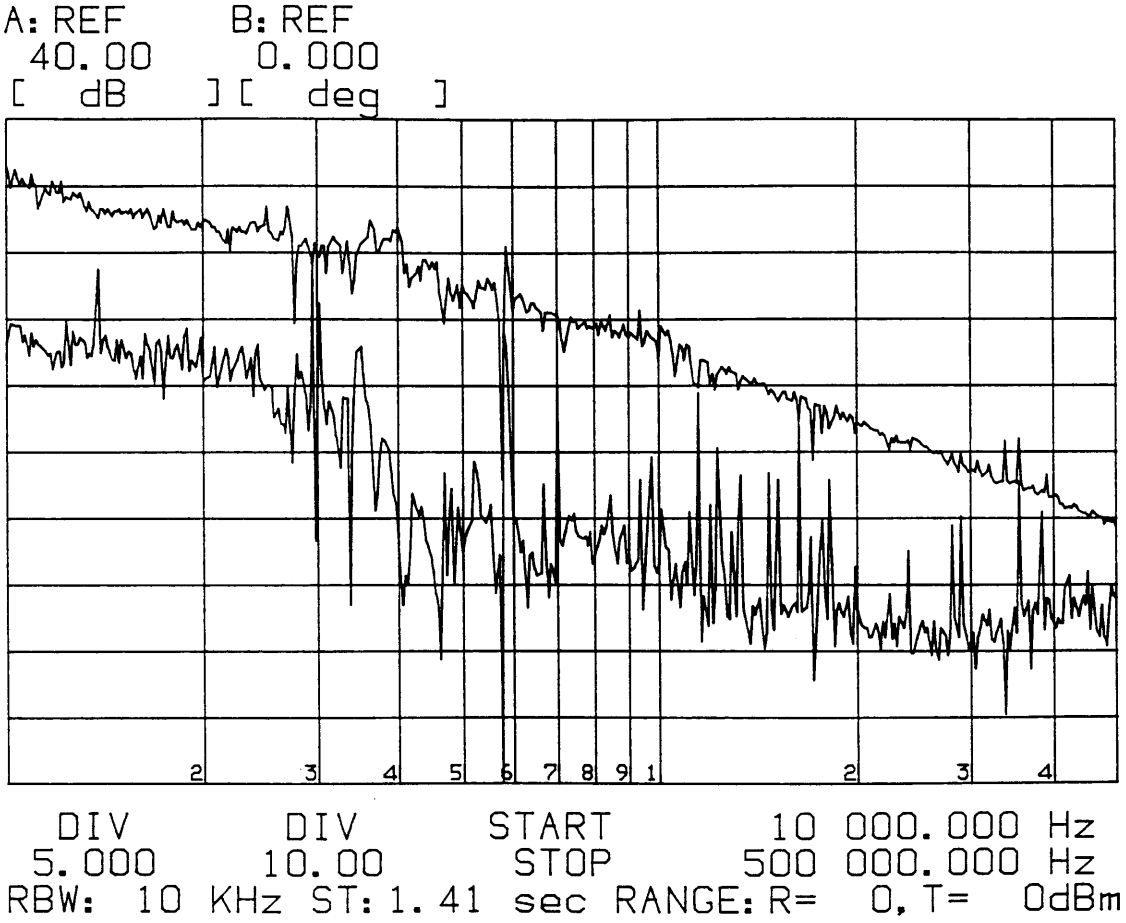

Fig. 5.7 Frequency response of the coupled cavities in reflection to a frequency modulation of the input laser beam. Top: magnitude; bottom: phase.

the electronics is cancelled by dividing the response of the coupled cavities by a reference response made by measuring the frequency response of the recycling cavity alone (which has a pole frequency of about 2.5 MHz). The data below 15–20 kHz is not valid because the servo transfer functions are not the same in the two cases and the division operation does not compensate for this. The phase curve in Fig. 5.7 goes

through $-45°$ at about 30 kHz, and the magnitude curve has a slope of 20 dB/decade above 100 kHz. The phase reaches about $-75°$ at 500 kHz, whereas the phase of a pole at 30 kHz should be $-87°$ at 500 kHz. This discrepancy can be explained by the fact that the reference response contains more than just the frequency response of the electronics; it also contains the frequency response of the recycling cavity alone, which is not perfectly flat up to 500 kHz. With its pole frequency of 2.5 MHz, the recycling cavity contributes about $-11°$ at 500 kHz. Since the frequency response of the recycling cavity is used as a reference by dividing the transfer function of the coupled cavities by the transfer function of the recycling cavity, this means that 11° of phase shift are erroneously added to the coupled cavity transfer function at 500 kHz. This explains nearly all the difference between the measured and expected phase shift at 500 kHz, so that the frequency response of the couple cavities is that of a pole at 30 kHz.

5.4 Recycling of a full interferometer

Introduction. The addition of another Fabry-Perot cavity arm introduces two new degrees-of-freedom into the system: the length of the second arm cavity, and the position of the two arm cavities with respect to the main beamsplitter, i.e. the Michelson phase difference. A new loss mechanism is also introduced: power can be lost through the anti-symmetric output of the Michelson interferometer, as a result of either an imperfect (less than unity) contrast, or a deviation from the dark fringe ($\phi_d \neq 0 \bmod 2\pi$).

The interferometer can be operated in three configurations: the full system with Fabry-Perot cavities in each arm (FP MI); the simple Michelson (MI), using only the input mirrors of the arm cavities (the rear mirrors are physically blocked); and the asymmetric case, with a cavity in one arm and a simple mirror (the cavity input mirror) in the other. Each of these arrangements can be operated with or without recycling.

These recycling experiments are performed with the short ($l_r = 53$ cm) recycling cavity. (The cavities are positioned equidistant from the main beamsplitter, so the recycling cavity length is still defined as the distance from the recycling mirror to a cavity input mirror.) This means that cavity-length-modulation must be used to generate the arm cavity error signals. (Phase modulation at the next free-spectral-range would require modulating/demodulating at $f_m = c/4l_r = 140$ MHz, which is not practical with currently available electronics.)

Description of apparatus. The optical and servo system used is depicted in Figure 5.8. The laser is frequency stabilized as described in chapter 2.3. The optics prior to the recycling mirror are the same as for the coupled cavity experiments (Fig. 5.1).

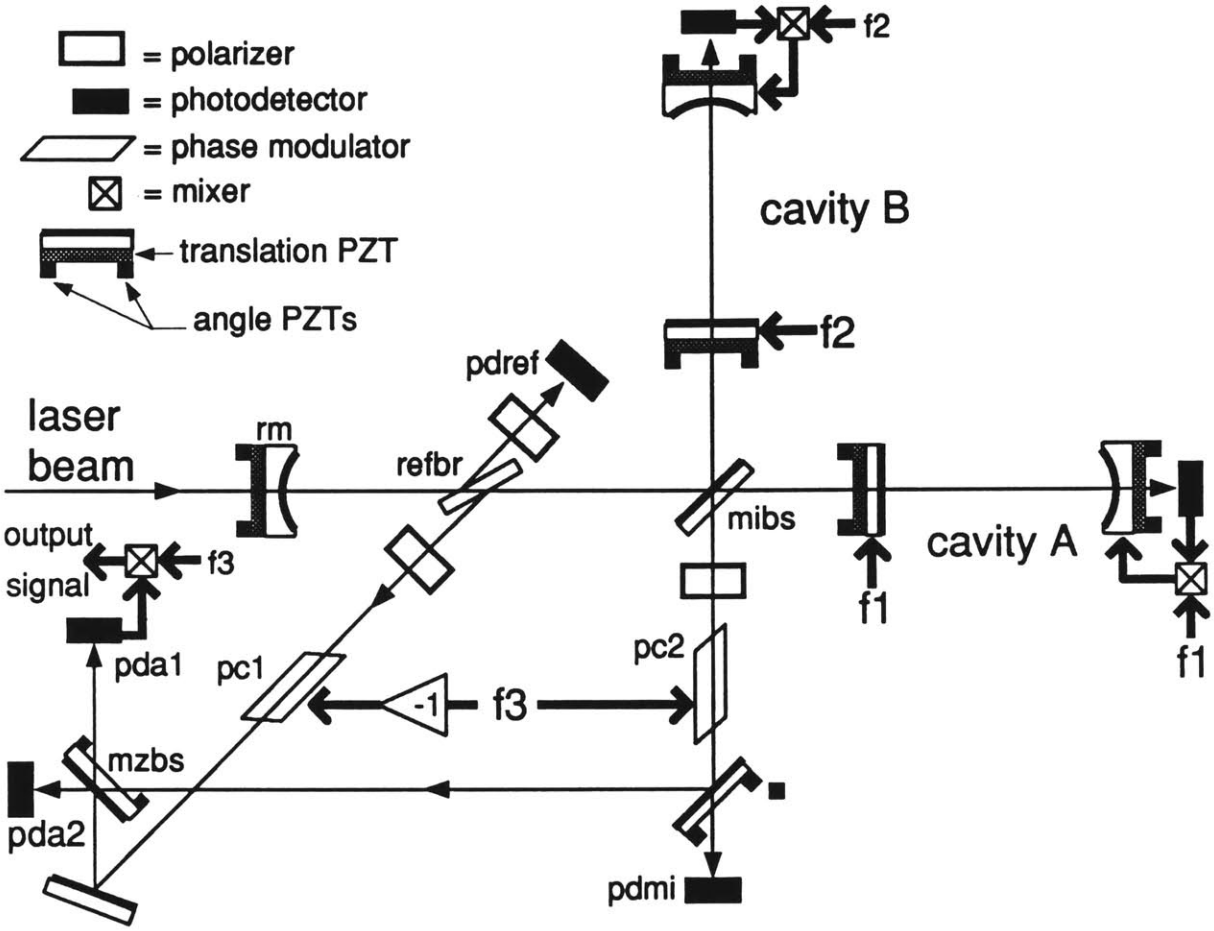

Fig. 5.8. The optical and servo system for the interferometer recycling experiments.

Each of the five main interferometer mirrors (the recycling mirror and the four arm cavity mirrors) is mounted on a PZT allowing about 1 μm of translational control In addition, each mirror is held in a mount outfitted with two PZTs which provide about 3 mrad of remote alignment control in each of the two pertinent angular degrees-of-freedom.

Each arm cavity is 47 cm long and is composed of the, by now standard, T_1 = 2.8% flat input mirror and maximum reflectivity 1 m radius of curvature rear mirror (finesse 220, linewidth 1.4 MHz). The input mirrors are placed 20 cm from the main beamsplitter, **mibs**. The average loss per arm cavity mirror is about 1.2×10^{-4}; this leads to a (on-resonance) loss on reflection of about 3.3% for each cavity (see section **5.1**). Note that this set of mirrors is less lossy than those used in the two coupled cavity experiments; they are from the same batch of mirrors but have had less exposure to the environment. The fraction of the input power coupled into the TEM_{00} mode of each arm cavity (without recycling) is about 95%. The mode-matching, finesse, and losses are the same in the two cavities, to within $\pm$5%.

The recycling mirror, **rm**, has a 1 m radius of curvature and is placed 53 cm from the arm input mirrors, matching the TEM_{00} modes in the recycling and arm cavities just as for the previous experiment. Ideally the transmission of the recycling mirror should be equal to the total loss in the interferometer; the closest match available was an ordinary commercial (CVI) laser mirror of 8.3% transmission and 0.3% estimated loss.

The main Michelson beamsplitter, **mibs**, is nominally 50/50 for p-polarization. The reference beamsplitter, **refbr**, is a flat, uncoated plate mounted at an angle such that it reflects 2.5×10^{-4} of the incident light from each face. The polarizers at each reflection from the reference splitter and at the anti-symmetric output ensure that only the power in the (horizontal) polarization of the input beam is detected.

Also shown in Figure 5.8 are the components comprising the signal detection scheme known as external modulation. This technique will be discussed in detail in the next section. Essentially, the signal at the anti-symmetric output of the Michelson, ϕ_d, interferes with a phase-modulated reference beam. With the appropriate phase between the Michelson output beam and the reference beam, the demodulated output of this Mach-Zehnder interferometer is proportional to ϕ_d.

Error signals and servos. Each arm cavity is held on resonance with the cavity length-modulation and lock-in detection method described in the previous chapter. Different length-modulation frequencies are used for the two cavities, f_1 = 70 kHz for cavity A and f_2 = 90 kHz for cavity B. The actual mirror motion at f_1 of f_2 is about 4×10^{-12} m_{pk} in the recycled configuration; more will be said about this later. Different frequencies are used in order to de-couple the two arm servos from one another, as explained below.

Fluctuations in the length of a cavity, cavity A for example, produce fluctuations in the amplitude and phase of the field reflected from cavity A. Because of the recycling mirror, these fluctuations appear in the input field to cavity B, and thus also in the reflected and transmitted fields of cavity B. The cavity-length-modulation servos work by holding to zero the signal at f_m transmitted by each cavity. If the cavities were modulated at the same frequency and one of the cavities (A for example) were slightly off-resonance, some of the signal at f_m transmitted through cavity B would be due to the field reflected from cavity A. The cavity B servo would misinterpret this signal and cavity B would not necessarily be held to a local maximum of the internal power. We thus modulate the two arm cavities at different frequencies so that length changes of cavity A (B) will not be interpreted by the cavity B (A) servo as length changes of cavity B (A). Note that laser amplitude noise can corrupt the servos in the same way, but the amplitude noise of the laser at 70 and 90 kHz is not large enough to be a problem.

The loop compensation for the arm servos (omitted from Fig. 5.8) is by now familiar: a simple pole at 5 Hz for the initial locking, and an additional 1 Hz/860 Hz pole/zero combination for operation with more low-frequency gain. The control

signals are applied to the rear mirrors of the arm cavities with ±200 V dynamic range amplifiers.

Because of the stabilizing effect of the arm cavity servos as described in section **5.3**, the recycling mirror position is not actively stabilized. The system is also mechanically stable enough that the Michelson phase (the positions of the arm cavities with respect to the Michelson beamsplitter) does not need to be actively stabilized. The fringe operating point is controlled by manually adjusting (using the PZTs) the positions of the near mirrors of the arm cavities, anti-symmetrically with respect to **mibs** (the arm servoes ensure that the rear mirrors track this motion).

While a servo for the Michelson phase is not needed to make accurate measurements, we did attempt to implement a Michelson servo with limited success, making it possible to discuss the problems associated with the scheme we tried. When the system is operating around the dark fringe, a signal proportional to the Michelson phase can be obtained by demodulating the output of photodetector **pdmi** at 70 (or 90) kHz. In our attempt this signal was applied anti-symmetrically to the arm cavity input mirrors. For low frequencies (where the loop gain in the arm servos is large), the arm rear mirrors track the motion of the input mirrors. For frequencies above the unity-gain-frequency (u.g.f.) of the arm servos, the cavities do not stay on resonance. The Michelson phase shift produced by a given input mirror motion is thus larger at higher frequencies because the cavity contributes progressively more phase shift. In addition, the phase shift depends on the frequency. For low frequencies, the arm cavities move as a whole and as an input mirror is moved away from the beamsplitter, the path length in that arm gets longer. At high frequencies, the arm cavities do not move as a whole, and as an input mirror moves away from the beamsplitter, the cavity gets shorter and thus the path length in that arm gets shorter. The transfer function between differential input mirror motion and the Michelson phase shift is a bit strange: the magnitude rises from the low frequency value to a level 140 times higher (for these cavities) at frequencies above the u.g.f. of the arm servos; the phase starts out at zero degrees and fall to -180 degrees at high frequency. The fact that the phase goes negative as the magnitude increases make this a difficult system to compensate. A better scheme would be to control the position of each cavity as a whole (i.e. move both the input mirror and rear mirror of each cavity), but this was not convenient (nor necessary) in this setup.

The system is brought into angular alignment and resonance in steps: First, with the recycling mirror misaligned, the two arm cavities are aligned for maximum coupling to the TEM_{00} modes. Then, with the arm cavities locked on resonance, the Michelson phase is adjusted to the dark fringe and the arm mirrors given further small alignments to achieve the minimum dark fringe. The recycling mirror is then brought into rough alignment (the arm cavities do not remain resonant for this step). With an arbitrary initial length of the recycling cavity, the two arm cavity lengths are adjusted for resonance and held there with the servos. The recycling cavity length is then adjusted for resonance in the recycling cavity, and each mirror

is aligned for maximum power in the system. Note that because of the phase shift upon reflection from an arm cavity (π rad on resonance, ≈ 0 rad off resonance) the recycling cavity resonance length depends on the length of the arm cavities.

Losses and recycling gain. Measurements of the recycling power gain were made for the three configurations of the Michelson interferometer mentioned in the introduction to this section. Photodiode **pdref** monitors the signal reflected from **refbr** and gives a measure of the input power when the recycling mirror is misaligned and a measure of the power gain when the system is recycled.

In the simple Michelson case, the maximum power gain observed is $G_{\rm rcc} = 19.5$. In order to compare with the expected value, an accounting of the measured and estimated loss is shown in Table 5.1.

Loss element	Loss per pass; m=measured, e=estimated	Round trip loss
Cavity input mirror: Transmission	2.8% (m)	2.8%
Cavity input mirror: Reflection from AR coated surface	0.2% (m)	0.4%
Beamsplitter: 50-50 surface	0.3% (e)	0.6%
Beamplitter: AR surface	0.15% (e)	(1/2)×0.3%
Reference beamsplitter	(2)×0.015% (m)	0.06%
Recycling mirror	0.3% (e)	0.3%
Contrast defect	0.02% (m)	0.02%
Total round trip loss = 4.33%		

Table 5.1. Losses for the recycled simple Michelson interferometer.

The estimated losses are based on experience with other optics having the same kind of dielectric coating. The factor of (1/2) for the round trip loss of the beamsplitter AR surface accounts for the fact that this loss occurs only in one arm; the factor of 2 in the loss per pass of the reference beamsplitter accounts for the two surfaces of the splitter. The contrast defect refers to the average fractional power coming out the anti-symmetric port of the Michelson beamsplitter. Using the values of $T_{\rm r} = 8.3\%$, $A_{\rm r} = 0.3\%$, and $A_2 = 4.03\%$ in eq. 46 gives an expected power gain of 20.6. The measured factor of 19.5 is the ratio of the recycling cavity internal power to the total input power. If we correct for the fraction of the input power that is in the $\rm TEM_{00}$ mode of the cavity, $M = 0.95$, the measured increase in the $\rm TEM_{00}$ mode is $G_{\rm rec}^{\rm TEM_{00}} = 19.5/0.95 = 20.5$; the agreement between the expected and measured values is better than the 5% uncertainty in the measured gain (due mostly to uncertainty in the matching).

For the configuration with Fabry-Perot cavities in the arms of the Michelson, the maximum observed gain is $G_{\rm rec}^{\rm TEM_{00}} = 18.0$, corrected for the recycling cavity $\rm TEM_{00}$ mode matching of $M = 0.95$. This is the ratio of the recycling cavity internal power to the input power; the power in the arm cavities, as measured by the cavity transmissions, also increases by this factor (to within ±5%). In this case the loss accounting is shown in Table 5.2.

Loss element	Loss per pass	Round trip loss
Cavity A reflection	3.1% (m)	1/2(3.1%+3.4%)
Cavity B reflection	3.4% (m)	
Cavity A & B input mirrors: Reflection from AR surface	0.2% (m)	0.4%
Beamsplitter, **mibs**: 50-50 surface	0.3% (e)	0.6%
Beamsplitter, **mibs**: AR surface	0.15% (e)	(1/2)×0.3%
Ref. beamsplitter, **refbr**	(2)×0.025% (m)	0.1%
Recycling mirror	0.3% (e)	0.3%
Contrast defect	0.1% (m)	0.1%
Total round trip loss = 4.9%		

Table 5.2. Losses for the recycled Fabry-Perot arm Michelson interferometer.

The effect of the slightly differing loss in the two cavities has been approximated by using the average cavity loss for the round trip loss from the cavities. The expected value of the recycling gain, with $T_{\rm r} = 8.3\%$, $A_{\rm r} = 0.3\%$, and $A_2 = 4.6\%$ in eq. 46, is $G_{\rm rec}^{\rm predicted} = 18.9$. With these losses the recycling gain for the optimal recycling mirror, $T_{\rm r} \approx A_{\rm r} + A_2 = 4.8\%$, would be 20.6; the penalty for using a recycling mirror with transmission somewhat higher than optimum is not high. This is shown in Figure 5.9, where the recycling gain (eq. 46) is plotted as a function of the recycling mirror transmission, for the losses of $A_{\rm r} = 0.3\%$ and $A_2 = 4.55\%$; the recycling gain is much more sensitive to $T_{\rm r}$ if it is smaller than the optimum.

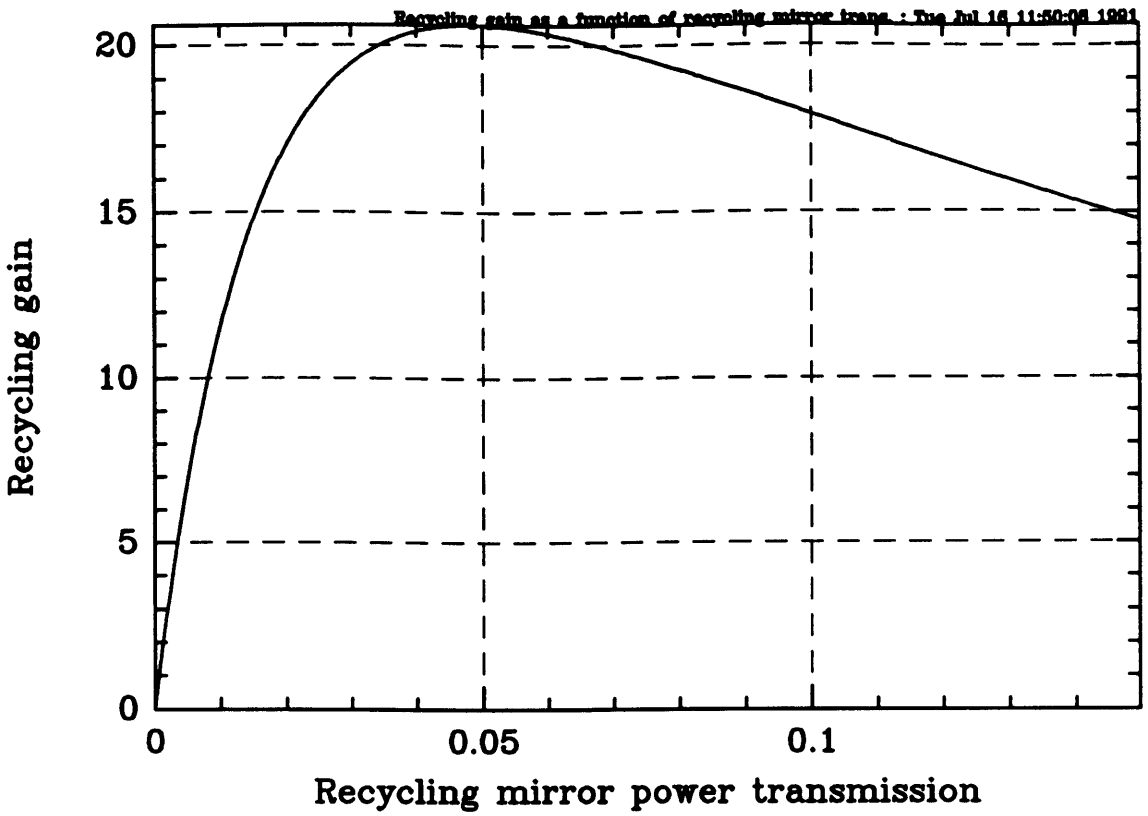

Fig. 5.9 Recycling gain (two mirror cavity model) as a function of the recycling mirror transmission, with mirror losses corresponding to the experiment: A_r=0.3%, A_2=4.55%.

Contrast. The results of the asymmetric Michelson, consisting of a Fabry-Perot in one arm and a simple mirror (the cavity input mirror) in the other, address the question of how the interferometer contrast changes with recycling. In the non-recycled asymmetric configuration, the contrast is poor for the following reason. Light in the cavity arm that does not couple into the cavity does not experience the additional cavity π rad phase shift, but in the simple mirror arm all the light experiences the same phase shift at the mirror. Therefore, at the anti-symmetric output the higher-order modes from the two arms constructively interfere at a Michelson path length difference for which the TEM_{00} modes destructively interfere.

Consider a model where the beams in the two arms are described by the same mode decomposition, and let D(x,y) be the spatial function describing the fundamental mode and F(x,y) describe the light in all the higher order modes, such that $\int \left(|D|^2 + |F|^2\right) dxdy = 1$, and $\int D^* F dxdy = 0$. In the asymmetric configuration, the electric field in one arm is $E_1 = (D + F)e^{i\phi}$, and in the other $E_2 = (D - F)e^{-i\phi}$, where we consider only a phase difference, ϕ, between the arms. The intensity at the output is then $|E_1 - E_2|^2 = 2|D|^2(1 - \cos 2\phi) + 2|F|^2(1 + \cos 2\phi)$. The contrast for this model is $C = \int \left(|D|^2 - |F|^2\right) dxdy = 1 - 2\int |F|^2 dxdy$. The contrast we measure in the non-recycled case is $C = 0.77$, which corresponds to

$\int |F|^2 dxdy = 11.5\%$ of the light contained in higher-order modes. When this system is recycled, the recycling cavity rejects these higher-order modes to some degree. The contrast becomes $C = 0.98$. If this contrast defect is still due to higher-order modes, this implies that the mode-matching of the recycling cavity light into the arm cavities is $M = \int |D|^2 dxdy = 0.99$.

The suppression of higher-order modes can be calculated by using the expression for the ratio of the Fabry-Perot internal power to the incident power for an arbitrary resonance condition:

$$P_{\rm int}/P_{\rm inc} = \frac{T_1}{1 + R_1 R_2 - 2\sqrt{R_1 R_2}\cos\psi}\,, \tag{54}$$

where the parameter ψ specifies how far the light is from resonance. For a plano-spherical cavity of length l and mirror radius of curvature R, $\psi = 2(m+n)\tan^{-1}\sqrt{l/(R-l)}$, where the integers (m,n) are the usual designations for the modes. For the recycling cavity ($l = .53$ m, $R = 1$ m), $\psi = 1.63(m+n)$. Most of the light not in the fundamental mode of the recycling cavity is probably in $(m+n) = 1$ modes. The suppression for these modes is (eq. 54) $P_{\rm int}/P_{\rm inc} = 4 \times 10^{-2}$. The $(m+n)$=2 modes are suppressed by 2×10^{-2}, and the $(m+n)$=3 modes by 5×10^{-2}. The fraction of the incident light in higher-order modes, $|F|^2$, is suppressed by at least 4×10^{-2}, from 11.5% to less than 0.5%. The fact that the contrast is only $C = 0.98$ in the recycled asymmetric case (rather than 0.99 if limited by the effect mentioned above) implies that the fundamental modes of the recycling and arm cavities are not perfectly matched.

For the symmetric arm configurations, the contrast also improves when the system is recycled. In the recycled configurations, the bright fringe power is inferred by scaling the non-recycled bright fringe power (as measured by **pdm1**) by the recycling gain (as measured by the increase in **pdref**); the dark fringe power is still measured directly by **pdmi**. For a contrast near unity, the fractional power lost at the anti-symmetric output is $A_C = P_{\rm min}/P_{\rm max} \approx (1-C)/2$. The measured loss in our system for the various configurations is shown in Table 5.3. The figures refer

simple MI (Michelson)	$A_C = 5.6 \times 10^{-4}$
recycled simple MI	$A_C = 1.5 \times 10^{-4}$
FP MI (Michelson w/ cavities in arms)	$A_C = 1.7 \times 10^{-3}$
recycled FP MI	$A_C = 3.4 \times 10^{-4}$

Table 5.3 The contrast loss for the un-recycled and recycled symmetric configurations.

to the minimum power detected with **pdmi**. In the FP MI configurations, large residual low frequency signals ($f \sim 100$ Hz) make the average power (averaged over $\sim .1$ sec) on **pdmi** about 3–4 times the minimum. It is the average power loss which appears in the loss accounting in Tables 5.1 and 5.2 as the contrast defect. For

both the simple MI and the FP MI the minimum fractional power lost through the anti-symmetric output decreases by a factor of 4–5 when the system is recycled.

A CCD camera was used to obtain the spatial distribution of the dark fringe power. The dark fringes for the FP MI and the recycled FP MI are shown in Figures 5.10 and 5.11, respectively. These figures show that the dark fringe power is not in the TEM_{00} mode, but that it is nearly all contained within a couple of radii of the fundamental mode. The contrast defect is due to non-interfering modes of fairly low order, though not the fundamental mode.

The mechanism(s) for this phenomenon are not so clear. In general, a less than unity contrast is produced by some asymmetry between the two arms. This asymmetry could be caused by a number of mechanisms: a difference in the reflectivities or the figure of the mirrors, a difference in the path lengths, a difference in the wavefront distortion produced in the two arms, a misalignment, etc. For the asymmetric arm configuration, the effect, and how it changes with recycling, is clear. For the symmetric arm configurations, why the effects of a contrast-degrading asymmetry might depend on recycling is not so obvious. The mechanisms I have considered fall into two classes.

The first class, which includes the mechanism for the contrast improvement in the asymmetric interferometer, depends on the input beam containing power in the higher-order modes of the cavities. If there is then some asymmetry which results in a lower contrast for the light in the higher-order modes than for the light in the fundamental mode, the contrast will improve with recycling, since the fraction of the light interfering at the beamsplitter in the higher-order modes is much less. The contrast improvement relies on the 'mode cleaning' of the recycling cavity; if the input light were entirely in the fundamental mode, the contrast would not change. Consider the following two mechanisms which fall into this category.

The input beam can be decomposed into the modes of the recycling (or arm) cavity. The mode-matching into the fundamental mode is typically M = 95%. Because the higher-order modes propagate differently than the fundamental, a length asymmetry could lead to a contrast defect that would improve with recycling, since the higher-order modes are filtered in the recycled system. In particular, a mode of order (n,m) propagates with an extra phase factor $\psi_{n,m} = (n+m)\tan^{-1}(z/z_R)$ relative to the (0,0) mode, where z is the distance from the waist and z_R is the Rayleigh length, $z_R = \pi\omega_0^2/\lambda$. The mode decomposition of the input beam is not known (other than that M = 95%). The mode emerging from the fiber is not a purely gaussian mode, but the overlap of the fiber mode with a gaussian is 99.6% (Marcuse 1970), so the higher-order modes must be produced in the optics between the fiber and the interferometer. The phase $\psi_{n,m}$ changes most rapidly at $z = 0$, where $d\psi_{n,m}/dz = (n+m)z_R^{-1}$; it is possible that one or more higher-order modes could come to a focus (i.e. have $z = 0$) at the photodetector. Then if the differential arm phase for the fundamental mode is 0 rad at the photodetector, the differential arm phase for higher-order modes will be $d\psi_{n,m} = (n+m)dz/z_R$. To estimate this

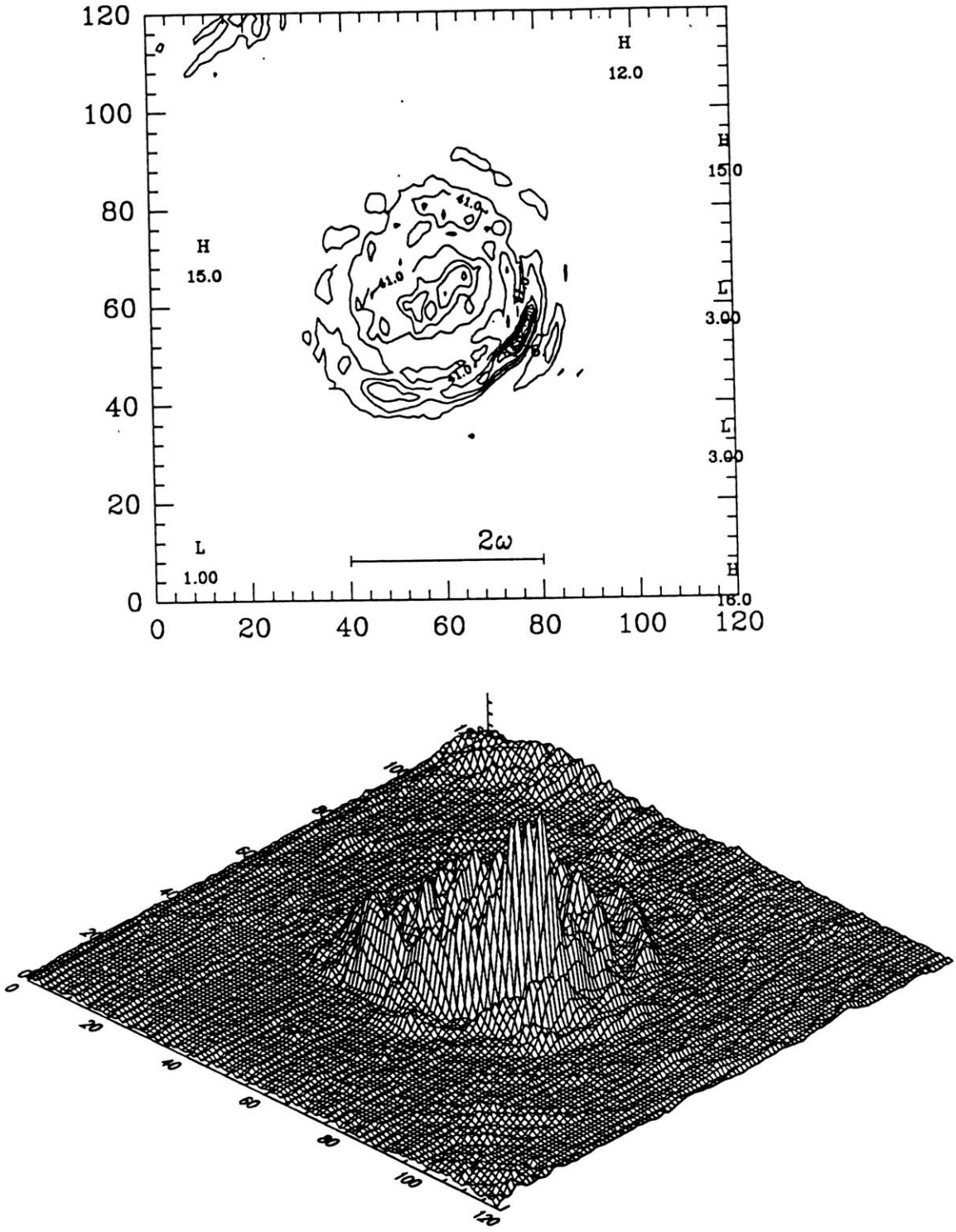

Fig. 5.10 Contour and isometric plots of the spatial distribution of the dark fringe power for the non-recycled Fabry-Perot arm interferometer. The images were taken with a CCD camera using (120 pixels)^2. The calibration is 19.75 μm/pixel. The center of the TEM_{00} mode is at roughly (x,y) = (60,60), determined by adjusting the Michelson path difference for a bright fringe at the anti-symmetric output. The spatial integration of this distribution represents a fractional, time-averaged power of 7.5×10^{-3}.

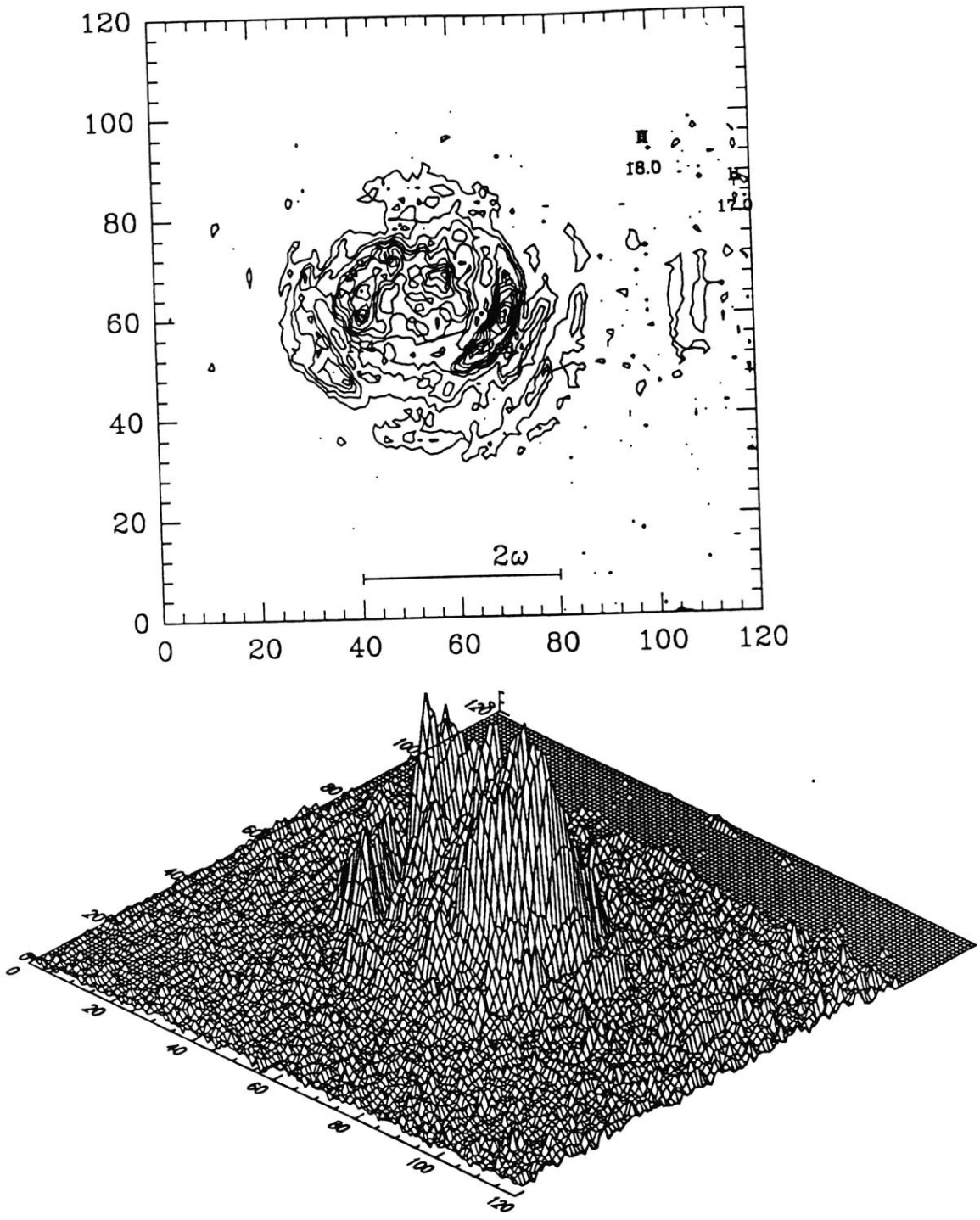

Fig. 5.11 Contour and isometric plots of the spatial distribution of the dark fringe power for the recycled Fabry-Perot arm interferometer. The calibration is 19.75 μm/pixel. The center of the TEM_{00} mode is at roughly (x,y) = (60,60). The spatial integration of this distribution represents a fractional, time-averaged power of 1.5×10^{-3}, a factor of 5 less than the non-recycled case (fig. 5.10). The z-axis calibration (determined by the camera electronics gain) is adjusted in Figs. 5.10 and 5.11 to give a peak intensity close to 256 (corresponding to the full dynamic range of the camera).

effect, take ω_0 for the higher-order modes to be the same as for the fundamental, $z_R = 0.5$ m. For a (possible) path length difference of 2 cm, the extra phase is $d\psi_{n,m} = 0.04(n+m)$ rad. Most of the higher-order light is probably in the $(n+m) = 1$ mode. Then fractional dark fringe power due to this asymmetric phase is $P_{\rm min}/P_{\rm max} \approx (1-M)d\psi_{n,m}^2/4 = 2 \times 10^{-5}$; when the system is recycled the higher-order modes are suppressed by a factor > 10 (see above), making the contrast defect due to this effect negligible. The estimated contrast defect is not large enough to explain the simple Michelson contrast; a knowledge of the mode decomposition of the beam might bring the model prediction closer to the measurement, though the model has been generous in assuming $z = 0$ for the higher-order modes at the photodetector. In addition, this model does not explain the difference between the unrecycled MI and FP MI contrasts.

Wavefront distortion could also have a larger effect on higher-order modes because they have a larger spatial extent than the fundamental mode, and it is likely that the wavefront distortion is greater on larger spatial scales. A simple experiment was done where the $\rm TEM_{00}$ mode size was increased by a factor of 2.5 ($\omega = .71$ mm) at the arm flat mirrors. The contrast of the simple MI did not change with this increase in beam size, indicating either that wavefront distortion on this larger scale is not worse than on the smaller scale, or that wavefront distortion at either scale is not the dominant source of contrast defect. The size of the larger $\rm TEM_{00}$ beam ($\omega = .7$ mm) corresponds approximately to the size of the $(n+m) = 7$ modes (if there were any) of the original smaller beam.

The second class of possible effects involves what might be called 'mode healing'. An asymmetry in the arms that leads to a contrast defect will also lead to a distortion of the beam exiting through the symmetric output of the beamsplitter (i.e. the beam reflected by the interferometer). That is, the mirror formed by the interferometer appears to be distorted. The mode established in the recycling cavity will depend on this distortion. The idea of 'mode healing' is that the mode established in the recycling cavity will compensate for the distortion in the arms in such a way that the contrast loss is smaller than for an un-recycled beam.

It is not clear what type of distortion could lead to a smaller contrast loss. A misalignment of one arm of the interferometer by an angle α, for example, corresponds to a phase gradient $\phi(x) \approx 2\pi\alpha x/\lambda$ across the beam. The symmetric output beam will then have a phase gradient of half that, $\phi_{\rm sy}(x) \approx \pi\alpha x/\lambda$. In a plano-spherical two mirror cavity, this corresponds to a rotation of the flat mirror by an angle $\alpha/2$. The mode in the cavity will change to a $\rm TEM_{00}$ propagating along the new optic axis determined by this angle. In the recycled interferometer, when this new mode propagates into the arms and back to the beamsplitter, the arm beams still meet at an angle α at the beamsplitter, so the interference is unchanged. It is not clear if some other type of distortion could lead to a better contrast.

The question of why the contrast is lower for the configurations with cavities in the arms, as opposed to the simple MI (see Table 5.3), has not yet been addressed.

A likely explanation is that the fundamental modes of the two arm cavities are not identical. The field distributions of the beams reflected from the cavities will then be different. Parts of the input distribution will experience the resonant π phase shift in one arm, but not in the other. This will limit the contrast just as in the asymmetric arm configuration. If the two arm modes are expressed in terms of common and differential parts, the (unrecycled) FP MI contrast of $C = 99.7\%$ requires the power in the differential mode to be 1.5×10^{-3} of the power in the common mode.

In all cases it is important that the contrast is not limited by the modulation. Consider the fields in the two arms before recombination; assuming they have the same magnitude, they are $E_1 = E_0 e^{i\phi_1}$ and $E_2 = E_0 e^{i\phi_2}$. The phases ϕ_1 and ϕ_2 contain the phase modulations, $m_1\sin(\omega_1 t)$ and $m_2\sin(\omega_2 t)$. The normalized minimum intensity at the output (corresponding to $\langle\phi_1 - \phi_2\rangle = n2\pi$) is

$$I_{\rm min} = |E_1 - E_2|^2_{\rm min}/2|E_0|^2 = [1 - \cos(m_1 \sin\omega_1 t - m_2 \sin\omega_2 t)]. \qquad (55)$$

This can be expanded in terms of the Bessel functions. For $\omega_1 \neq \omega_2$, the terms contributing to a dc intensity are $I^{\rm dc}_{\rm min} = (1 - J_0(m_1)J_1(m_2))$. For the case $m_1 = m_2 = m$, and $m \ll 1$, this is approximately $I^{\rm dc}_{\rm min} \approx m^2/2$. For $m \ll 1$, the maximum output is $I^{\rm dc}_{\rm max} \approx 2$, so that $A_C^{\rm mod} = I^{\rm dc}_{\rm min}/I^{\rm dc}_{\rm max} \approx m^2/4$. The modulation index is calculated from the expression for the slope of the Fabry-Perot reflection phase curve, $d\phi/dl = (16\pi/\lambda T_1)$, where $T_1 = .028$ for the arm cavities. Since it is only the differential phase modulation which contributes to the dc intensity at the anti-symmetric output, and the differential phase shift is not affected by recycling, this is the appropriate expression to use. With a mirror motion of 4×10^{-12} $m_{\rm pk}$, the modulation index is about $m = 0.014$. This gives a loss due to modulation of $A_C^{\rm mod} = m^2/4 = 5\times10^{-5}$, more than 3 times less than the measured $A_C = 1.7\times10^{-4}$ for the recycled FP MI.

Misalignment sensitivity. An attempt was made to measure the misalignment sensitivity of the full interferometer. The data was recorded with a computer: the outputs of photodetectors **pdref** and **pdmi** (Fig. 5.8), and the photodetectors monitoring the power transmitted by each cavity, were all recorded with A/Ds as an angle-PZT voltage (also recorded by A/D) was varied around the optimal alignment point. Unfortunately, for unknown reasons the quality of the data is poor; in several instances the power transmitted by one of the arms as a function of the angle-PZT voltage, for example, is multi-valued. It is not possible to extract quantitative results from the data, though it is clear that the interferometer is more sensitive to misalignment (in the sense of the fractional change in an arm cavity power) when it is recycled. Roughly, the recycled interferometer requires an angular misalignment a few times smaller than the non-recycled system in order to reduce the arm cavity power by $\sim$ 10%.

It is worthwhile to apply the misalignment model developed in chapter 5.1 to a full interferometer, in particular to a recycled long baseline interferometer. The model must now take into account the (misalignment dependent) power exiting the

anti-symmetric output. The question becomes not just how the power coupled into an arm cavity depends on misalignment, but how the signal-to-noise ratio of the interferometer depends on misalignment. This issue has also been addressed by Meers and Strain (1991).

In general, a misalignment will decrease the signal (by decreasing the recycling gain and the power coupled into an arm cavity), and increase the noise (by increasing the contrast loss). Of course, it is possible to have a symmetric misalignment in the two arm cavities such that the dark fringe power does not change, but in general both effects will occur. I will consider only a misalignment of the rear mirror of one of the arm cavities. The arm cavities are taken to have a plano-spherical geometry, so that such a misalignment leads to a displacement of the optic axis in that cavity.

Consider first the decrease in the signal. The beam returning to the recycling mirror from the aligned cavity is entirely in the unperturbed mode: $2E_1 = r_{\rm cav} u_0(x)$. The field from the misaligned cavity contains an unperturbed beam and a displaced beam: $2E_2 = (r_{\rm cav} + b)u_0(x) - be^{-a^2/2x_0^2}u_0(x+a)$, where a is the optic axis displacement, x_0 is the waist size, $b = T_1\sqrt{R_2}/\left(1-\sqrt{R_1R_2}\right)$, and $r_{\rm cav} = \sqrt{R_1} - b$ (the subscript 1 refers to the arm cavity input mirror and 2 to the rear mirror, as usual). The additional recycling cavity loss, in the limit of small misalignment $a^2/x_0^2 \ll 1$, is

$$dA_\theta = r_{\rm cav}^2 - \left[\int_{-\infty}^{\infty} (E_1+E_2)u_0(x)dx\right]^2 = \left(\frac{2a}{x_0}\right)^2 \frac{T_1\sqrt{R_2}\left(\sqrt{R_2}(R_1+T_1)-\sqrt{R_1}\right)}{\left(1-\sqrt{R_1R_2}\right)^2}$$
$$\approx \left(\frac{2a}{x_0}\right)^2 \left(1-\frac{4A}{T_1}\right)\left(2-\frac{T_1}{2}-\frac{4A}{T_1}\right), \tag{56}$$

where A is the per mirror loss. The approximate form holds when the arm cavity reflection coefficient is close to one (small reflection loss).

The effect this additional loss has on the recycling gain depends on the losses. The fractional change in the recycling gain is $dG_{\rm rec}/G_{\rm rec} = -G_{\rm rec}dA_\theta$. This gives the change in the recycling cavity power. The power in the aligned arm cavity will also decrease by this factor. The power in the misaligned arm cavity will be reduced further due to the non-unity coupling between the recycling cavity mode and the arm cavity mode. However, as seen in section 5.1, the decrease in the recycling cavity power is the dominant effect; in the subsequent analysis the fractional power decrease in the arms is assumed to be the same and equal to the fractional power decrease in the recycling cavity.

The power at the dark fringe due to the misalignment is proportional to $\left[\int (E_1-E_2)^2 dx\right]$. The fractional dark fringe power due to misalignment is

$$dA_{\rm df}^\theta = \frac{b^2\left(1-e^{-a^2/x_0^2}\right)}{4r_{\rm cav}^2} \approx \left(\frac{a}{x_0}\right)^2 \frac{2T_1}{1+7A/T_1}\,. \tag{57}$$

The approximate relation holds for small misalignment and small arm cavity loss.

The effect of the additional dark fringe power must be analyzed in the context of a signal detection system. The next chapter describes the external modulation scheme for signal detection, and I will use the results from there. In the external modulation system, a small fraction R_e of the circulating light is split off to form a reference field which is than interfered with the anti-symmetric output field. The noise power is proportional to the detected light power: $N \propto (A_C + R_e)^{1/2}$. The fractional change in the noise due to the increased dark fringe power is $dN/N = \frac{1}{2} dA_{\rm df}^{\theta}/(A_C + R_e)$. It is assumed that the misalignment does not change the fractional dark fringe power, A_C, due to other effects (i.e. inherent types of wavefront distortion). There is an optimal value for the fractional power R_e used for the reference beam: $R_e = (A_C(A_C + A_0)/2)^{1/2}$, where A_0 is the interferometer loss not due to a contrast defect (e.g. arm cavity loss).

It is time to put some numbers into these equations. A full-scale interferometer will have mirror parameters of around $T_1 = 3\%$, $A = 10^{-4}$ (giving $R_{\rm cav} = 0.974$). Assuming a (aligned) contrast of $C = 99\%$ ($A_C = 0.5\%$), this allows a recycling gain of $G_{\rm rcc} = 32$ if there are no other losses. The beam waist size will be about $x_0 = 2.8$ cm, resulting from a plano-spherical cavity having a rear mirror radius of curvature R = 10 km.

The fractional change in the recycling gain, and thus signal, is $dG/G \approx -0.3(a/1\text{mm})^2$. The fractional change in the noise is $dN/N \approx 3 \times 10^{-3}(a/1\text{mm})^2$. The signal is reduced much faster than the noise is increased. The signal, and thus the signal-to-noise, is reduced by 10% for a displacement of $a = 0.55$ mm. This displacement is produced by an arm cavity rear mirror rotation of $\theta = a/R = 5.5 \times 10^{-8}$ radians. This is a fairly severe requirement on the stability of the mirror angle.

Scaling the interferometer. Some of the issues involved with scaling this experiment to a long baseline interferometer have already been discussed. The methods of generating the error signals and implementing the servos used here are convenient for this type of fixed-mass prototype experiment. A more attractive technique for a full-scale interferometer is the use of rf-phase modulation to obtain the cavity and Michelson error signals. The coupling of the cavities in a recycled FP interferometer, and the restriction against modulators in the interferometer arms, make this method somewhat complicated to implement. This will be the subject of further experiments with the fixed-mass interferometer.

In addition, the time constants associated with the various error signal will be different (longer) in a full-scale interferometer. The effect of this on the acquisition of the operating state is an important question. Experimental experience with the problem will have to wait for the large system.

Some comments about the losses in a large system can be made. The cavity finesse in these experiments is appropriate to a full-scale interferometer, but the mirror coating technology has improved and (small) mirrors with a loss up to 10 times less than those used in this experiment are now available. Significant further

reductions in the loss could be made by using a Michelson beamsplitter and recycling mirror made with low-loss coatings, and V-coatings for all anti-reflection surfaces. The very small contrast defect is not a significant loss in this experiment, but the beam is small ($\omega_0 \approx 0.3\,\mathrm{mm}$) compared to a full-scale system ($\omega_0 \approx 3\,\mathrm{cm}$); since the phase-front distortions due to the optical elements will be different on these two scales, no conclusions about the contrast in a large system can be made based on this experiment. Nonetheless, if the contrast is not less than $C \approx 0.99$, a power gain of at least 30 should be possible.

6 Signal Detection: External modulation

6.1 Theory of external modulation

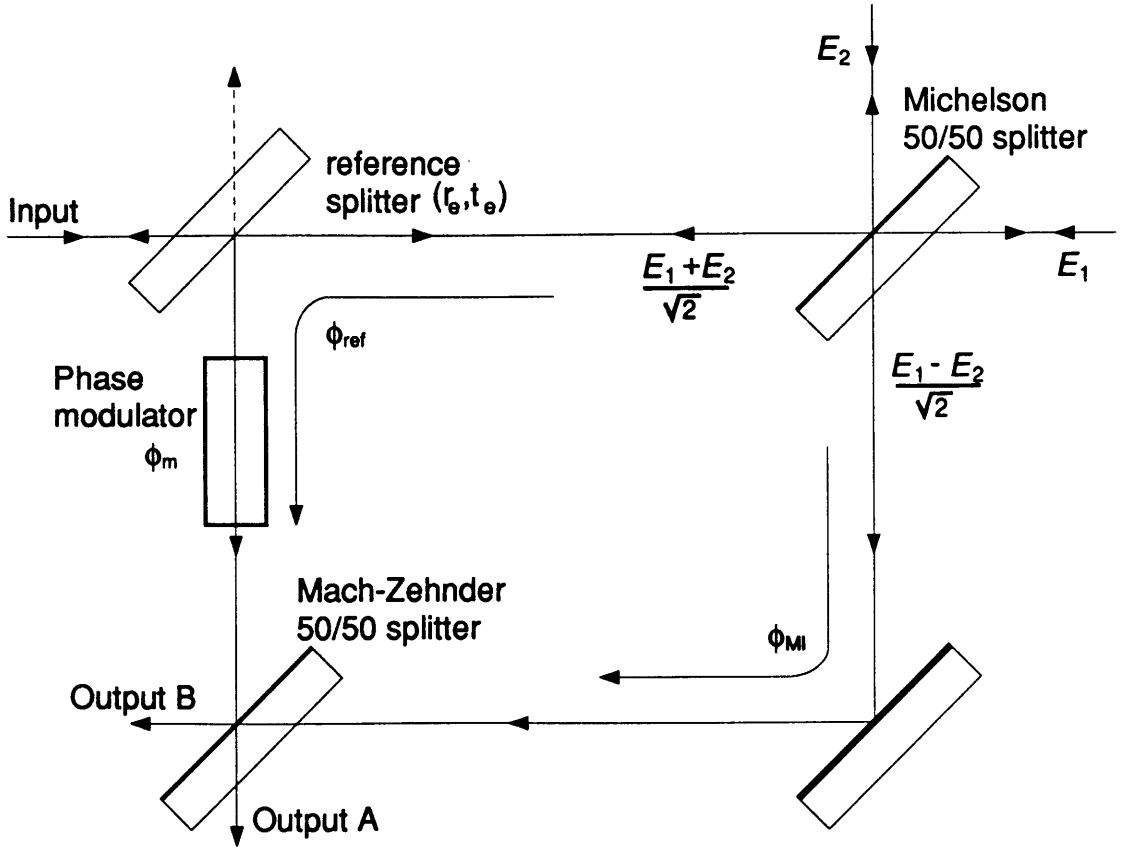

Fig. 6.1 Optical arrangement for external modulation

When an interferometer is operated on the dark fringe, the differential arm phase does not show up directly in the output dc-intensity. In order to detect the differential phase, the output must be interfered with some reference field. In the case of in-line or internal modulation (chapter 3), the carrier in each arm is interfered with the rf-sidebands in the other arm to give an rf signal proportional to the differential phase. For recycling, the phase modulators are removed from the arms and the reference field must be found elsewhere. Such a field can be derived from the main beam, phase-modulated and interfered with the Michelson output

through a Mach-Zehnder arrangement as shown in Figure 6.1 This technique was used on a recycled simple one-bounce Michelson interferometer by Man et al. (1990).

This shows the reference beam being split off from the Michelson symmetric output beam. The reference beam could also be taken from the input beam, before it enters the interferometer. The advantage of the method shown is that the two Mach-Zehnder (MZ) beams can be made to travel equivalent path lengths before interfering at the MZ beamsplitter. This means that the two beams will be the same size, important for the quality of the interference, and that the sensitivity to frequency fluctuations can be minimized. (In practice a second phase modulator is placed in the Michelson arm of the Mach-Zehnder to achieve symmetry.)

In the analysis of this configuration, the field amplitudes and phases in the two arms are broken up into common and differential parts. The spatial distributions of the fields are assumed to be identical, the imperfect contrast coming only from the amplitude imbalance. This may not be the best model in our experimental situation, where the Michelson anti-symmetric output is mostly comprised of light in higher-order modes, but it would probably apply if there were a mode-cleaning cavity or single-mode fiber at the Michelson output, since the light transmitted through the mode cleaner would be in the fundamental mode. The fields in the two arms for this model are

$$E_1 = \sqrt{2}E_0(1+\Delta)e^{i(\phi_c+\phi_d)/2}\,, E_2 = \sqrt{2}E_0(1-\Delta)e^{i(\phi_c-\phi_d)/2}\,. \tag{58}$$

The differential arm phase is thus ϕ_d. The field at the anti-symmetric side of the Michelson beamsplitter is $E_{\rm AS} = (E_1 - E_2)/\sqrt{2}$ and at the symmetric side it is $E_{\rm SY} = (E_1 + E_2)/\sqrt{2}$:

$$\begin{aligned} E_{\rm AS} &= 2E_0 e^{i\phi_c/2}\left[i\sin\frac{\phi_d}{2} + \Delta\cos\frac{\phi_d}{2}\right], \\ E_{\rm SY} &= 2E_0 e^{i\phi_c/2}\left[\cos\frac{\phi_d}{2} + i\Delta\sin\frac{\phi_d}{2}\right]. \end{aligned} \tag{59}$$

The field $E_{\rm AS}$ picks up a phase $\phi_{\rm MI}$ as it propagates to the Mach-Zehnder beamsplitter. The Michelson symmetric output field, $E_{\rm SY}$, reflects from the reference beamsplitter – amplitude reflection $r_{\rm c}$ – and accrues a phase shift of $\phi_{\rm r}$ (including phase modulation) in propagating to the Mach-Zehnder beamsplitter. The field at output A is $E_A = \left[E_{\rm AS}e^{i\phi_{\rm MI}} - r_{\rm e}E_{\rm SY}e^{i\phi_{\rm r}}\right]/\sqrt{2}$ and the intensity is $|E_{\rm A}|^2$:

$$\begin{aligned} E_A &= \sqrt{2}E_0 e^{i\phi_c/2}\left[\left(i\sin\frac{\phi_d}{2} + \Delta\cos\frac{\phi_d}{2}\right)e^{i\phi_{\rm MI}} - r_{\rm e}\left(\cos\frac{\phi_d}{2} + i\Delta\sin\frac{\phi_d}{2}\right)e^{i\phi_{\rm r}}\right], \\ |E_A|^2 &= 2|E_0|^2\Big[\sin^2\frac{\phi_d}{2}(1+r_{\rm e}^2\Delta^2) + \cos^2\frac{\phi_d}{2}(\Delta^2+r_{\rm e}^2) - \\ &\qquad 2\Delta r_{\rm e}\cos(\phi_{\rm MI}-\phi_{\rm r}) + r_{\rm e}(1-\Delta^2)\sin(\phi_d)\sin(\phi_{\rm MI}-\phi_{\rm r})\Big]. \end{aligned} \tag{60}$$

Similarly for output B:

$$E_B = \left[E_{\rm AS}e^{i\phi_{\rm MI}} + r_{\rm e}E_{\rm SY}e^{i\phi_{\rm r}}\right]/\sqrt{2}\,,$$
$$|E_B|^2 = 2|E_0|^2\left[\sin^2\frac{\phi_d}{2}(1+r_{\rm e}^2\Delta^2) + \cos^2\frac{\phi_d}{2}(\Delta^2+r_{\rm e}^2) + \right. \tag{61}$$
$$\left. 2\Delta r_{\rm e}\cos(\phi_{\rm MI}-\phi_{\rm r}) - r_{\rm e}(1-\Delta^2)\sin(\phi_d)\sin(\phi_{\rm MI}-\phi_{\rm r})\right]\,.$$

The reference beam phase, $\phi_{\rm r}$, consists of a propagation phase and a phase modulation: $\phi_{\rm r} = \phi_{\rm r}^0 - m\sin\omega_m t$. The difference between the propagation phases of E_{AS} and E_{SY} is called the Mach-Zehnder phase: $\phi_{\rm MZ} = \phi_{\rm MI} - \phi_{\rm r}^0$. The dc- and ω_m-intensities at output A are then

$$|E_A|^2_{\rm dc} = 2|E_0|^2\left[\sin^2\frac{\phi_d}{2}(1+r_{\rm e}^2\Delta^2) + \cos^2\frac{\phi_d}{2}(\Delta^2+r_{\rm e}^2) - \right.$$
$$\left. 2\Delta r_{\rm e}J_0(m)\cos\phi_{\rm MZ} + r_{\rm e}(1-\Delta^2)\sin(\phi_d)J_0(m)\sin\phi_{\rm MZ}\right]\,, \tag{62}$$

$$|E_A|^2_{\omega_{\rm m}} = 4|E_0|^2 r_{\rm e}\left[2\Delta\sin\phi_{\rm MZ} + (1-\Delta^2)\sin(\phi_d)\cos\phi_{\rm MZ}\right]J_1(m)\sin\omega_m t\,.$$

The sensitivity of the ω_m signal to the differential arm phase, $\phi_{\rm d}$, is greatest when the Mach-Zehnder phase is set to $\phi_{\rm MZ} = 0$ (or $n\pi$). These expressions can be written in terms of the individual beam photocurrents measured after the Mach-Zehnder beamsplitter by either of the two photodetectors:

$$\begin{aligned}
&\text{Michelson minimum: } |E_A|^2 = \tfrac{1}{2}|E_{\rm AS}|^2_{\phi_d=0} = 2|E_0|^2\Delta^2 \Rightarrow I_{\rm MI}^{\rm min}\\
&\text{Michelson maximum: } |E_A|^2 = \tfrac{1}{2}|E_{\rm AS}|^2_{\phi_d=\frac{\pi}{2}} = 2|E_0|^2 \Rightarrow I_{\rm MI}^{\rm max}\\
&\text{Reference beam: } |E_A|^2 = \tfrac{1}{2}r_{\rm e}^2|E_{\rm SY}|^2_{\phi_d=0} = 2r_{\rm e}^2|E_0|^2 \Rightarrow I_{\rm ref}
\end{aligned} \tag{63}$$

The dc currents at the operating point $\phi_{\rm MZ} = 0$ are

$$\begin{aligned}
I_A^{\rm dc} &= I_{\rm MI}^{\rm min} + I_{\rm ref} - 2J_0(m)\sqrt{I_{\rm MI}^{\rm min}I_{\rm ref}}\,,\\
I_B^{\rm dc} &= I_{\rm MI}^{\rm min} + I_{\rm ref} + 2J_0(m)\sqrt{I_{\rm MI}^{\rm min}I_{\rm ref}}\,.
\end{aligned} \tag{64}$$

The ω_m signals are opposite in sign: $S_A = -S_B$. The signal sensitivity to a differential arm phase (at $\phi_d = 0$) is

$$\frac{dS_A}{d\phi_d} = \frac{4C}{1+C}J_1(m)\sqrt{I_{\rm MI}^{\rm max}I_{\rm ref}}\,\sin\omega_m t = -\frac{dS_B}{d\phi_d}\,. \tag{65}$$

The contrast C in this model is $C = (1-\Delta^2)/(1+\Delta^2)$.

The A and B photocurrents are subtracted to give twice the ω_m signal sensitivity. The photocurrent is turned into a voltage by the photodetector/preamplifier. This voltage is then demodulated by the mixer, bringing the signal down to dc. Taking the trans-impedance gain of the preamplification/demodulation process to be R, the signal voltage due to a differential arm phase is

$$v_s(f) = R\left(\frac{dS_A}{d\phi_d} - \frac{dS_B}{d\phi_d}\right)\phi_d(f) = R\frac{8C}{1+C}J_1(m)\sqrt{I_{\rm MI}^{\rm max}I_{\rm ref}}\,\phi_d(f)\,. \tag{66}$$

The noise current is due to the dc photocurrent: $i^2_{\rm noise} = 2e\big(I^{\rm dc}_A + I^{\rm dc}_B + I_{\rm det}\big)$. The current $I_{\rm dct}$ is the equivalent dc-current that would produce the photodetector no-light noise level; this term can also account for a photocurrent due to light which does not contribute to the signal, such as light in higher-order modes. When the noise is demodulated, components above and below the mixer frequency ω_m are mixed down to the same positive frequency and add incoherently, resulting in an additional factor of $\sqrt{2}$.[2] The rms noise voltage which competes with the signal current is then

$$v_{\rm noise}(f) = 2R\sqrt{2e\big(I^{\rm min}_{\rm MI} + I_{\rm ref} + I_{\rm det}/2\big)}\,. \tag{67}$$

Equating the signal and the noise gives an equivalent rms phase noise due to the shot noise of

$$\phi_d(f) = \frac{1+C}{4C}\frac{\sqrt{2e\big(I^{\rm min}_{\rm MI} + I_{\rm ref} + I_{\rm det}/2\big)}}{J_1(m)\sqrt{I^{\rm max}_{\rm MI} I_{\rm ref}}}\,. \tag{68}$$

The sensitivity to the Mach-Zehnder phase, at the operating point $\phi_{\rm MZ} = 0$, is

$$\frac{dS_A}{d\phi_{\rm MZ}} = \left(\frac{2\Delta}{1-\Delta^2}\right)\frac{dS_A}{d\phi_d} = \frac{\sqrt{1-C^2}}{C}\,\frac{dS_A}{d\phi_d}\,. \tag{69}$$

That is, the MZ outputs are less sensitive to the MZ phase, $\phi_{\rm MZ}$, than to the differential arm phase, ϕ_d, by a factor of $C/\sqrt{1-C^2} \approx 1/\sqrt{2(1-C)}$, where the approximation holds for near unity contrast.

Optimum reference beam power. If the interferometer is not recycled, the Michelson bright fringe power can be made independent of the reference beam power by using a Faraday isolator which transmits all of the input light but directs the Michelson symmetric output into the Mach-Zehnder reference arm. In this case, the phase sensitivity is maximized by making the reference beam power much larger than the Michelson dark fringe power (plus detector noise equivalent power). The phase noise is then independent of the reference power and, in the limit of perfect contrast, is equal to $\phi_d(f) = 0.86\sqrt{2e/I^{\rm max}_{\rm MI}}$, using the maximum value of $J_1(m) \approx 0.582$. Note that $I^{\rm max}_{\rm MI}$ is measured after the 50/50 Mach-Zehnder beamsplitter, and thus is half the photocurrent produced by the full Michelson bright fringe beam.

If the interferometer is recycled, the reference beam represents a loss to the recycling cavity and the Michelson bright fringe power is not independent of the reference

[2] For a more explicit treatment of the demodulation process, take the pre-demodulation signal current to be $I_s(f_s)\sin\omega_m t$. The mixer multiplies this by some waveshape of the same frequency, say a sine wave. The resulting current, averaged over many ω_m cycles, is $(1/2)I_s$. The pre-demodulation noise current density at a frequency ω is $I_n = \sqrt{2eI_{\rm dc}}(\sin\omega t + \cos\omega t)$. The components at $\omega = \omega_m \pm \omega_s$ are $I^{\pm}_n = \sqrt{2eI_{\rm dc}}(\sin\omega_m t(\cos\omega_s t \mp \sin\omega_s t) + \cos\omega_m t(\cos\omega_s t \pm \sin\omega_s t))$. Demodulation picks out the $\sin\omega_m t$ term. Each of the noise sidebands thus contributes a noise power density of $(I^{\pm}_n)^2 = 2eI_{\rm dc}/4$. Summing the two noise powers gives a current noise spectral density of $I_n = \sqrt{eI_{\rm dc}}$. So the demodulation process is equivalent to multiplying each pre-demodulation current by a gain R, and multiplying the noise current density by a further factor of $\sqrt{2}$ to account for the two sidebands.

beam power. The recycling gain is related to the losses by $G_{\rm rec} = 1/(A_0 + A_C + 2R_e)$, where $R_e = r_e^2$, A_C is the contrast loss, and A_0 is the remaining loss in the recycling cavity. The various photocurrents are related to the photocurrent I_0 due to the input power by

$$I_{\rm MI}^{\rm max} = \frac{I_0}{2} G_{\rm rec} \; ; \;\; I_{\rm MI}^{\rm min} = \frac{I_0}{2} A_C G_{\rm rec} \; ; \;\; I_{\rm ref} = \frac{I_0}{2} R_e G_{\rm rec} \; , \tag{70}$$

the factors of (1/2) again due to the fact that these photocurrents are measured after the Mach-Zehnder beamsplitter. The phase sensitivity can then be written as $\phi_d(f) = \frac{1+C}{2CJ_1(m)}\sqrt{e/I_0}\,\sqrt{f(R_e)}$. The dependence on the reference splitting coefficient has been put into the function f:

$$f(R_e) = \frac{1}{R_e}\left(A_C + R_e + \frac{I_{\rm det}}{I_0}(A_0 + A_C + 2R_e)\right)(A_0 + A_C + 2R_e) \; . \tag{71}$$

If the detector noise can be neglected, the minimum of this function occurs for a reference-splitter reflectivity of $R_e = \sqrt{A_C(A_C + A_0)/2}$. With this optimum reference beam power, the phase noise due to shot-noise is

$$\phi_d(f) = \frac{1+C}{2CJ_1(m)}\sqrt{\frac{e}{I_0}}\left(\sqrt{2A_C} + \sqrt{A_0 + A_C}\right) \; . \tag{72}$$

The contrast loss affects the shot-noise sensitivity differently than the arm loss (A_0) because the loss A_0 only lowers the signal (by lowering the recycling gain), while the loss A_C both lowers the signal and increases the noise.

Comparison to internal (in-line) modulation In appendix B the shot-noise limited phase sensitivity of an in-line (or internally) modulated interferometer is calculated. In the limit of unity contrast and a noise-less photodetector, the phase sensitivity is

$$\text{Internal mod: } \phi_d(f) \underset{C\to 1}{=} \sqrt{\frac{2e}{I_{\rm max}}} \; . \tag{73}$$

Here $I_{\rm max}$ is the dc photocurrent on the bright fringe, so to compare with external modulation, the substitution $I_{\rm MI}^{\rm max} = I_{\rm max}/2$ must be made. Then, in the limit of unity contrast and $I_{\rm dct} = 0$, and choosing the optimum modulation index (so that $J_1(m) = 0.582$), the phase sensitivity is

$$\text{External mod: } \phi_d(f) \underset{C\to 1}{=} 1.2\sqrt{\frac{2e}{I_{\rm max}}} \; . \tag{74}$$

Note that the fundamental phase sensitivity for internal modulation is the same as for middle-of-the-fringe detection as discussed in chapter 1.3.

6.2 Experimental results

The Michelson output signal was measured with the external modulation technique for the experiments of chapter 5. Figure 5.8 shows the optical and electronic arrangement used for external modulation. The phase modulation is applied in anti-phase to both arms of the Mach-Zehnder, using the standard Gsänger PM-25 Pockels cells. The signal is demodulated at only one of the Mach-Zehnder outputs (**pda1**); the photodetector at the other output (**pda2**) monitors the dc intensities.

When the Mach-Zehnder phase is at the operating point, $\phi_{MZ} = 0$, the sensitivity to a differential arm phase, $dS_{A,B}/d\phi_d$, depends on the Mach-Zehnder phase only in second order. The combination of this insensitivity and the mechanical stability of the system means that accurate measurements of the signal can be made without servo-controlling ϕ_{MZ}.

For the simple one-bounce Michelson interferometer, the expected signal voltage for a motion $\delta x(f)$ of one of the arm mirrors is

$$\delta V_s(f) = \frac{4C}{1+C} R \sqrt{I_{ref} I_{MI}^{max}}\, J_1(m) \frac{4\pi}{\lambda} \delta x(f)\,. \tag{75}$$

The signal at **pda1** produced by the 70 kHz motion of the near mirror of cavity A was measured for the one-bounce Michelson both with and without recycling. The transimpedance gain R of the photodetector/mixer combination is calibrated by measuring the output voltage noise for a known shot-noise producing dc-photocurrent.

In the non-recycled case, the measured signal for a mirror motion of 5×10^{-10} m_{pk} ($\pm 10\%$) is smaller than the expected signal by a factor of 1.23. The parameters for this measurement are: $C = 0.999$; $J_1(m) = 0.386$; $\sqrt{I_{ref} I_{MI}^{max}} = 2.6 \times 10^{-6}$A. With recycling, the signal increases by a factor of 236, while the overall power increases by a factor of 218. The measured signal in this case is thus a factor of 1.14 smaller than the calculated signal size. The dependence of the signal amplitude on the modulation depth for the non-recycled case is shown in Figure 6.2. The maximum modulation index achievable with the Pockels cell driver used is $m = 0.831$. The signal increases proportionally with $J_1(m)$ up to this maximum modulation depth.

In the case with FP cavities in the arms, the signal should increase by a factor of $(4/T_1) = 143$ over the one-bounce Michelson. The measured signal is due to the light in the TEM_{00} mode and must be corrected for the mode matching in comparing to the one-bounce Michelson. The measured increase in the 70 kHz signal, corrected for the mode matching of $M = 0.93$, is a factor of 131, a factor of 1.08 smaller than the expected increase. For the recycled FP MI, the 70 kHz signal increases by an additional factor of 206, while the overall power increases by a factor of 200.

The signal sensitivity to the Mach-Zehnder phase, $dS_{A,B}/d\phi_{MZ}$, is smaller than the sensitivity to the differential arm phase by a factor of $C/\sqrt{1-C^2} \approx 1/\sqrt{2(1-C)}$, as shown above. Assuming the reference beam interferes only with the TEM_{00} component of the Michelson beam, the contrast C in this expression must

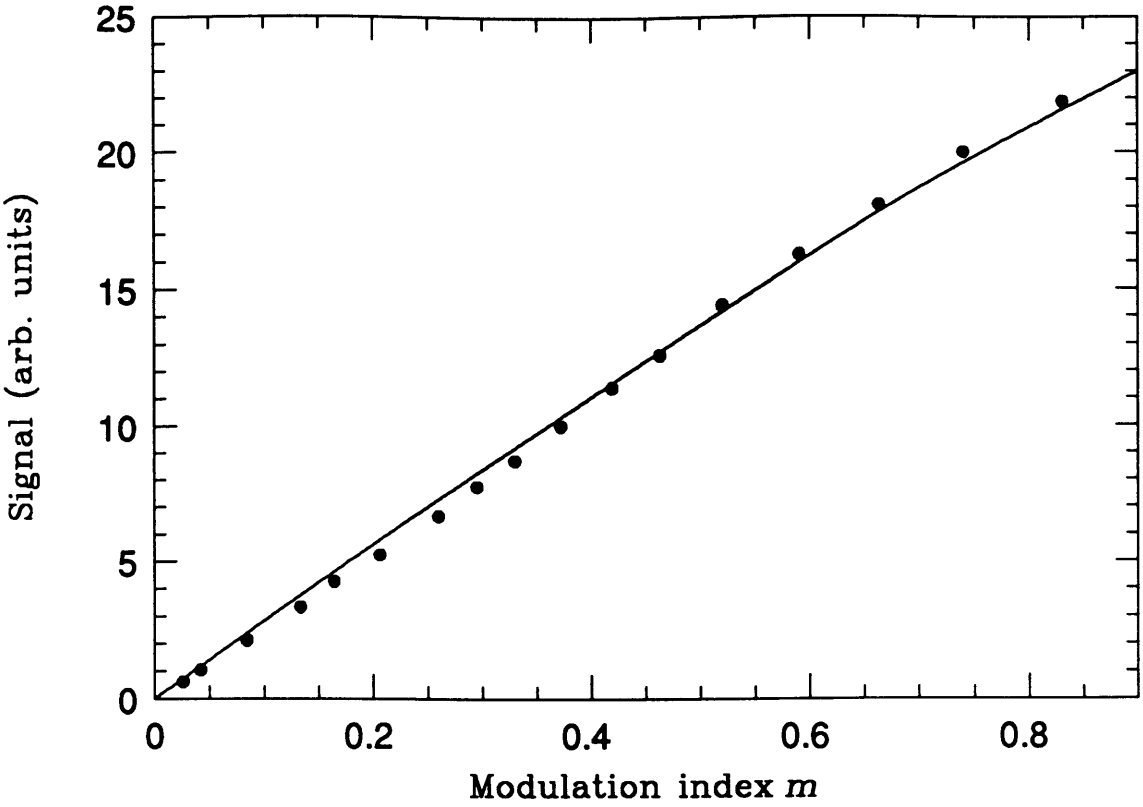

Fig. 6.2 The level of the 70 kHz signal, as detected with the external modulation technique, as a function of the modulation index, m. The curve is $J_1(m)$, scaled for the best fit to the data.

be that for the TEM_{00} component of the Michelson beam. The spatial intensity pattern at the Michelson anti-symmetric output shows that the light at the dark fringe is dominated by modes of higher order than the TEM_{00} mode. The measured contrast can be used to obtain a lower limit for the sensitivity factor; for the recycled one-bounce Michelson, this gives $1/\sqrt{2(1-C)} \geq 40$. By comparing the MZ output signal generated by applying a signal to the MZ Pockels cell to the MZ output signal generated by a Michelson path length difference signal, the sensitivity to the Mach-Zehnder phase is measured to be 200–1000 times smaller than the sensitivity to the Michelson phase. This is consistent with the calculated lower limit of 40.

The noise was also measured with the external modulation arrangement. No attempt was made to optimize the reference beam power; the reference beamsplitter power reflection coefficient of 2.5×10^{-4} (per surface per pass) – determined by its angle – was chosen to be as large as possible while still presenting a relatively small loss to the recycling cavity. For the one-bounce Michelson, using a single photodetector, the shot-noise equivalent single mirror motion sensitivity is

$$\delta x(f) = \frac{\lambda}{\pi}\frac{1+C}{8C}\frac{\sqrt{e(I_{\rm dc}^{\rm ext}+I_{\rm det})}}{\sqrt{I_{\rm MI}^{\rm max}I_{\rm ref}}\,J_1(m)}\,, \tag{76}$$

where $I_{\rm dc}^{\rm ext}$ is the dc photocurrent in the detector at the Mach-Zehnder operating point. For the recycled one-bounce Michelson, the output noise (for frequencies

above about 30 kHz) is a factor of 1.4 greater than the shot-noise due to the effective bright fringe dc-photocurrent of $I_{\rm MI}^{\rm max} = 40\,{\rm ma}$ (the light bulb test). The equivalent displacement noise measured is $9.5 \times 10^{-16}\,{\rm m}/\sqrt{\rm Hz}$. The shot-noise contribution, as inferred from the light bulb test, is $6.8 \times 10^{-16}\,{\rm m}/\sqrt{\rm Hz}$.

The theoretical shot-noise contribution can be calculated using the parameters of the system: $I_{\rm dc}^{\rm ext} = 1.6 \times 10^{-5}\,{\rm A} = I_{\rm det}; I_{\rm ref} = 1.13 \times 10^{-5}\,{\rm A}; J_1 = .386; C = .999$. The calculated shot-noise limited sensitivity is $3.6 \times 10^{-16}\,{\rm m}/\sqrt{\rm Hz}$, a factor of 1.9 lower than the measured shot-noise contribution. The reason for the discrepancy is not completely clear. The signal size is lower than expected by the factor of 1.23 mentioned above. The measured sensitivity is accurate to about ±15%, due mostly to uncertainty in the PZT calibration; the uncertainty in the expected sensitivity is somewhat better than this, probably around ±5%, due to uncertainties in the modulation index and the currents.

For the recycled Fabry-Perot Michelson, the output noise is much larger than the contribution due to the shot-noise and limited by various unidentified mechanical resonances. In addition, relatively large low frequency signals saturate the photodetector for Mach-Zehnder modulation depths in excess of about $m = 0.025$. It is clear that a fixed-mass, in-air system is not suitable for detailed noise studies.

7 Final remarks

To summarize, a small, fixed-mass prototype has been used to study various interferometric techniques being proposed for use in a large baseline gravity wave detector. Such a prototype is a useful tool for the investigation of optical techniques, with the limitation that detailed noise studies cannot be done, and that some of the properties associated with the scale of the interferometer cannot be realized.

The technique of in-line modulation is the most convenient means of operating a Fabry-Perot arm interferometer, as long as the modulation cancellation effect is countered. However, the placement of modulators in the interferometer arms is undesirable in a recycled system. The optical distortion and loss due to the modulators lower the contrast and limit the recycling gain.

Light recycling appears to be a practical technique for increasing the effective light power. In addition, for a given phase shift (i.e., a given mirror motion), the output signal of the external modulation detection system is seen to increase linearly with the effective light power; this is true even for mirror motion frequencies higher than the coupled-cavity pole frequency of ~ 25 kHz, indicating that light recycling does not alter the bandwidth of the system. The recycling gain of 18 seen in this experiment follows from the known optical loss in an understandable way, and could be increased by using available lower-loss optics throughout the interferometer. In a full-scale interferometer, an arm storage time of $\tau_s = 0.8$ msec ($f_0 = 100$ Hz) for a 4 km cavity corresponds to an input mirror transmission of $T_1 = 3.3\%$. A mirror loss of 100 ppm then gives a cavity loss of 2.4%; if mirror coating technology can

produce large mirrors of 10 ppm loss, the arm cavity loss would drop to 0.24%. It should be possible to make the losses in the other optics – the main beamsplitter, the recycling mirror, and any other beamsplitter plates – much smaller than the arm cavity loss. The contrast loss will depend on the quality of the optics on spatial scales much larger than the 0.3 mm beam size in this experiment, making it impossible to predict the contrast loss for a full-scale system based on these experiments. However, a realistic goal for a large system is a contrast of $C = 0.99$, giving a contrast loss of $A_C = 0.5\%$; a wavefront distortion between the two arms of roughly $\lambda/30$ on spatial scales of the beam diameter and smaller would degrade the contrast to this level.

The dependence of the contrast on recycling remains an open question. There as yet is no convincing explanation for the observed decrease in the contrast loss with recycling. The question deserves more experimental work, to see if the effect is reproducible. Computer modeling of the effects of wavefront distortion in a recycled interferometer may be the best path to gain understanding.

In short, there appears to be no fundamental limitation to achieving a recycling factor of at least 30 (the initial LIGO goal) in a large baseline system. Coupled with the 1–1.5 W of laser power at the input of the interferometer easily available with current Argon ion lasers, recycling should produce the 30–40 W of effective laser power needed to bring the shot-noise limited sensitivity of an initial LIGO to around the $h(f) \simeq 3 \times 10^{-23}/\sqrt{\text{Hz}}$ level.

The model for the misalignment sensitivity indicates that a recycled interferometer is much more sensitive to misalignment of the arm mirrors than a non-recycled interferometer. For a full-scale interferometer the alignment requirements are fairly severe: the models predicts a 10% decrease in the power coupled into an arm cavity (i.e. the useful power) for a mirror misalignment of $\theta \simeq 5 \times 10^{-8}$ radians. For a 20 cm diameter mirror, this corresponds to a displacement of 5 nm at the edge of the mirror.

Another issue not fully addressed in this thesis is the modulation and servo topology appropriate for a recycled large baseline interferometer. The error signal generation and servo methods used here are convenient for this type of prototype. The cavity-length-modulation technique used is unsuitable for a full-scale interferometer for a number of reasons. Modulating at a frequency much smaller than the cavity linewidth of $\sim 200\,\text{Hz}$ would lead to a servo with a very small bandwidth. If the modulation were applied at a frequency above the gravity wave band, it would be difficult to attain sufficient modulation depth, as this would require relatively large motions of the mirrors. In addition, applying such forces to the mirrors without introducing significant noise (random mirror motion) may be difficult to do.

For these reasons, a phase modulation system for generating the arm and recycling cavity error signals is required for a full-scale interferometer. The signal detection technique of external modulation used here is applicable to a large system, though these experiments did not answer the questions of how best to generate error signals for the Michelson and Mach-Zehnder path lengths; a phase modulation

system for generating these error signals is also required. A mock-up of a possible phase modulation system for a full-scale interferometer will be tested using this prototype in the near future. Many of the practical difficulties of such a system stem from the cavity coupling phenomena illuminated in these experiments. This will be the topic of a future thesis (or theses), and so will not be elaborated upon here.

Appendix A: The Fabry-Perot cavity

Reflection and transmission coefficients. The optical Fabry-Perot cavity is ubiquitous in this thesis. This appendix contains a derivation of the many formulae used for these resonators. Specifically, this includes the response of a single and a double (recycled) Fabry-Perot to monochromatic light, the response of a FP to a gravity wave (a time varying length change), and the response to a frequency modulated 'monochromatic' field. Since I will treat these topics somewhat independently, the approach will not be the most general formulation conceivable, but I believe it better illuminates some of the physics involved.

Figure A1 shows a FP cavity made of two mirrors (shown as plane mirrors, but they could be of any figure) separated by a distance l. The following definitions are made:

r_1 = amplitude reflection coefficient of input mirror from substrate side
$-r_1$ = amplitude reflection coefficient of input mirror from cavity side
t_1 = amplitude transmission coefficient of input mirror
$-r_2$ = amplitude reflection coefficient of rear mirror from cavity side
t_2 = amplitude transmission coefficient of rear mirror

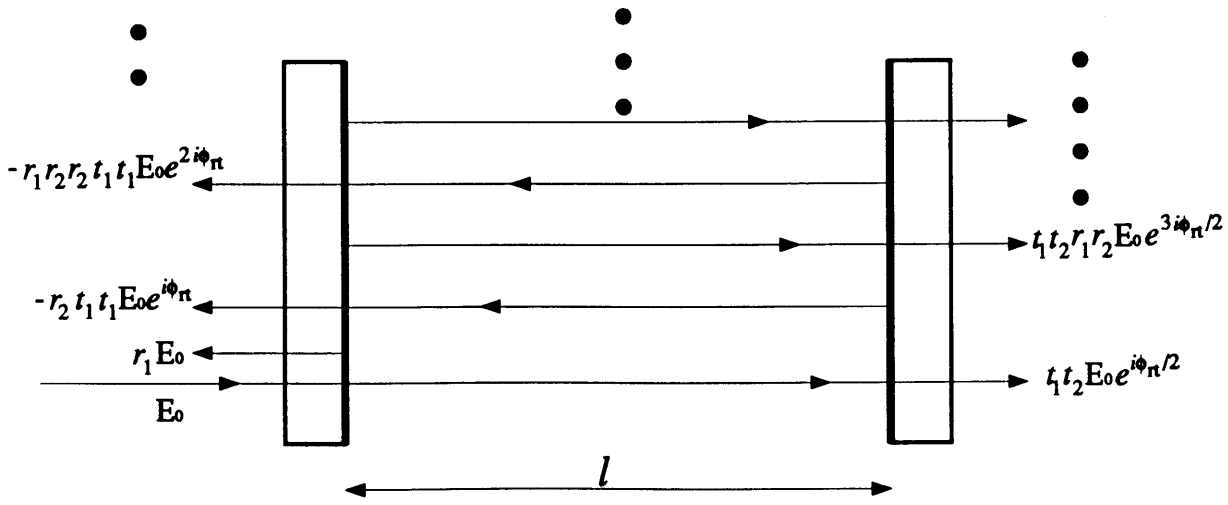

Fig. A1. Fabry-Perot cavity

Here all the r_i and t_i are taken to be positive, and the sign change is explicitly associated with those reflections impinging from the cavity side of a mirror. The incident electric field is $\mathcal{E}_0 = E_0e^{i(\omega t-kz)}$and the reflected field is denoted by $\mathcal{E}_r$. Considering the steady state case, the reflected field is found by adding up all fields at the input mirror (substrate side) traveling in the negative z direction at a given

time. Taking the phase accumulated after a cavity round trip to be negative, $\phi_{rt}= -2kl = -\theta$, this gives

$$\begin{aligned}\mathcal{E}_r/\mathcal{E}_0 &= r_1 - r_2t_1t_1e^{-i\theta} - r_1r_2r_2t_1t_1e^{-2i\theta} - r_1r_2r_1r_2r_2t_1t_1e^{-3i\theta} - \cdots \\ &= r_1 - t_1^2r_2\sum_{n=0}^{\infty}(r_1r_2)^n e^{-in\theta} \\ &= \frac{r_1 - r_2(r_1^2+t_1^2)e^{-i\theta}}{1 - r_1r_2e^{-i\theta}} \equiv \hat{r}_{cav} \,.\end{aligned} \tag{77}$$

The circumflex, $\hat{}$, denotes a complex quantity. Similarly, the transmitted field is

$$\begin{aligned}\mathcal{E}_t/\mathcal{E}_o &= t_1t_2e^{-i\theta/2} + t_1t_2r_1r_2e^{-i3\theta/2} + t_1t_2r_1r_2r_1r_2e^{-i5\theta/2} + \cdots \\ &= t_1t_2e^{-i\theta/2}\sum_{n=0}^{\infty}\left(r_1r_2e^{-i\theta}\right)^n \\ &= \frac{t_1t_2e^{-i\theta/2}}{1 - r_1r_2e^{-i\theta}} \equiv \hat{t}_{cav}\end{aligned} \tag{78}$$

Taking r_1 and r_2 to be real (equivalent to neglecting any additional phase shift at the mirror surface), they are related to the mirror intensity transmission T and absorption A by $r_i = \sqrt{1 - T_i - A_i}$. The amplitude coefficient for reflection, $\hat{r}_{cav}$, can be written in complex exponential notation as $\hat{r}_{cav}=A(\theta)e^{i\phi(\theta)}$. Defining

$$\begin{aligned}\mathrm{A}^2 &= (1 - A_1 - T_1)\,, \\ \mathrm{B}^2 &= (1 - A_2 - T_2)(1 - A_1)^2\,, \\ \mathrm{C}^2 &= (1 - A_1 - T_1)(1 - A_2 - T_2)\end{aligned} \tag{79}$$

$\hat{r}_{cav}$ becomes:

$$\hat{r}_{cav}(\theta) = \left[\frac{\mathrm{A}^2 - 2\mathrm{AB}\cos\theta + \mathrm{B}^2}{1 - 2\mathrm{C}\cos\theta + \mathrm{C}^2}\right]^{1/2} \exp i\left[\tan^{-1}\left(\frac{\mathrm{B}\sin\theta}{\mathrm{A} - \mathrm{B}\cos\theta}\right) - \tan^{-1}\left(\frac{\mathrm{C}\sin\theta}{1 - \mathrm{C}\cos\theta}\right)\right] \tag{80}$$

Similarly for the transmitted field:

$$\hat{t}_{cav} = \left[\frac{T_1T_2}{1 - 2\mathrm{C}\cos\theta + \mathrm{C}^2}\right]^{1/2} \exp i\left[-\theta/2 - \tan^{-1}\left(\frac{\mathrm{C}\sin\theta}{1 - \mathrm{C}\cos\theta}\right)\right] \tag{81}$$

The magnitude and phase of $\hat{r}_{cav}$ are plotted separately in Fig. A2 for the parameters A_1=A_2=10^{-4}, T_2=0, and various values of T_1. Figure A3 shows how $\hat{r}_{cav}$ behaves as the mirror loss is increased for a fixed input mirror transmission. The reflection coefficient is qualitatively different depending on whether the loss ($A_{total} = T_2 + A_2 + A_1$) is less than or greater than the transmission of the input mirror. The critically matched case, $\hat{r}_{cav}(0) = 0$, corresponds to A = B, or in the case of small

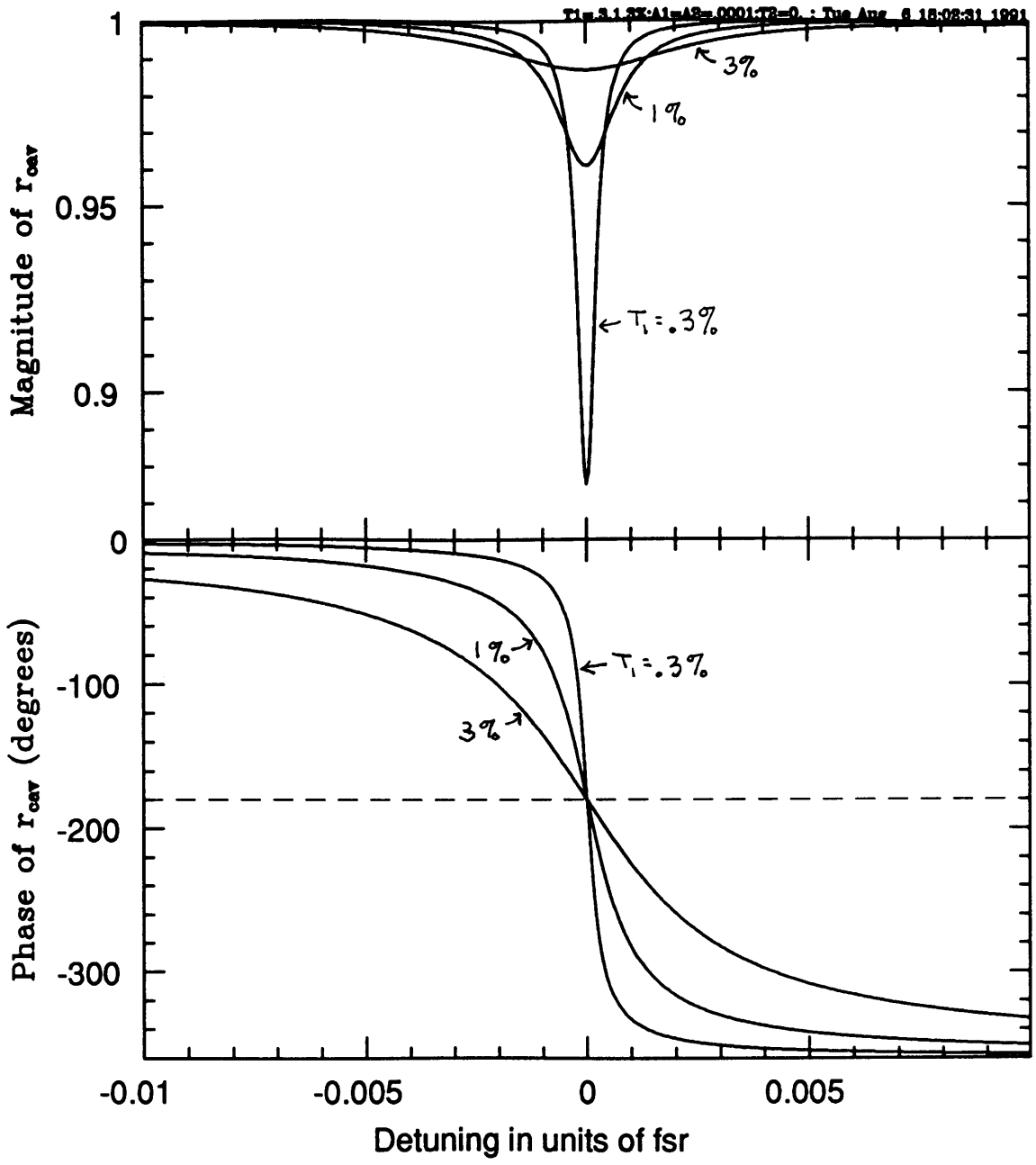

Fig. A2 Magnitude and phase of $\hat{r}_{cav}$ for A_1=A_2=10^{-4}, T_2=0, and T_1=0.3,1.0, and 3.0%.

losses ($<<$ 1), $T_1 \approx T_2 + A_2 + A_1$. When the loss is zero, $|\hat{r}_{cav}(\theta)| \equiv A(\theta) = 1$ for all values of T_1 and θ.

The magnitude and phase of $\hat{t}_{cav}$ are plotted in Figure A4 for the parameters A_1=A_2=10^{-4}, T_2=10^{-3}, and various values of T_1.

In terms of the power coefficients for reflection and transmission, R_i =

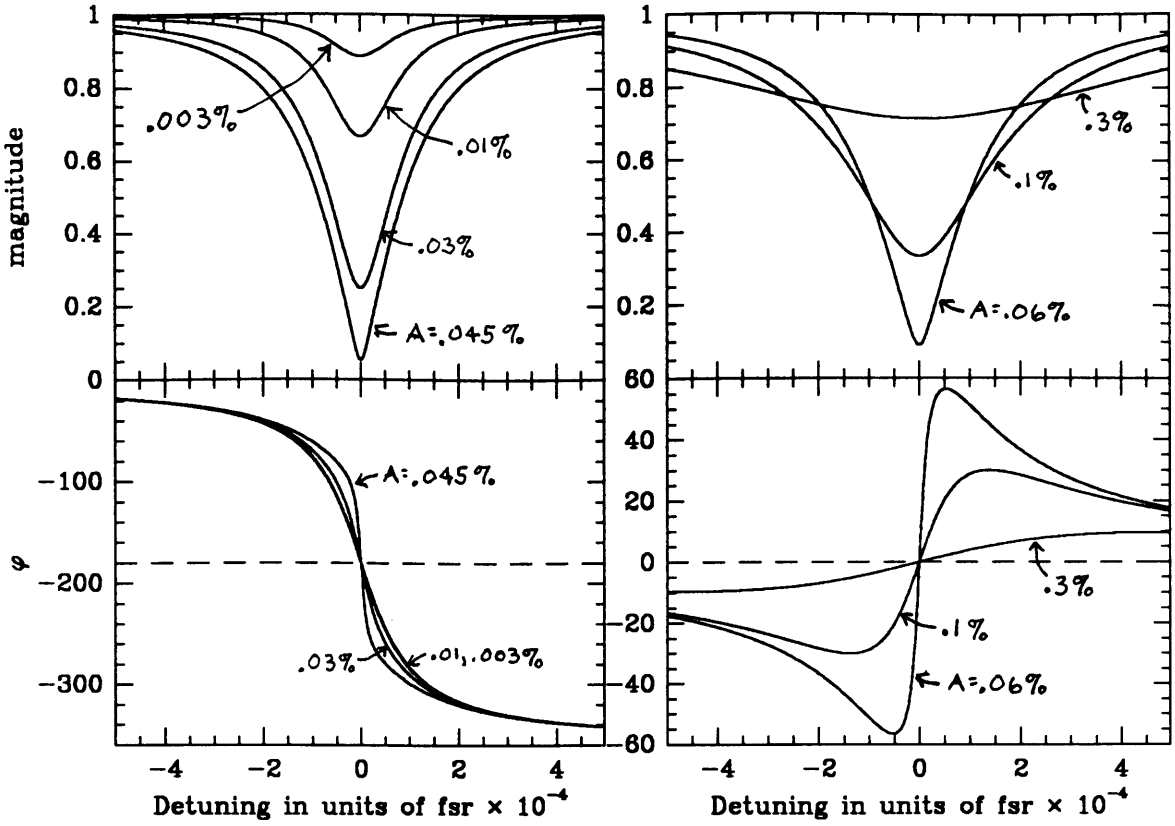

(a) (b)

Fig. A3 Cavity reflection coefficient for $T_1 = 0.1\%$, $T_2 = 0$, a) $A_1{=}A_2 = 0.003$, 0.01, and 0.045%; b) $A_1{=}A_2 = 0.06$, 0.1, and 0.3%.

$|r_i|^2$and $T_i = |t_i|^2$, the cavity reflected and transmitted intensities are

$$R_{\rm cav} \equiv |\hat{r}_{\rm cav}|^2 = \frac{R_1 + (R_1+T_1)^2 R_2 - 2\sqrt{R_1 R_2}(R_1+T_1)\cos\theta}{1 + R_1 R_2 - 2\sqrt{R_1 R_2}\cos\theta}$$
$$T_{\rm cav} \equiv |\hat{t}_{\rm cav}|^2 = \frac{T_1 T_2}{1 + R_1 R_2 - 2\sqrt{R_1 R_2}\cos\theta} = \frac{T_{\rm max}}{1 + (2\mathcal{F}/\pi)^2 \sin^2(\theta/2)} \qquad (82)$$

where $T_{\rm max}$ is the peak transmission and the finesse is defined as

$$\mathcal{F} \equiv \frac{\pi (R_1 R_2)^{1/4}}{1 - \sqrt{R_1 R_2}} \approx \frac{\Delta f_{\rm cav}}{fsr} \,. \qquad (83)$$

The cavity bandwidth, $\Delta f_{\rm cav}$, is the full-width-half-maximum of the transmission curve, and $fsr{=}c/2l$ is the free spectral range of the cavity.

Approximate relations. The arm cavities of a gravity wave interferometer usually satisfy the following conditions for the mirror properties: $R_2 \simeq 1$, $A_1, A_2 \ll 1$. Also one can take $T_2{=}0$, since any transmission can be included in the loss, A_2

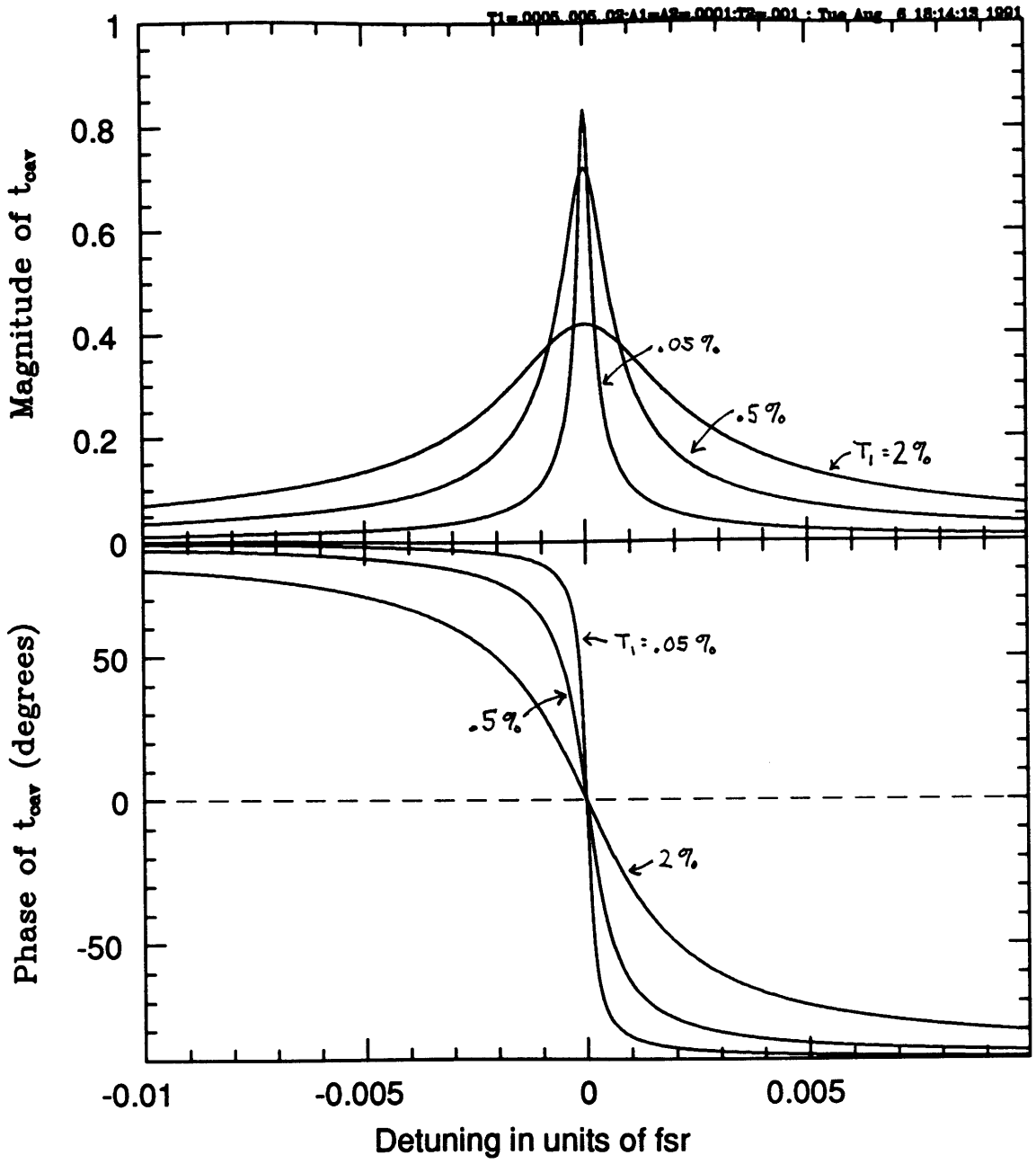

Fig. A4 $\hat{t}_{cav}$ for $A_1=A_2=10^{-4}$, $T_2=10^{-3}$, and T_1=0.05, 0.5, and 2.0%.

(or vice versa). Then the following approximations can be made

$$
\begin{aligned}
|\hat{r}_{cav}(0)|^2 &\approx 1 - \frac{4(A_1+A_2)}{T_1} \\
\left.\frac{d\phi(\theta)}{d\theta}\right|_{\theta=0} &\approx -\frac{4}{T_1\left(1-\left(\frac{A_1+A_2}{T_1}\right)^2\right)} \\
\left.\frac{d\phi}{dl}\right|_{\theta=0} &\approx -\frac{16\pi}{\lambda T_1}\,.
\end{aligned}
\tag{84}
$$

Coupled cavities. Figure A5 shows a three mirror cavity (or two coupled cavities); this is the model for a recycled Fabry-Perot interferometer. Using the reflection coefficient of a single cavity, $\hat{r}_{cav}$, as given above, the fields at various points in the coupled system are easily found:

$$\frac{E_R}{E_0} = \frac{r_r + \hat{r}_{cav}(r_r^2 + t_r^2)e^{i\theta_2}}{1 + r_r\hat{r}_{cav}e^{i\theta_2}} = \frac{r_r(1 - r_1r_2e^{i\theta_1}) + (r_1 - r_2(r_1^2 + t_1^2)e^{i\theta_1})(r_r^2 + t_r^2)e^{i\theta_2}}{1 - r_1r_2e^{i\theta_1} + (r_1 - r_2(r_1^2 + t_1^2)e^{i\theta_1})(r_r^2 + t_r^2)e^{i\theta_2}}$$

$$\frac{E_1}{E_0} = \frac{t_r}{1 + r_r\hat{r}_{cav}e^{i\theta_2}} = \frac{t_r(1 - r_1r_2e^{i\theta_1})}{1 - r_1r_2e^{i\theta_1} + (r_1 - r_2(r_1^2 + t_1^2)e^{i\theta_1})e^{i\theta_2}}$$

$$\frac{E_R}{E_0} = \frac{t_re^{i\theta_2/2}}{1 + r_r\hat{r}_{cav}e^{i\theta_2}}\hat{t}_{cav} = \frac{t_rt_1t_2e^{i(\theta_1+\theta_2)/2}}{1 - r_1r_2e^{i\theta_1} + r_rr_1e^{i\theta_2} - r_rr_2(r_1^2 + t_1^2)e^{i(\theta_1+\theta_2)}} \cdot \tag{85}$$

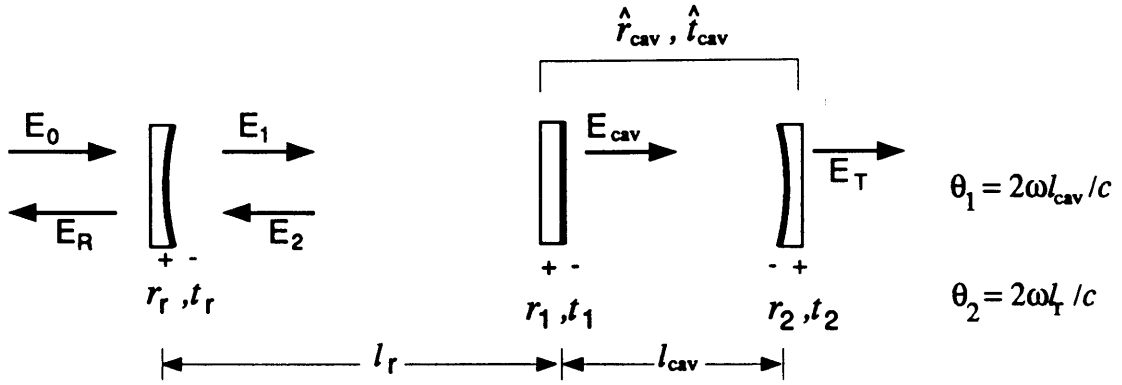

Fig. A5 A three mirror cavity (the model for recycling). The +/- signs indicate the sign convention for reflection from the denoted side of the mirror.

The Fabry-Perot as a frequency discriminator. In the rf-reflection locking technique, the laser light is phase modulated at a frequency greater than the cavity linewidth and the light reflected from the cavity is demodulated at the modulation frequency. The discriminant is the form of the demodulated signal as a function of the frequency of the laser light (the carrier frequency) relative to the cavity resonance frequency. With a phase modulated input field, the field reflected from the cavity is

$$\frac{E_r}{E_0e^{i\omega t}} = J_0A(\theta_0)e^{i\phi(\theta_0)} + J_1A(\theta_+)e^{i\phi(\theta_+)}e^{i\omega_m t} - J_1A(\theta_-)e^{i\phi(\theta_-)}e^{-i\omega_m t} + \cdots \tag{86}$$

Here $\theta_0 = 2\omega l/c$, $\theta_\pm = 2l(\omega \pm \omega_m)/c$, ω_m is the modulation frequency, and the J_i are the Bessel functions of integer order. The reflected intensity thus contains a signal at the modulation frequency. This demodulated signal is shown in Figure A6 as a function of the laser/cavity relative frequency. Also plotted is the transmitted (dc)

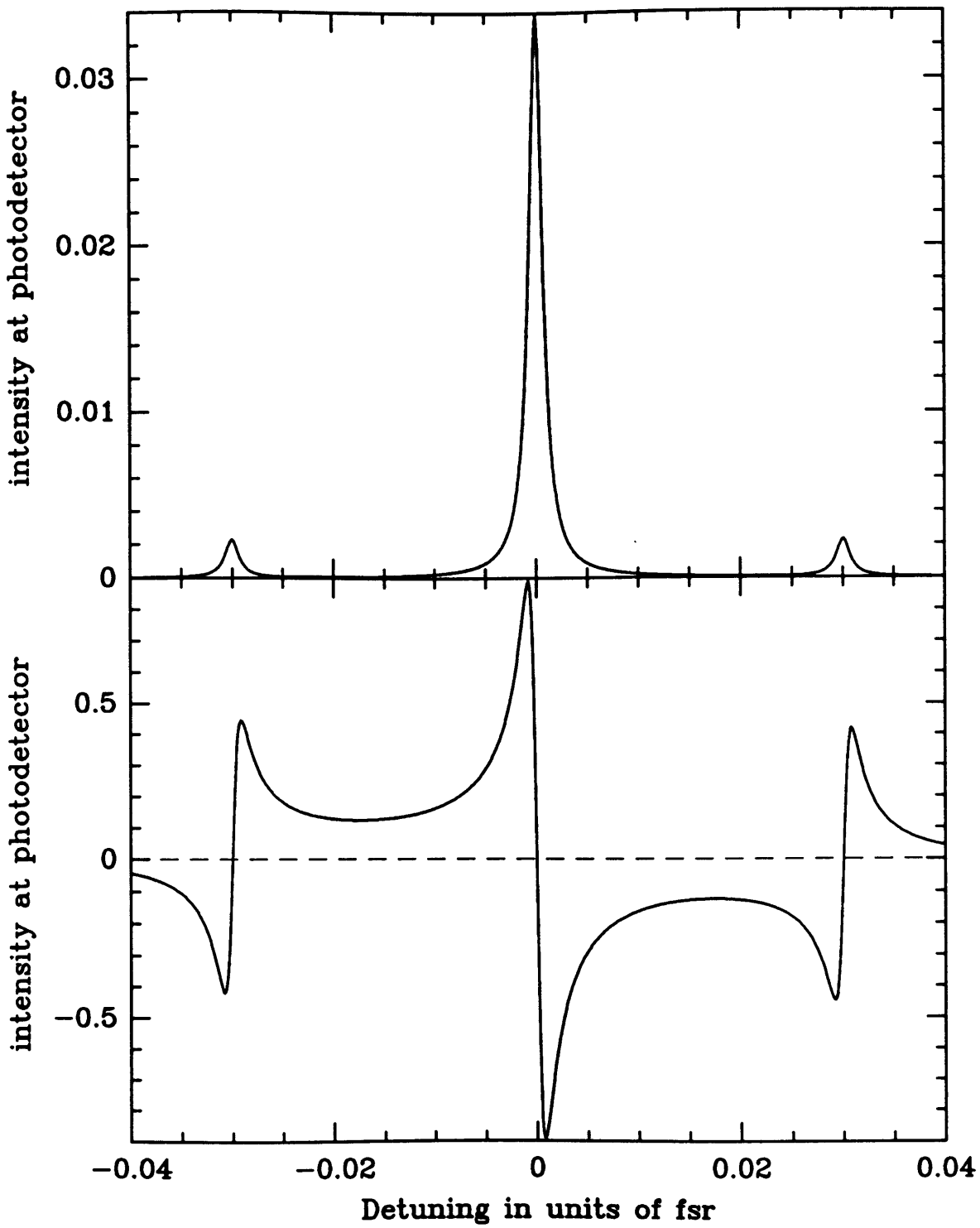

Fig. A6. Top: The transmitted laser intensity (arb units) as the phase modulated laser frequency scans through the resonance of the cavity. Bottom: The demodulated reflected intensity as a function of the laser frequency/cavity resonance detuning. The finesse of the cavity is 625, the modulation frequency is $f_m/\Delta f_{cav} = 19$, and the modulation index is $m = 0.5$.

intensity, showing the position of the first (J_1) sidebands. The demodulated reflected

light is clearly a useful error signal for locking to the center of the cavity resonance.

FP response to frequency modulated light. The discriminant of Fig. A6 is true for laser frequency fluctuations at frequencies much lower than the linewidth of the cavity. For fluctuation frequencies high compared to the cavity linewidth, the cavity filters the fluctuation and the resulting demodulated signal.

Consider a laser field of the form $E(t) = E_0 e^{i\phi(t)} = E_0 e^{i(\omega_0 t + \delta \sin \omega_\delta t)}$, where $\delta = \delta(\omega_\delta) = \delta_0/\omega_\delta$, δ_0 a constant. The instantaneous laser frequency is $\omega(t) = \dot{\phi}(t) = \omega_0 + \delta_0 \cos \omega_\delta t$. That is, the frequency is a constant plus a small sinusoidal modulation, whose amplitude is independent of the modulation frequency ω_δ. Assume that the frequency modulation is small enough that only the first sidebands, $J_{\pm 1}(\delta) e^{\pm i\omega_\delta t}$, need be considered.

In the reflection locking technique, this field is passed through a phase modulator. Again consider only the first sidebands impressed by this modulation: $J_{\pm 1}(m) e^{\pm i\omega_m t}$. There are now nine frequencies: the carrier at ω_0 and the two phase-modulation sidebands at $\omega_0 \pm \omega_m$, and the two frequency-modulation sidebands on each of these frequencies: $\omega_0 \pm \omega_\delta$, $(\omega_0 \pm \omega_m) \pm \omega_\delta$. The carrier is at the cavity resonance; the cavity reflection coefficient for the carrier is $\hat{r}_{\text{cav}} = A_0 e^{i\phi_0}$. The cavity reflection coefficient for the $\omega_0 \pm \omega_\delta$ sidebands is $\hat{r}_{\text{cav}} = A(\omega_0 \pm \omega_\delta) e^{i\phi(\omega_0 \pm \omega_\delta)} \equiv A_\delta e^{\pm i\phi_\delta}$. Assume that the phase-modulation sidebands, and their frequency-modulation sidebands are sufficiently outside the cavity resonance that $\hat{r}_{\text{cav}}=1$ for these six frequencies. The field reflected from the cavity is then

$$\begin{aligned} \frac{E_r}{E_0 e^{i\omega_0 t}} =& J_0(m)\left[J_0(\delta) A_0 e^{i\phi_0} + 2iA_\delta J_1(\delta) \sin(\omega_\delta t + \phi_\delta)\right] + \\ & 2iJ_1(m)[J_0(\delta) - 2iJ_1(\delta) \sin \omega_\delta t] \sin \omega_m t \,. \end{aligned} \tag{87}$$

The intensity at the phase-modulation frequency ω_m is

$$\left|\frac{E_r}{E_0}\right|^2_{\omega_m} = 8J_0(m)J_0(\delta)J_1(m)J_1(\delta)[A_\delta \sin(\omega_\delta t + \phi_\delta) - A_0 \cos\phi_0 \sin \omega_\delta t] \sin \omega_m t \,. \tag{88}$$

The demodulated signal contains an oscillating signal at ω_δ, S_δ, of amplitude

$$|S_\delta| \propto J_0(\delta_0/\omega_\delta) J_1(\delta_0/\omega_\delta) \left[(A_\delta \cos\phi_\delta - A_0 \cos\phi_0)^2 + (A_\delta \sin\phi_\delta)^2\right]^{1/2} \tag{89}$$

and phase

$$\theta_\delta = \tan^{-1}\left[\frac{A_\delta \sin\phi_\delta}{A_\delta \cos\phi_\delta - A_0 \cos\phi_0}\right] . \tag{90}$$

Figure A7 shows the magnitude and phase of the demodulated signal as a function of the frequency of the frequency-modulation, ω_δ. The transfer function is shown for various values of the ratio of the loss ($A_1+A_2+T_2$) to the input transmission. There is no qualitative difference between the cases of the loss being less than or greater

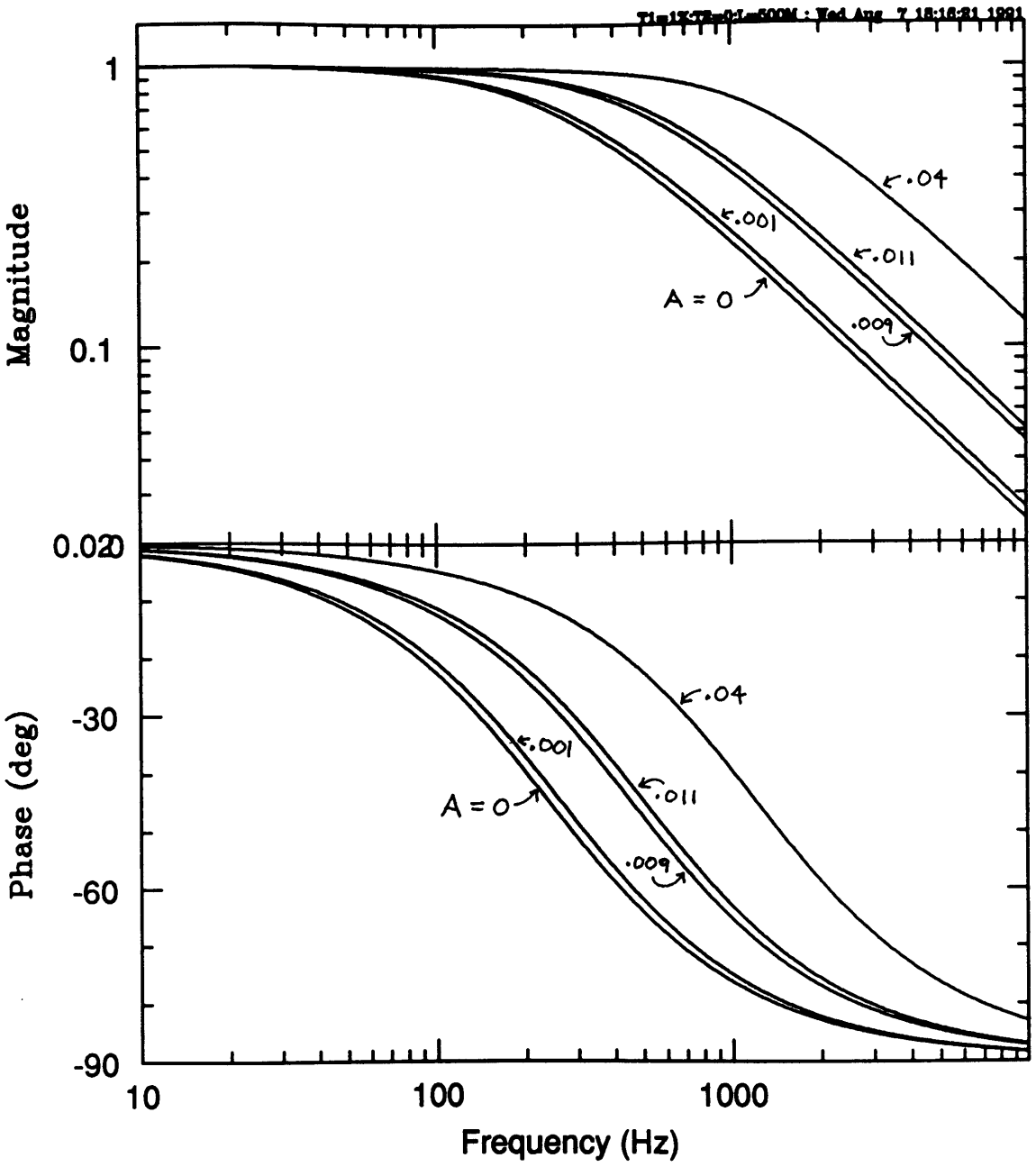

Fig. A7 Frequency response of a cavity error signal to a modulation of the laser frequency, for various values of the cavity losses. The cavity length is 500 m, the input mirror transmission T_1=1%, and the round trip loss takes on the values of A=A_1+A_2+T_2=0, .001, .009, .011, and .04. For the no-loss case, the cavity storage time is 0.33 msec, and the pole frequency is $1/4\pi\tau$ = 240 Hz.

than the input transmission (i.e. being on one side or the other of the critically matched case). In all cases, the pole frequency is given by $1/4\pi\tau_s$, where the storage time is $\tau_s = \tau_t r_1 r_2/(1 - r_1 r_2)$, and the transit time is $\tau_t = l/c$.

Response of a FP interferometer to a gravity wave. The transfer function of a gravity wave to the differential phase shift of a Fabry-Perot interferometer is found by

adding the contributions of each of the (infinitely many) beams that have traversed the cavities. The phase shift produced by a gravity wave of optimal polarization and propagation direction, and amplitude $h_0 e^{-i\omega t}$, for one traversal of an arm was found in chapter 1.3 to be $\delta\phi = (h_0\omega/\omega_0)\sin(\omega\tau_t)e^{i\omega(\tau_t - t)}$. The phase shift after n round trips is thus

$$\delta\phi_n = \frac{h_0\omega_0}{\omega}\sin(n\omega\tau_t)e^{in\omega\tau_t}e^{-i\omega t} . \tag{91}$$

Assuming that the laser light is resonant with the cavity, $2\omega_0 l/c = 0 \bmod 2\pi$, the field reflected from one of the arms is then

$$\frac{E_r}{E_0} = r_1 - t_1^2 r_2 \sum_{n=0}^{\infty}(r_1 r_2)^n e^{i\delta\phi_{n+1}} . \tag{92}$$

For all the terms contributing significantly to the sum, the approximation $\delta\phi_n \ll 1$ holds, since h_0 is so small. Thus the exponential phase factor can be approximated by $(1 + i\delta\phi_n)$. The series can then be summed:

$$\frac{E_r}{E_0} = \hat{r}_{\rm cav}(0) - \frac{ir_2 t_1^2(h_0\omega_0/\omega)\sin\omega\tau_t}{(1 - r_1 r_2)(1 - r_1 r_2 e^{2i\omega\tau_t})}e^{i\omega(\tau_t - t)} \equiv r_0(1 + i\Delta(\omega)) . \tag{93}$$

For the other arm the reflected field is $E_r/E_0 = r_0(1 - i\Delta(\omega))$. The differential arm phase per gravity wave amplitude h is then

$$\frac{\delta\phi_d}{h} = \frac{2\Delta(\omega)}{h} = \left(\frac{2r_2 t_1^2}{r_1 - r_2(r_1^2 + t_1^2)}\right)\left(\frac{\omega_0}{\omega}\right)\frac{\sin\omega\tau_t}{1 - r_1 r_2 e^{2i\omega\tau_t}}e^{i\omega(\tau_t - t)} . \tag{94}$$

This can be simplified for low-frequency gravity waves. For $\omega\tau_t \ll 1$, only terms first order in $(\omega\tau_t)$ are kept; this corresponds to the arm length being small compared to the gravitational wavelength. Also assuming that $r_2 \simeq 1$, and $A_1 \ll 1$, the amplitude of the transfer function becomes

$$\left|\frac{\delta\phi_d}{h}\right| \approx \frac{4\omega_0\tau_s}{\sqrt{1 + (2\omega\tau_s)^2}} , \tag{95}$$

where the storage time is $\tau_s = \tau_t r_1 r_2/(1 - r_1 r_2)$. The phase factor of the transfer function in this approximation is

$$\frac{\delta\phi_d}{h} = \left|\frac{\delta\phi_d}{h}\right| e^{i\Phi} , \quad \Phi = \omega\tau_t + \tan^{-1}(2\omega\tau_s) . \tag{96}$$

The transfer function in this approximation is a simple pole at $f = 1/4\pi\tau_s$.

Appendix B: In-line modulation

This appendix contains a derivation of the shot-noise limited sensitivity for an in-line modulated interferometer with Fabry-Perot cavities in the arms, and for a simple Michelson.

Shot-noise limited sensitivity: FP arms A derivation of the sensitivity must take into account the non-unity contrast of the system. The model used here for the contrast is that there are differing spatial distributions of higher order mode light in the two arms, which do not perfectly interfere. The TEM_{00} component in each arm is assumed to be the same, and the intensities in the two arms are taken to be identical. The spatial distribution of the common fundamental mode is denoted by $D(x,y)$; the higher order mode distribution in one arm is denoted by $F(x,y)$, in the other by $G(x,y)$. Including the in-line differential phase modulation, the fields in the arms are

$$\begin{aligned} E_1 &= \sqrt{2}E_0(D(x,y) + F(x,y))e^{im\sin \mathrm{x}} \\ E_2 &= \sqrt{2}E_0(D(x,y) + G(x,y))e^{-im\sin \mathrm{x}} , \end{aligned} \tag{97}$$

where $\mathrm{x} = \omega_{\mathrm{m}} t$. The spatial functions satisfy

$$\begin{gathered} \int \left(|D|^2 + |F|^2\right) dxdy = 1 , \int \left(|D|^2 + |G|^2\right) dxdy = 1 , \\ \int D^* F dxdy = 0 = \int D^* G dxdy , \int F^* G dxdy = \int G^* F dxdy . \end{gathered} \tag{98}$$

In the following the integration notation will be omitted.

A phase shift due to a cavity length change will appear only on the carrier of the fundamental mode. So to compute the signal, the fields are

$$\begin{aligned} E_1 &= \sqrt{2}E_0\left[D\left(J_0(m)e^{i\phi_d/2} + 2iJ_1(m)\sin \mathrm{x} + \cdots\right) + Fe^{im\sin \mathrm{x}}\right] , \\ E_2 &= \sqrt{2}E_0\left[D\left(J_0(m)e^{-i\phi_d/2} - 2iJ_1(m)\sin \mathrm{x} + \cdots\right) + Ge^{-im\sin \mathrm{x}}\right] . \end{aligned} \tag{99}$$

The intensity at the anti-symmetric output is $|E_1 - E_2|^2/2$. The signal at the modulation frequency is

$$\left.\frac{|E_1 - E_2|^2}{2}\right|_{\mathrm{x}} = 16|E_0|^2|D|^2 J_0(m)J_1(m)\sin(\phi_d/2)\sin \mathrm{x} . \tag{100}$$

For $\phi_d = 0$, the dark fringe dc intensity is

$$\begin{aligned} \left.\frac{|E_1 - E_2|^2}{2}\right|_{\mathrm{dc}} &= |E_0|^2\left[2|D|^2(1 - J_0(2m)) + |F|^2 + |G|^2 - 2F^*GJ_0(2m)\right] \\ &= 2|E_0|^2[1 - CJ_0(2m)] , \end{aligned} \tag{101}$$

where the contrast in this model is $C = |D|^2 + F^*G$. If the intensity $|E_0|^2$ produces a photocurrent I_0, then the photocurrents on the dark and bright fringes, with

no modulation, are $I_{\min} = 2I_0\left(|F|^2 - F^*G\right)$, and $I_{\max} = 2I_0\left(1 + |D|^2 + F^*G\right)$, so $I_{\max} + I_{\min} = 4I_0$. The signal current experiences the transimpedance gain R of the photodetector/mixer. The signal voltage at the output of the mixer is thus

$$V_s(f) = R2|D|^2(I_{\max} + I_{\min})J_0(m)J_1(m)\,\phi_d(f)\,. \tag{102}$$

The noise current is due to the shot-noise of the dc current: $i_n^2 = 2eI_{\rm dc} + 2eI_{\rm det}$, where $I_{\rm dct}$ is the equivalent dc-photocurrent that would produce the photodetector no-light noise level.[3]The noise current also experiences the gain R. In addition, noise sidebands above and below the carrier frequency are both mixed incoherently down to the same low frequency, resulting in an additional factor of $\sqrt{2}$ for the noise voltage (see also chapter 6.1). The noise voltage at the output of the mixer is thus

$$V_n(f) = R\sqrt{2e(I_{\max} + I_{\min})(1 - CJ_0(2m)) + 4eI_{\rm det}}\,. \tag{103}$$

Equating the signal and the noise gives a shot-noise limited phase sensitivity of

$$\phi_d(f) = \sqrt{\frac{2e}{I_{\max} + I_{\min}}}\,\frac{\left[1 - CJ_0(2m) + \frac{2I_{\rm det}}{I_{\max}+I_{\min}}\right]^{1/2}}{2MJ_0(m)J_1(m)}\,, \tag{104}$$

where the mode matching is $M = |D|^2$. In the limit of unity contrast and $I_{\rm dct} = 0$, the phase noise is the familiar $\phi_d(f) = \sqrt{2e/I_{\max}}$.

This derivation assumes only a single pass through the in-line phase modulator, whereas in the experiment each arm beam passes two times through the modulator during the round trip from the beamsplitter. The assumption made is that the effect of this double-passing is just to reduce the effective modulation index, so that the shot-noise limited sensitivity is given by the above (single-pass) formula if the (reduced) effective modulation index is used. This approximation should be valid in the limit of a small modulation index, such that $J_0^2(m) \gg J_1^2(m)$ and J_2 is negligible. The reduction in the modulation index is then just the reduction in the amplitude of the $\pm J_1$ sidebands, and, as given in chapter 3, is

$$\frac{m_{\rm net}}{m_{\rm sp}} = J_0^2(m_{\rm sp})\left\{\left(1 - \sqrt{R_{\rm c}}\right)^2 + \left[\sin\left(2\omega_{\rm m}l/c + \phi_{\rm cav}\right)\right]^2\right\}. \tag{105}$$

Here $m_{\rm sp}$ is the single-pass modulation index, $R_{\rm c}$ is the power reflection coefficient of the cavity on-resonance, l is the modulator-cavity distance, and $\phi_{\rm cav}$ is the cavity phase shift added to the $\pm J_1$ sidebands. Since in this approximation $J_1(m) \propto m$, the signal for the double-passed configuration is reduced by this factor compared to the single-passed case.

[3] This treatment of the shot noise does not include any effects arising from the modulation of the output light power, i.e. the modulation of the dark fringe power resulting from the internal phase modulation. Niebauer et al. (1991) have analyzed this effect, and concluded that it will increase the calculated shot-noise contribution by up to about 2 dB, depending on the system.

A computer program for modeling various interferometer geometries has been developed in this lab by Rainer Weiss. The program is capable of handling large modulation indices by keeping many orders of the modulation sidebands. The program has been used to model in-line modulation, and it predicts that the signal (i.e. the size of the ω_m signal for a given mirror motion) is reduced by the factor calculated with the above formula, for the small modulation index ($m_{sp} = 0.16$) used in the experiment.

Erratum: The shot-noise limited phase sensitivity given in the paper contains an erroneous extra factor of 2.

Shot-noise limited sensitivity: simple Michelson. If the same contrast model as for the FP arm case is used, the only difference in the arm fields is that the signal is assumed to appear on all components of the field in each arm:

$$\begin{aligned} E_1 &= \sqrt{2}E_0(D(x,y) + F(x,y))e^{im\sin x}e^{i\phi_d/2} \\ E_2 &= \sqrt{2}E_0(D(x,y) + G(x,y))e^{-im\sin x}e^{-i\phi_d/2} \,. \end{aligned} \tag{106}$$

The signal at the modulation frequency is in this case

$$\left.\frac{|E_1 - E_2|^2}{2}\right|_x = 4|E_0|^2 C J_1(2m)\sin(\phi_d)\sin x \,, \tag{107}$$

and the signal voltage at the mixer output is

$$V_s(f) = R(I_{max} + I_{min})CJ_1(2m)\phi_d(f) \,. \tag{108}$$

The dark fringe dc intensity, and thus the noise voltage at the mixer output, is the same as for the FP arm case. Equating the signal and the noise gives a shot-noise limited phase sensitivity of

$$\phi_d(f) = \sqrt{\frac{2e}{I_{max} + I_{min}}}\,\frac{\left[1 - CJ_0(2m) + \frac{2I_{det}}{I_{max}+I_{min}}\right]^{1/2}}{CJ_1(2m)} \,. \tag{109}$$

The unity contrast, noise-less detector limit for this case is also $\phi_d(f) = \sqrt{2e/I_{max}}$.

References

Blair, D.G., et al. (1989). *Proposal for the Australian International Gravitational Observatory*, University of Western Australia and Australian National University.

Brillet, A. and Giazotto, A., et al. (1989). *The VIRGO Project*, INFN, Pisa and CNRS, Orsay.

Caves, C.M. (1980). *Physical Review Letters*, **45**, 75.

Caves, C.M. (1981). *Physical Review D*, **23**, 1693.

Christensen, N.L. (1990). *On Measuring the Stochastic Gravitational Radiation Background with Laser Interferometric Antennas*, Ph.D. Thesis, M.I.T., Cambridge, Mass.

Drever, R.W.P. (1982). In *Gravitational Radiation*, eds. N. Deruelle and T. Piran, North Holland: Amsterdam, 1983. p. 321.

Drever, R.W.P., Hall, J.L., Kowalski, F.V., Hough, J., Ford, G.M., Munley, A.J., and Ward, H. (1983). *Applied Physics B*, **31**, 97.

Einstein, A. (1916). *Preuss. Akad. Wiss. Berlin, Sitzungsberichte der Physikalischmathematischen Klasse*, p. 688.

Forward, R.L. (1978). *Physical Review D*, **17**, 379.

Gea-Banacloche, J. and Leuchs, G. (1987). *Journal of Modern Optics*, **34**, 793.

Gertsenshtein, M.E. and Pustovoit, V.I. (1962). *Soviet Physics — JETP*, **16**, 433.

Hall, J.L. and Hänsch, T.W. (1984). *Optics Letters*, **9**, 502.

Hamilton, M.W. (1989). *Contemporary Physics*, **30**, 21.

Hils, D. and Hall, J.L. (1987). *Review of Scientific Instruments*, **58**, 1406.

Hough, J., Hils, D., Rayman, M.D., Ma, L.S., Hollberg, L., and Hall, J.L. (1984). *Applied Physics B*, **33**, 179.

Hough, J., et al. (1989). *Proposal for a Joint German-British Interferometric Gravitational-Wave Detector*, **MPQ 147**, MPQ, Garching.

Kawamura, S., Mizumo, J., Hirao, J., Kawashima, N., and Schilling, R. (1989). *The Institute of Space and Astronautical Science Report No. 637.* Tokyo.

Kerr, G.A., Robertson, N.A., Hough, J., and Man, C.N. (1985). *Applied Physics B*, **37**, 11.

Livas, J., Benford, R., Dewey, D., Jeffries, A., Linsay, P., Saulson, P., Shoemaker, D., and Weiss, R. (1986). In *Proceedings of the Fourth Marcel Grossman Meeting on General Relativity*, ed. R. Ruffini. North Holland: Amsterdam. p. 591.

Maischberger, K., Rüdiger, A., Schilling, R., Schnupp, L., Winkler, W., and Billing, H. (1979). In *Proceedings of the 2nd Marcel Grossman Meeting on General Relativity*, ed. R. Ruffini. North Holland. p. 1083.

Maischberger, K., Rüdiger, A., Schilling, R., Schnupp, L., Winkler, W., and Leuchs, G. (1987). In *International Symposium on Experimental Gravitational Physics*, ed. P.F. Michelson. World Scientific, 1988. p. 316.

Man, C.N., Shoemaker, D., Pham Tu, M., and Dewey, D. (1990). *Physics Letters A*, **148,** 8.

Marcuse, D. (1970). *Bell System Technical Journal*, **49,** 1695.

Meers, B.J. (1988). *Physical Review D*, **38,** 2317.

Meers, B.J. (1989). *Physics Letters A*, **142,** 465.

Meers, B.J. and Strain, K.A. (1991). *Physical Review D*, **43,** 3117.

Michelson, P.F., Price, J.C., and Taber, R.C. (1987). *Science*, **237,** 150.

Niebauer, T.M., Schilling, R., Schnupp, L., Danzmann, K., Rüdiger, A., and Winkler, W. (1991). *Physical Review A*, **43,** 5022.

Rüdiger, A., Schilling, R., Schnupp, L., Winkler, W., Billing, H., and Maischberger, K. (1981). *Optica Acta*, **28,** 641.

Salomon, Ch., Hils, D., and Hall, J.L. (1988). *Journal of the Optical Society of America B*, **5,** 1576.

Saulson, P.R. (1984). *Physical Review D*, **30,** 732.

Saulson, P.R. (1990). *Physical Review D*, **42,** 2437.

Shoemaker, D., Winkler, W., Maischberger, K., Rüdiger, A., Schilling, R., and Schnupp, L. (1986). In *Proceedings of the Fourth Marcel Grossman Meeting on General Relativity*, ed. R. Ruffini. North Holland: Amsterdam. p. 605.

Shoemaker, D., Schilling, R., Schnupp, L., Winkler, W., Maischberger, K., and Rüdiger, A. (1988). *Physical Review D*, **38,** 423.

Shoemaker, D., Brillet, A., Man, C.N., Crégut, O., and Kerr, G. (1989). *Optics Letters*, **14,** 609.

Shoemaker, D., Fritschel, P., Giaime, G., Christensen, N., and Weiss, R. (1991). *Applied Optics*, **30,** 3133.

Spero, R. (1986). In *Proceedings of the Fourth Marcel Grossman Meeting on General Relativity*, ed. R. Ruffini. North Holland: Amsterdam. p. 615.

Strain, K.A. and Meers, B.J. (1991). *Physical Review Letters*, **66,** 1391.

Taylor, J.H. and Weisberg, J.M. (1982). *Astrophysical Journal*, **253,** 908.

Thorne, K.S. (1987). In *300 Years of Gravitation*, eds. S.W. Hawking and W. Israel, Cambridge University Press, p. 330.

Vinet, J., Meers, B., Man, C.N., and Brillet, A. (1988). *Physical Review D*, **38,** 433.

Vogt, R.E. (1989). *A Laser Interferometer Gravitational-Wave Observatory (LIGO): Proposal to the National Science Foundation*, California Institute of Technology.

Ward, H., Hough, J., Kerr, G.A., Mackenzie, N.L., Mangan, J., Meers, B.J., Newton, G.P., Robertson, D.I., and Robertson, N.A. (1987). In *International Symposium on Experimental Gravitational Physics*, ed. P.F. Michelson. World Scientific, 1988. p. 322.

Weber, J. (1960). *Physical Review*, **117,** 306.

Weber, J. (1969). *Physical Review Letters*, **22,** 1302.

Weiss, R. (1972). *Quarterly Progress Report of the Research Laboratory of Electronics of the Massachusetts Institute of Technology.* **105,** 54.